博士論文

放射光分光による酸化物ヘテロ界面の電荷分布と界面強磁性に関する研究

Charge distribution and ferromagnetism at oxide heterointerfaces studied by synchrotron radiation spectroscopy

北村　未歩

Miho Kitamura

Department of Applied Chemistry

School of Engineering

The University of Tokyo

February, 2016

Preface

This thesis marks the compilation of my studies under the supervision of Professor Masaharu Oshima from 2007 to 2009 and that of Professor Hiroshi Fujioka and Professor Hiroshi Kumigashira from 2013 to 2016 as a student of the Department of Applied Chemistry, Graduate School of Engineering, the University of Tokyo.

This thesis is organized in the main 8 chapters. Chapter 1 presents the general introduction to novel interfacial magnetism emerging at the oxide heterointerfaces caused by the charge distribution, and the purpose and strategy of this study on the relationship between charge transfer phenomena and interfacial ferromagnetism. The experimental methods of thin film growth and synchrotron radiation spectroscopy are described in Chapter 2. In Chapter 3, optimization of growth conditions of double perovskite La_2NiMnO_6 (LNMO) is described. I described the element-selective study of the electronic and magnetic states of LNMO in Chapter 4. In Chapter 5, the charge transfer phenomenon, especially its spatial distribution at $LaNiO_3$ (LNO)/$LaMnO_3$ (LMO) heterointerface is investigated. Chapter 6 presents the element-selective study of interfacial ferromagnetism at LNO/LMO hetrointerface. In Chapter 7, the electronic states at the LMO/Nb:$SrTiO_3$ heterointerface are investigated by determining the band diagram. Finally, Chapter 8 is devoted to summary and future prospects.

February, 2016

Miho KITAMURA

Contents

Preface i

1 General Introduction 1

1.1 Background · · ·

5 Charge transfer across the heterointerface between perovskite oxides $LaNiO_3$ and $LaMnO_3$ 84

5.1 Introduction · 84

5.1.1 Previous studies of charge transfer and interfacial magnetism in $LaNiO_3$-$LaMnO_3$ heterostructures · · · · · · · · · · · · · · · · · · 84

5.1.2 Purpose of this study · 87

5.2 Experiments · 87

5.3 Results and discussion · 89

5.3.1 Growth and characterization of $LaNiO_3$/$LaMnO_3$ bilayers · · · · · · · · 89

5.3.2 Confirmation of chemical abruptness at the interface · · · · · · · · · · 92

5.3.3 Valence change due to the charge transfer · · · · · · · · · · · · · · · 98

5.3.4 Approach for evaluation of the spatial distribution of charge transfer · · · 104

5.3.5 Spatial distribution of the transferred charge · · · · · · · · · · · · · 107

5.3.6 Comparison to previous reports and theoretical calculations · · · · · · 112

5.4 Conclusion · 116

6 Interfacial ferromagnetism at the heterointerface between perovskite oxides $LaNiO_3$ and $LaMnO_3$ 117

6.1 Purpose of this study · 117

6.2 Experiments · 117

6.3 Results and discussion · 118

6.3.1 Growth and characterization of $LaNiO_3$/$LaMnO_3$ trilayers · · · · · · 118

6.3.1 X-ray magnetic circular dichroism study of interfacial ferromagnetism · 120

6.4 Conclusion · 134

7 Determination of band diagram for *p*-*n* junction between Mott insulator $LaMnO_3$ and band insulator $Nb:SrTiO_3$ 136

7.1 Introduction · 136

7.1.1 Previous studies of novel magnetic properties of $LaMnO_3$-$SrTiO_3$ superlatiices · 136

7.1.2 Previous studies of *p*-*n* junction between $LaMnO_3$ and $SrTiO_3$ · · · · · 138

7.1.3 Purpose of this study · 139

7.2 Experiments · 140

7.3 Results and Discussion · 141

7.3.1 Growth and characterization of $LaMnO_3$ films · · · · · · · · · · · · 141

7.3.2 Confirmation of chemical abruptness at the interface · · · · · · · · · · 143

7.3.3 Verification of the charge transfer · · · · · · · · · · · · · · · · · · · 146

7.3.4 Valence band spectra · 149

7.3.5 Peak shift of core level spectra · 150

7.3.6 Band alignment of $LaMnO_3$/$Nb:SrTiO_3$ heterojunction · · · · · · · · · 152

7.4 Conclusion · 156

8 Summary and Future prospects 158

Bibliography 163

Acknowledgements 174

Appendix A. List of Publications and Presentations 179

Appendix B. Summary in Japanese 184

Chapter 1
General introduction

1.1 Background

Perovskite transition-metal oxides exhibit a wide variety of unique properties such as the high T_C superconductivity [1], metal-insulator transitions [2], colossal magnetoresistance [3], and multiferroics [4]. These properties originate from complex interactions involving the spin, charge, and orbital degrees of freedom of the strongly correlated electrons [2] Recently, well-defined oxide heterointerfaces and superstructures have been accomplished due to the rapid progress of the growth techniques. The developments of a pulsed laser deposition, a molecular beam epitaxy and a sputtering method, as well as the monitoring system using the reflection high-energy electron diffraction (RHEED) during the thin film growth, enable us to fabricate high quality oxide heterointerfaces in an atomic scale. The perovskite oxide heterointerface, which is composed of two different isostructural materials with a chemical formula of ABO_3, produces distinctive interfacial electronic and/or magnetic properties not present in the bulk constituents [5, 6, 7]. These unusual properties have been of considerable interest because of the potential applications of the heterostructure in future electronic devices with multifunctional properties. Extensive studies on the behavior of oxide heterojunctions have revealed that these properties can be tuned through the interfacial charge transfer (redistribution) and the resulting reconstruction of the spin and orbital states. For example, the metallic conductivity due to the charge modulation has been reported at the interface between Mott insulator $LaTiO_3$ and band insulator $SrTiO_3$ [8], furthermore, the metallic state and then the superconductivity appear at the interface between two insulators $LaAlO_3$ and $SrTiO_3$ [9, 10].

One particularly interesting aspect of these heterostructures seems to be the appearance of ferromagnetism at the interface between non-ferromagnetic oxides. For example, superlattices (heterointerfaces) composed of antiferromagnetic insulator layers of $LaCrO_3$-$LaFeO_3$ [11, 12] and $LaMnO_3$ (LMO)-$SrMnO_3$ [13, 14] are ferromagnetic. Similar behavior is also seen in lattices consisting of the antiferromagnetic insulator $CaMnO_3$ and paramagnetic metal $CaRuO_3$ [15, 16, 17] or $LaNiO_3$ (LNO) [18].

$LaMnO_3$ (LMO)-$SrMnO_3$ system is the most intensively studied. $LaMn^{3+}O_3$ possesses one e_g electron per Mn site, wheres there has no e_g electron in $SrMn^{4+}O_3$, resulting in the difference of chemical potential at the interface which promotes the charge (hole) transfer from an LMO layer to an $SrMnO_3$ layer. As a result, the transition takes place from antiferromagnetic insulators LMO and $SrMnO_3$ to ferromagnetic metal $La_{1-x}Sr_xMnO_3$ around the interfacial region because mixed valence Mn^{3+}/Mn^{4+} state favors double-exchange ferromagnetism. Koida and coworkers investigated magnetic and transport properties of $(LMO)_m(SrMnO_3)_m$ superlattices with varying the periodicity m [13], as shown in Fig. 1.1. The shorter-period superlattices than the critical number related to the charge distribution showed homogeneous ferromagnetic metallic properties, whereas the longer-period ones exhibited a phase separation consists of interface region and bulk inside and significant suppression of the ferromagnetism and the metallicity. For LMO-$SrMnO_3$ system, the distances of charge distribution have been evaluated to be some monolayer (ML): 2-4 ML from transport and magnetization measurements [13, 19] and about 3 ML from polarized neutron reflectivity measurements [20].

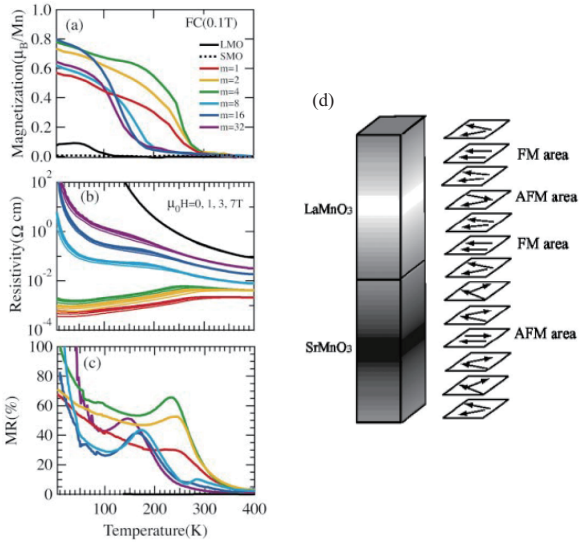

Figure 1.1: Temperature dependence of (a) magnetization, (b) resistivity, and (c) magnetoresistance of $(LaMnO_3)_m(SrMnO_3)_m$ superlattices. (d) The schematic images of the hole distribution. The dark color region has higher hole concentration than than the light region [13].

As for $CaMnO_3$-$CaRuO_3$ and $CaMnO_3$-LNO supperlattices, the inherent electron penetration occurs from the paramagnetic metal $CaRuO_3$ or LNO layer to the antiferromagnetic insulator $CaMnO_3$ layer resulting in the ferromagnetism in the interface region of the $CaMnO_3$ layer [15, 16, 17, 18]. Figure 1.2 depicts x-ray magnetic circular dichroism (XMCD) spectra of Mn and Ru for $CaMnO_3$-$CaRuO_3$ superlattices measured by Freeland *et al*. [16]. XMCD signals are clearly observed in Mn XMCD spectram and not in Ru one, indicating the presence of magnetic moments only in $CaMnO_3$ layer.

Furthermore, the charge transfer also plays an important role for the exotic interfacial magnetism of the heterostructures which consist of ferromagnetic materials. The novel exchange bias was observed in the heterostructures of $La_{0.75}Sr_{0.25}MnO_3$/LNO [21] and $La_{0.7}Ca_{0.3}MnO_3$/LNO [22], where the charge transfer between Ni and Mn ions ($Ni^{3+} + Mn^{3+} \rightarrow Ni^{2+} + Mn^{4+}$) was confirmed by x-ray absorption spectroscopy and x-ray photoemission

spectroscopy. For $La_{2/3}Ca_{1/3}MnO_3$-$YBa_2Cu_3O_7$ superlattices, electron-transfer from Mn ion to Cu ion suppresses ferromagnetism in manganite and induces a spin-polarized layer in cuprate about a few nanometers from the heterointerface (Fig. 1.3) [23].

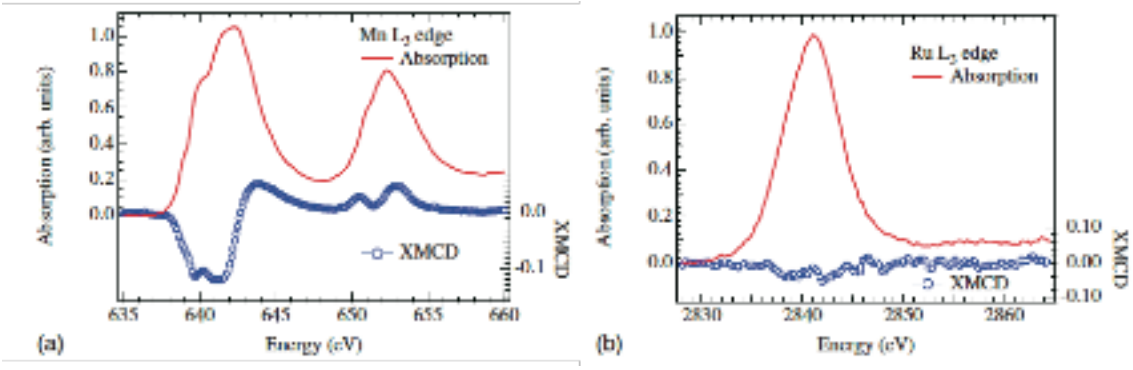

Figure 1.2: X-ray absorption spectra and x-ray magnetic circular dichroism spectra of (a) Mn-L_3 edge and (b) Ru-L_3 edge of $CaMnO_3$-$CaRuO_3$ superlattice [16].

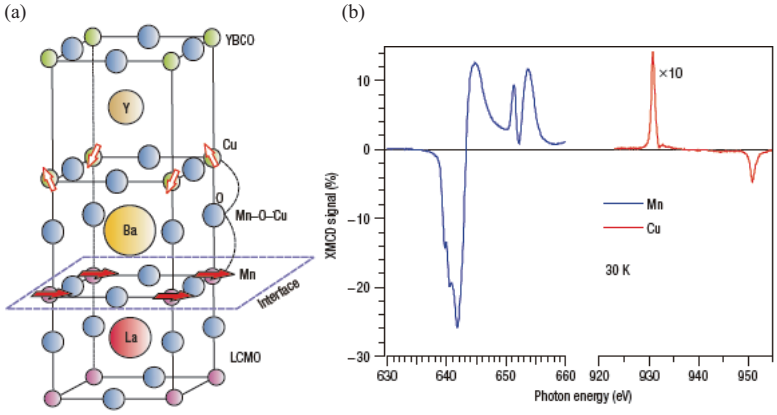

Figure 1.3: (a) Atomic stacking sequence and arrangement of the atoms of $La_{2/3}Ca_{1/3}MnO_3$/$YBa_2Cu_3O_7$ interface. The arrows show the possible magnetic moments. (b) X-ray magnetic circular dichroism spectra of Mn-$L_{2,3}$ edge and Cu-$L_{2,3}$ edge of $La_{2/3}Ca_{1/3}MnO_3$-$YBa_2Cu_3O_7$ superlattice [23].

1.2 Purpose of this study

As described above, the heterointerfaces which consist of perovskite transition-metal oxides show a lot of interesting interfacial magnetism. For these novel phenomena, the charge transfer (charge redistribution) at the interface is considered to play a significant role. Spin and orbital states of the transition metal ions around the interface region are modulated by the charge transfer, resulting in the change of magnetic exchange coupling between transition metal ions. In order to understand and control the interfacial magnetism, it is inevitable to decide the valence change and its spatial distribution and the relationship between the charge distribution and interfacial magnetism.

In this thesis, I have studied two different perovskite heterointerfaces. One is the heterointerface between a paramagnetic metal $LaNiO_3$ (LNO) and an antiferromagnetic (bulk) /ferromagnetic (film) insulator $LaMnO_3$ (LMO), and the other is the heterointerface between a Mott insulator LMO and a band insulator Nb-doped $SrTiO_3$ (Nb:STO). For the both heterostructures, it has been reported that ferromagnetism in supperlattices [24, 25] and exotic magnetic properties such as a ferromagnetic modulation [26] and an exchange bias effect [27] (For the detail, see Chapter 5 and 7). However, there is a difference between two heterointerface: Considering the redox potentials of B-site ions coordinated by six oxygen ions (Fig. 1.4) [28, 29], the charge transfer is expected for an LNO/LMO interface, whereas not expected for an LMO/Nb:STO one. For these contrasting heterointerfaces, I have elucidated the charge transfer phenomena, especially the spatial distribution of the transferred charge, and investigated the relationship between the charge transfer and the interfacial ferromagnetism. The strategy of this study is depicted in Fig.1.5. I have fabricated two kinds of heterointerfaces by a pulsed laser deposition method and characterized by synchrotron radiation spectroscopy, utilizing its elemental selectivity and surface (buried interface) sensitivity. In order to study an LNO/LMO interface, as a first step, I have grown and characterized a double perovskite

La_2NiMnO_6 (LNMO) film. LNMO can be regarded as a "natural superlattice", in which LNO and LMO layers alternately stack along the [111] direction resulting in the rock-salt-type ordering of Ni and Mn ions. Then I have investigated LNO/LMO heterostructures with a well-defined interface accomplished by monitoring the intensity oscillation of RHEED during the growth in order to the spatial distribution of the charge transfer.

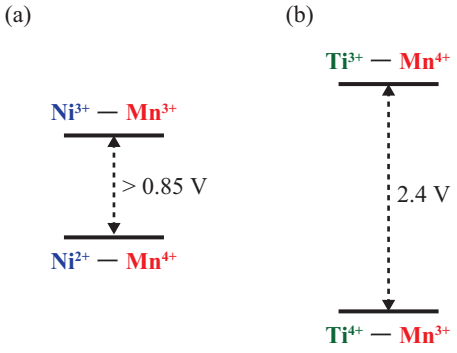

Figure 1.4: Redox potentials between (a) Ni and Mn, and (b) Ti and Mn [28, 29].

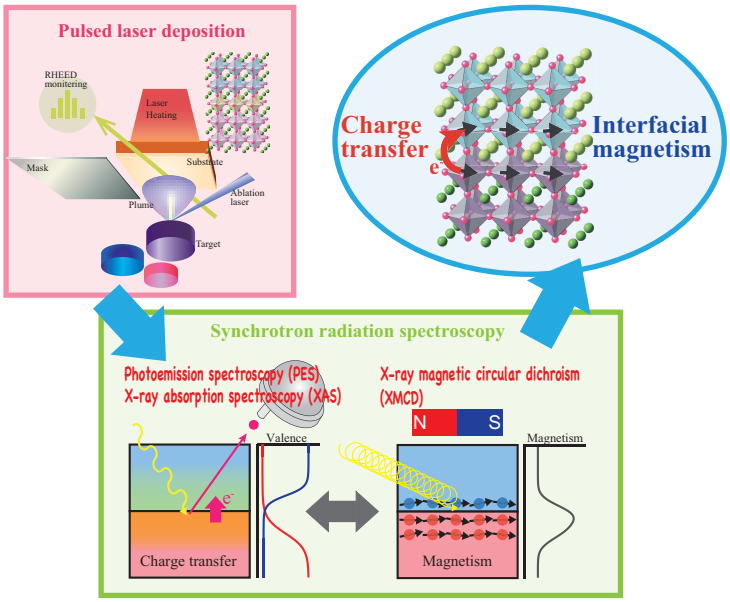

Figure 1.5: Strategy of this study.

This thesis is organized as follows. Chapter 1 describes the general background to introduce the studies on interfacial magnetism of oxide heterostructures, and the strategies and the purpose of the present study on the relationship between charge distribution and interfacial ferromagnetism at perovskite oxide heterointerfaces using synchrotron radiation spectroscopy. The experimental methods of thin film growth, characterization of a film, and synchrotron radiation spectroscopy are briefly described in Chapter 2. I present growth condition dependence of ferromagnetic properties of a "natural superlattice" LNMO thin film in Chapter 3. By strictly controlling the growth temperature and oxygen pressure to stabilize Ni^{2+}-O-Mn^{4+} superexchange ferromagnetic interaction, LNMO film was obtained that shows higher ferromagnetic transition temperature and higher magnetic moment. In chapter 4, electronic and magnetic states of the LNMO film grown under the optimized condition have been investigated using synchrotron radiation spectroscopy. The charge transfer (Ni^{3+} + Mn^{3+}→ Ni^{2+} + Mn^{4+}) occurs in LNMO and the magnetism residing Ni and Mn ions are coupled ferromagnetically. I have verified that the ferromagnetism of LNMO is derived from Ni^{2+}-O-Mn^{4+} ferromagnetic superexchange interaction. In Chapter 5 and Chapter 6, I develop a "natural superlattice" LNMO to the well-controlled LMO/LMO heterointerfaces. The charge transfer between LNO and LMO and the spatial distribution of the transferred charge characterized by x-ray absorption spectroscopy are presented in Chapter 5 and the interfacial ferromagnetic states evaluated by x-ray magnetic circular dichroism are described in Chapter 6. The similar charge transfer to LNMO occurs at the interface between LNO and LMO, and it has been concluded that its spatial distribution is different between two layers. Magnetization are induced in Ni^{2+} ion in the vicinity of the interface, where the valence changes from 3+ to 2+ due to the charge transfer, and coupled ferromagnetically to Mn spins. The photoemission study of the other interface LMO/Nb:STO is written in Chapter 7. In contrast to the LNO/LMO interface, the charge transfer do not occur between Ti and Mn ions and LMO/Nb:STO heterojunctions can be

described on the basis of the *p*-*n* junction model for conventional semiconductors. Finally Chapter 8 is devoted to summary of this thesis and future prospects.

Chapter 2

Experimental Methods

2.1 Thin film growth

2.1.1 Pulsed laser deposition

Pulsed laser deposition (PLD) is a physical vapor deposition (PVD) technique especially useful for growing high quality oxide thin films. PLD has advanced since research on high temperature superconductive cuprates began, and has dramatically developed since the introduction of the excimer laser to thin film growth. Figure 2.1 shows a schematic image of the PLD process. In PLD, a high-power-laser pulse irradiates a sintered target and the material of the target melts, evaporates, and ionizes in the luminous pillar, called the plasma plume, owing to the rapid increase in the temperature of the target surface. The atoms and ions of the target material in the plume are deposited and migrate on the surface of the substrate, and a thin film grows on the surface. In most cases, ultraviolet pulse lasers are used for ablation, such as ArF (193 nm), KrF (248 nm), and XeCl (308 nm) excimer lasers and 3rd- (355 nm) and 4th- (266 nm) harmonic generation YAG solid-state lasers. To activate the surface migration of adatoms, the temperature of the substrate is typically kept high using a heater, ramp, and focused infrared lasers. The ablated species in the plume interact with background gases such as oxygen, ozone,

nitrogen, and argon, and it is important to control the plume conditions to achieve the desired film quality. It is possible to control the film thickness on an atomic scale by incorporating reflection high-energy electron diffraction measurements during the growth process. This system is called “laser molecular beam epitaxy (Laser MBE)”.

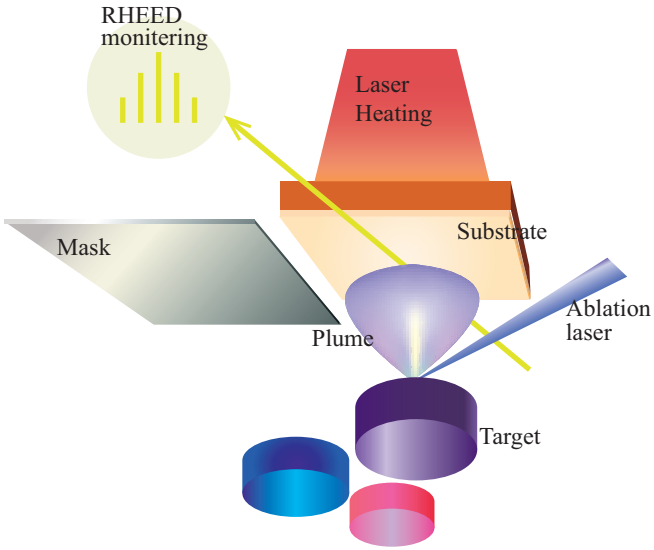

Figure 2.1: A schematic image of the PLD process

Advantages of PLD:

1) Materials with high melting point can be deposited given they absorb the ablation laser.

2) The composition of a target may be transferred to that of the deposited film because the ablation laser instantly exfoliates only the surface of the target.

3) Use of a high pressure of background gas is possible.

4) It is possible to digitally control the thin film growth.

5) Because PLD is a nonequilibrium process, it is possible to grow thin films of materials otherwise attainable under thermodynamic conditions.

6) PLD is a less contaminating process than other PVD processes because the ablation source is located outside the chamber.

Disadvantages of PLD:

1) Some particles of submicron size are often generated on the film surface.

2) It is difficult to obtain large areas with homogeneous composition and thickness.

3) Polishing of the surface of a target is needed to prevent the plume from leaning.

2.2 Characterization of thin films

2.2.1 Reflection high-energy electron diffraction

Reflection high-energy electron diffraction (RHHED) is commonly used to characterize surface morphology and crystallization. An electron beam accelerated by a high voltage (10–50 keV) enters the surface of the sample at a small incidence angle (1–3°). The incident electrons are reflected by the atoms of the surface and form diffraction patterns on the fluorescent screen. Owing to the small incidence angle, RHEED is a surface sensitive method despite the high energy of the electron beam, and so it is possible to use it to monitor the process of thin film growth in the molecular beam apparatus. In RHEED measurements, diffraction patterns are observed as the crosspoint between the Ewald's sphere defined by the

electron energy and reciprocal rods, as shown in Fig 2.2, because the surface can be regarded as a two-dimensional lattice owing to the oblique incidence angle.

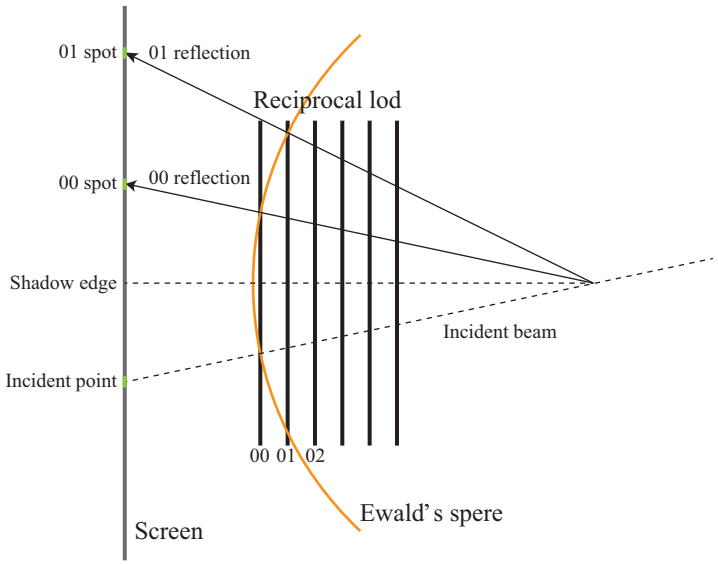

Figure 2.2: A schematic image of the principle of reflection high-energy electron diffraction

RHEED patterns are sensitive to the surface morphology parallel to the electron beam. If the surface is very flat on the atomic scale, the diffraction pattern appears as a bright spot because the radius of the reciprocal rod is very small. When the surface has a step-terrace structure and/or some small two-dimensional islands, streak patterns are observed because the radius becomes larger. Spot patterns appear if the surface is rough because the surface acts as a three-dimensional lattice to the electron beam. Furthermore, RHEED patterns also reflect the crystal quality of the surface. Spot and/or streak patterns are obtained from single crystal

surfaces. Ring patterns and hollows (no pattern) are observed when the surface is polycrystalline and amorphous, respectively.

RHEED can be used for another purpose during thin film growth. Figure 2.3 shows the relationship between RHEED oscillation and growth state. By monitoring the intensity of the diffraction spot, it is possible to obtain information on the growth mode and estimate the growth rate. The intensity of the spot decreases with the creation of two-dimensional islands, and recovers as the density of islands increases. As a result, the intensity oscillates, synchronizing with the growth of each new layer with one-unit-cell height. In this thesis, this RHEED oscillation was used to control film thickness during heterostructure fabrication.

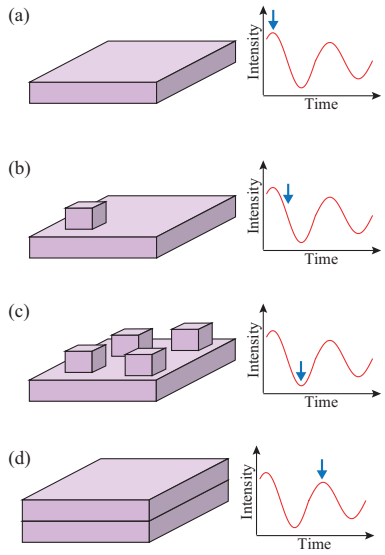

Figure 2.3: The relationship between surface morphology (left) and RHEED oscillation (right) during 1-monolayer (ML) this film growth. (a) Before deposition, (b) Right after starting deposition, (c) At 0.5-ML deposition, and (d) After 1-ML deposition.

2.2.2 Atomic force microscopy

The characterization of surface morphology was performed using atomic force microscopy (AFM; Nanoscope 3A, Veeco). AFM is a powerful tool for evaluating three-dimensional information on a film surface with a very high vertical resolution of sub-nanometers. In AFM measurements, atomic forces between a cantilever and the sample surface are measured to characterize the surface morphology. The tapping mode was used in this work, where the cantilever vibrates in a resonant frequency and scans over the surface with tapping. The change in the frequency and amplitude of vibration caused by the atomic force is measured through laser irradiation of the cantilever and is controlled to maintain constant vibration using a feedback mechanism, as shown in Fig. 2.4. Information on the surface morphology is obtained from the feedback signal. This mode can realize higher resolution and lower damage to the sample.

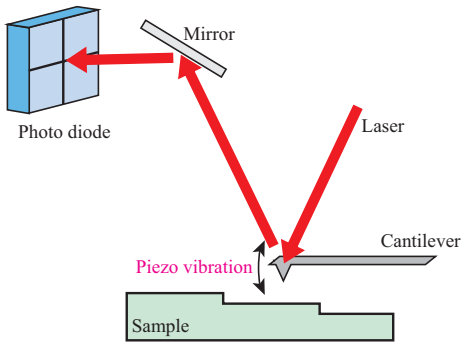

Figure 2.4: A Schematic diagram of atomic force microscopy.

2.2.3 X-ray diffraction

X-ray diffraction is commonly used to investigate the crystal structure of a material. This technique is based on the elastic scattering of x-ray from ordered structures. The obtained diffraction pattern is governed by Bragg's equation,

$$2d_{hkl}sin\theta = n\lambda \quad (2.1)$$

where d_{hkl}, θ, and λ are the length of the (hkl) plane period, incident angle, and x-ray wavelength, respectively. The intensity of a diffraction peak is determined by $S \cdot S$, where S is a structure-factor given by,

$$S(hkl) = \sum_j f_j \exp\left[-2\pi i\left(x_j h + y_j k + z_j l\right)\right] \quad (2.2)$$

where f_j is the atomic-scattering-factor.

The lattice parameters perpendicular to the surface of a sample can be obtained using a $2\theta/\theta$ scan because the crosspoints between reciprocal points of the Miller planes perpendicular to the surface and Ewald's sphere exit along the line of the $2\theta/\theta$ scan. Reciprocal space mappings, shown in Fig. 2.5, were also measured to obtain information on the in-plane orientation between film and substrate. The relationships between (2θ,ω) and coordinates in reciprocal space (Q_{IP}, Q_{OP}) are given by,

$$\begin{aligned} Q_{IP} &= R[cos\omega - \cos(2\theta - \omega)] \\ Q_{OP} &= R[sin\omega + \sin(2\theta - \omega)] \end{aligned} \quad (2.3)$$

where R is the radius of Ewald's sphere. The plane intervals d_{IP} and d_{OP} are expressed by,

$$d_{IP} = n\lambda/2Q_{IP}$$
$$d_{OP} = n\lambda/2Q_{OP} \quad (2.4)$$

where n is an integer related to the Miller indices and λ is the x-ray wavelength.

In this thesis, a RINT 2400 (RIGAKU) and RINT ATX-G (RIGAKU) with Cu K_α source were used. Diffractometer type 5250 (Huber) equipped with BL-4C, KEK-PF and SmartLab (RIGAKU) at BL-7C, KEK-PF were also utilized for synchrotron radiation x-ray diffraction measurements.

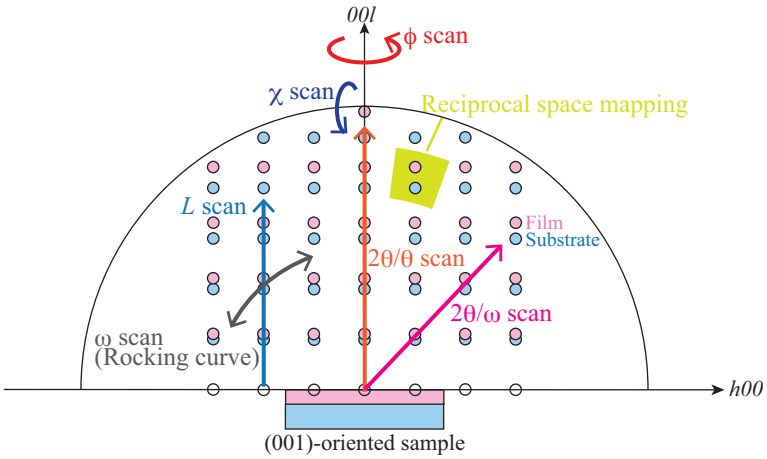

Figure 2.5: A Schematic diagram of geometry of x-ray diffraction measurement. Reciprocal points of a film and a substrate are shown in the case of coherent growth.

2.2.4 Characterization of magnetic properties

The magnetic properties of the thin films were characterized by using a magnetic properties measurement system (MPMS, Quantum Design) equipped with a superconducting

quantum interference device (SQUID). This apparatus can detect very small magnetization to a sensitivity of 10^8 emu. The temperature dependence of magnetization was measured to evaluate the Curie temperature of the films. The magnetic field dependence of the magnetization measurements was evaluated to obtain the saturated magnetization and the coercive field. The magnetic field was applied along the [100] axis parallel to the film surface.

2.2.5 Optical conductivity measurements

Optical constants, such as complex refractive index and complex dielectric constant, are commonly obtained by measuring absorption and/or reflectivity spectra. When the sample is thin and/or absorption coefficient α is small, one can estimate α by absorption spectrum, and then the extinction index $\kappa(\omega)$ can be calculated by,

$$\kappa = \frac{\alpha\lambda}{4\pi} \quad (2.5)$$

However, this method is sometimes complex because of reflection at the surface as well as interference and multiple reflection inside the sample. The calculation of complex refractive index and complex dielectric constant from reflectivity spectra is widely adopted as an alternative method. In this method, the phase factor $\theta(\omega)$, the change in the phase of the light caused by reflection on the surface, is calculated using the Kramers-Kronig relation from the measured reflectivity spectrum $R(\omega)$. The refractive index $n(\omega)$ and the extinction index $\kappa(\omega)$ are estimated using the following equations.

$$n(\omega) = \frac{1-R}{1+R-2\sqrt{R}\cos\theta}$$
$$\kappa(\omega) = \frac{2\sqrt{R}\sin\theta}{1+R-2\sqrt{R}\cos\theta} \quad (2.6)$$

In this study, reflectivity and transmittance spectra were measured to obtain optical constants. Reflectivity $R(\omega)$ and transmittance $T(\omega)$ are functions of the wavelength of the incident light, the thickness of the film and substrate, the refractive index of the substrate, and the refractive index and extinction index of the film. [30]. The refractive index and extinction index are numerically calculated using the successive approximation called the Newton-Raphson method. Figure 2.6 shows a flow of the Newton-Raphson method. M. Matsunami of RIKEN, SPring-8 aided with the numerical calculations of $n(\omega)$ and $\kappa(\omega)$. Optical conductivity $\sigma(\omega)$ is given by,

$$\sigma(\omega) = \omega n(\omega)\kappa(\omega)/2\pi \quad (2.7).$$

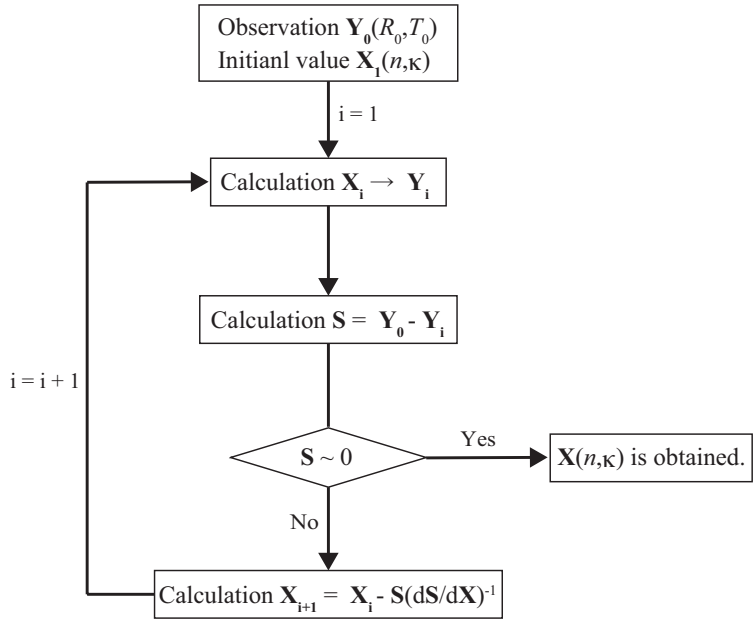

Figure 2.6: Flow of Newton-Raphson method

2.3 Synchrotron radiation spectroscopy

2.3.1 Photoemission spectroscopy

Figure 2.7 shows a schematic image of the principle of photoemission spectroscopy [31]. When an electron in a solid absorbs a photon with energy of $h\nu$, it may be excited to a higher electronic state. If the energy of the excited electron exceeds the work function, ϕ, of the material it is emitted from the material. This is called photoemission, and the emitted electrons are called photoelectrons. Following the law of energy conservation, the kinetic energy of the photoelectron is given by,

$$E_{kin}^{vac} = h\nu - \phi - E_B \quad (2.8)$$

where $E_{kin}{}^{vac}$ is the kinetic energy of the photoelectron based on the vacuum level (E_{vac}), and E_B is the binding energy based on the Fermi level (E_F). In real experiments, the kinetic energy (E_{kin}) measured from E_F rather than from E_{vac} is directly observed. Then, the following equation is convenient to use,

$$E_{kin} = h\nu - E_B \quad (2.9)$$

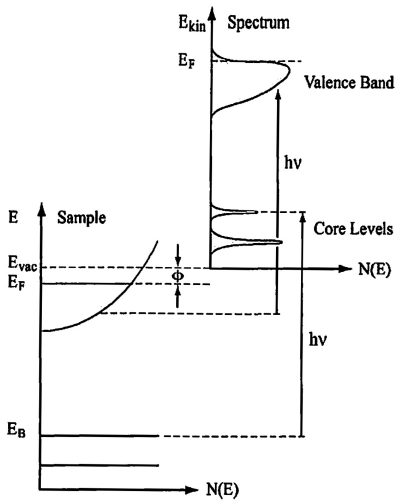

Figure 2.7: A schematic image of the principle of photoemission spectroscopy [31].

Photoemission spectroscopy is a surface-sensitive technique. Electrons are inelastically scattered by electron–electron and electron–phonon interactions before they are emitted from the material. This scattering determines the escape depth of the photoelectrons. Escape depth experimentally measured as a function of photoelectron kinetic energy is called "the universal curve", and is a very general indication of behavior that is material-independent, shown in Fig. 2.8 [31].

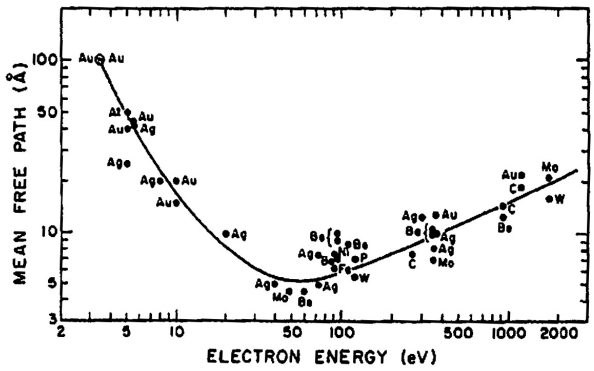

Figure 2.8: Mean free path of a photoelectron in various materials as a function of its kinetic energy [31].

2.3.2 Resonant photoemission spectroscopy

Synchrotron radiation has an advantage that photon energy is valuable. By utiliting this feature, one can measure the resonant photoemission spectrum. A schematic diagram of the resonant photoemission spectroscopy process is shown in Fig. 2.9. When the incident photon energy is equal to the energy difference between the *p* core level and the *d* valence states of the material, not only the direct photoemission process of a *d* electron in the valence states,

$$p^6 d^N + h\upsilon \rightarrow p^6 d^{N-1} + e^- \quad (2.10)$$

but also the photoabsorption of a core *p* electron and subsequent Auger-type decay, called Coster-Krönig decay,

$$p^6 d^N + h\upsilon \rightarrow p^5 d^{N+1} + e^- \rightarrow p^6 d^{N-1} + e^- \quad (2.11),$$

occur. These two processes have the same electron configuration in both the initial and final state, and therefore quantum-mechanical interference comes about. Thus, the intensity of the photoemission spectrum is resonantly enhanced and shows a so-called Fano profile [Fano PR124]. Because this enhancement occurs only for the emission of *d* electrons, it is possible to obtain the *d* partial density of states (DOS) in a material.

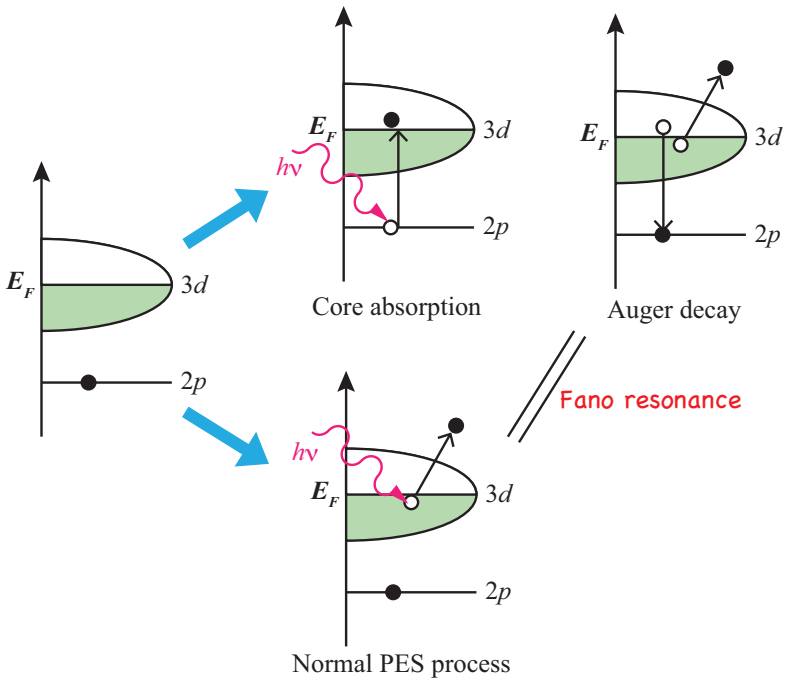

Figure 2.9: A schematic diagram of the principle of resonant photoemission spectroscopy.

2.3.3 X-ray absorption spectroscopy

X-ray absorption spectroscopy (XAS) is the measurement of photo-absorption following the excitation of a core electron into an unoccupied state as a function of photon energy. Utilizing the characteristic of synchrotron radiation that photon energy is valuable, one can obtain absorption spectra. According to the Fermi golden rule, the absorption intensity is given by,

$$I(h\nu) = \sum_f |\langle f|T|i\rangle|^2 \delta(E_i - E_f - h\nu) \quad (2.12)$$

where T is the dipole transition operator, and i and f represent initial and final state, respectively. In the dipole transition, the change in the angular momentum is limited to ±1. The O-K XAS spectrum, which involves excitation from O 1s to 2p orbitals, represents the unoccupied O 2p states. When O 2p orbitals are hybridized with other orbitals, O-K XAS spectra enable us to obtain information on the unoccupied states. In 3d transition-metal (TM) compounds, TM $L_{2,3}$-XAS spectra, which involves excitation from TM $2p_{1/2}$ and $2p_{3/2}$ to 3d orbitals, reflect the 3d states, such as the valence, spin states and crystal-field splitting. There are two kinds of modes for XAS measurement, transmission mode and yield mode. Transmission mode is standard for hard x-rays. In this mode, the intensities in front of and behind the sample are measured and then the amount of transmitted x-rays is calculated. However, this mode is not suitable for soft x-rays because of the strongly interact with the sample.

As the alternative to transmission mode, the yield mode is standard for soft x-rays. In yield mode, products which are generated in the decay process of core holes created by absorption are measured, and it can be classified into Auger-electron-yield, total-electron-yield and total-fluorescence-yield methods. The Auger-electron-yield method is the measurement of Auger electrons of specific energy emitted during the decay process. This method has the least ambiguity and relatively high surface sensitivity. The total-electron-yield method is the most widely used of the yield modes. although it has not been fully understood yet. In this method, all electrons escaping from a sample during the decay process are counted by measuring the compensation current from the earth to the sample. The signals obtained are dominated by secondary electrons generated in the cascade process of the Auger decay electrons. This is the most convenient method because of the ease of measurements and the strongest signals. The

total-electron-yield method was used throughout this study. In the total-fluorescence-yield method, the fluorescent decay to core holes is measured. Because fluorescence has a large probing depth (> 1 μm), this method has a higher bulk sensitivity than that of the total-electron-yield method. However, the signal intensity is weak and this method suffers from self-absorption effects, resulting in the complication of the data analysis.

2.3.4 X-ray magnetic circular dichroism

When a sample with magnetization (paramagnetic, ferromagnetic, and ferromagnetic materials) is irradiated with circular polarized x-rays, the resultant XAS spectra of the right-handed (σ^+) and left-handed (σ^-) circular polarized light, as shown in Fig. 2.10, are different because of the difference in transition matrix elements. X-ray magnetic circular dichroism (XMCD) is defined as the difference between the absorption spectra of x-rays of parallel and antiparallel polarity to the magnetization direction of the sample material. XMCD is an element specific measurement because the absorption process is originates from core electron excitation and its line shapes reflect the electronic structure related to the magnetism. In addition, XMCD sum rules enable us to estimate element-specific spin and orbital magnetic moments separately from the integrated intensities of the XAS and XMCD spectra. Typical XMCD spectra of iron reported by Chen *et al*. are shown in Fig. 2.11 [32].

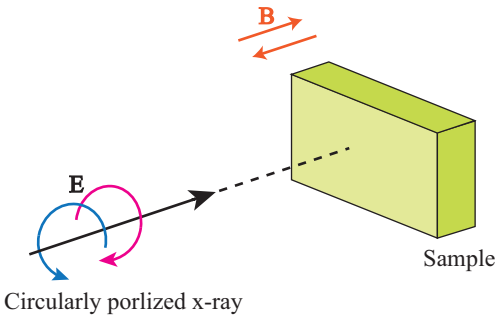

Figure 2.10: A schematic diagram of x-ray magnetic circular dichroism.

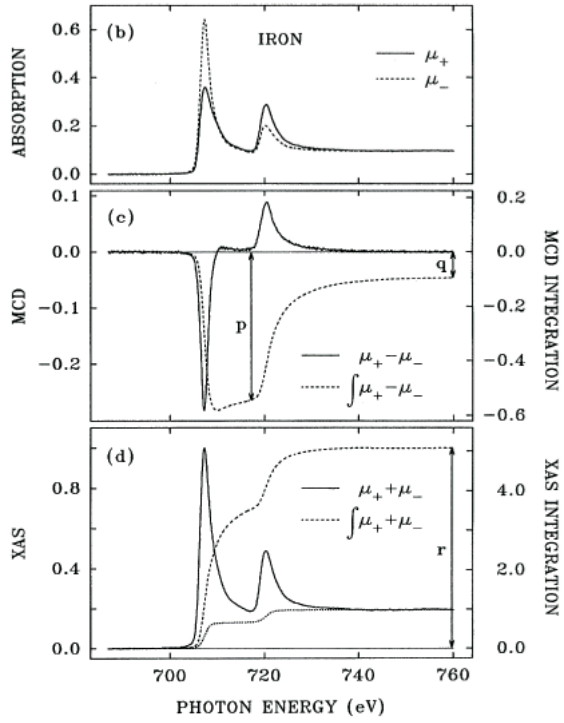

Figure 2.11: (b) Fe $L_{2,3}$ XAS spectra of measured by right-handed and left-handed circularly polarized x-rays. (c) Fe $L_{2,3}$ XMCD spectrum and its integration (dashed line). (d) Summed XAS spectrum and its integration (dashed line) [32].

For instance, let me consider $L_{2,3}$ XMCD (transition from $2p$ to $3d$). Figure 2.12 shows the transition matrix elements of $2p \rightarrow 3d$ absorption of σ^+ and σ^- for spin-down states. σ^+ (σ^-) increases (decreases) the z component of the orbital moment by 1. In the case that the majority spin states (spin-up) are fully occupied and the transition occurs only for minority spin (spin-down), the difference in intensity between σ^+ and σ^- are described by

$$L_3 : \Delta I_3 \propto 6h_{+2} + 6h_{+1} + (3-1)h_0 - 6h_{-1} - 18h_{-2}$$

$$L_2 : \Delta I_2 \propto 12h_{+2} + 3h_{+1} - 2h_0 - 3h_{-1} \quad (2.13)$$

where h_{md} is the hole number of each $3d$ state and its subscription m_d is the magnetic quantum number. Then, the orbital magnetic moment is proportional to the sum of the intensities as follows:

$$\Delta I_3 + \Delta I_2 \propto 18h_{+2} + 9h_{+1} - 9h_{-1} - 18h_{-2}$$

$$= 9(2h_{+2} + h_{+1} - h_{-1} - 2h_{-2})$$

$$= \sum_{m_d} m_d h_{md}$$

$$\propto \langle L_z \rangle. \quad (2.14)$$

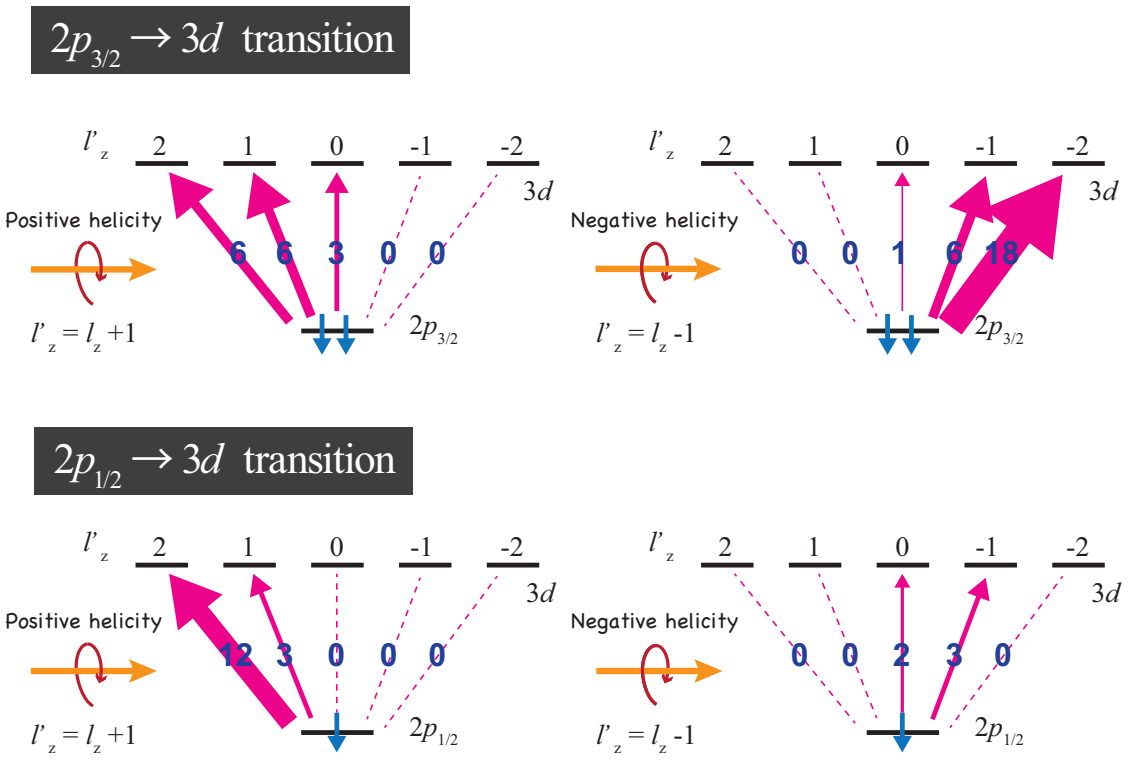

Figure 2.12: Transition matrix elements of $2p \rightarrow 3d$ absorption with circularly polarized x-rays for spin-down states

The spin magnetic moment is also estimated in the same manner. Thus, the orbital magnetic moment (M_{orb}) and the spin magnetic moment (M_{spin}) in units of μ_B/atom can be calculated by XMCD sum rules [33, 34] as follows:

$$M_{orb} = -\frac{2}{3}\frac{\int_{L_3+L_2}(\mu^+ - \mu^-)\,dE}{\int_{L_3+L_2}\left(\frac{\mu^+ + \mu^-}{2}\right)dE}(10 - N_d)$$

$$M_{spin}^{eff} = M_{spin} + 7M_T = -\frac{3\int_{L_3}(\mu^+ - \mu^-)\,dE - 2\int_{L_3+L_2}(\mu^+ - \mu^-)\,dE}{\int_{L_3+L_2}\left(\frac{\mu^+ + \mu^-}{2}\right)dE}(10 - N_d)$$

(2.15)

where μ^+ and μ^- are the absorption intensities of σ^+ and σ^-, respectively, and N_d is the number of *d* electrons of the specific atom. M_T is the magnetic dipole moment, which is small in the case of a high local symmetry of the transition-metal atomic site, and can be neglected in the case of perovskite oxides with cubic symmetry with respect to M_{spin}.

2.4 Experimental setup

2.4.1 Continuous composition spread-pulsed laser deposition system

In this work, a continuous composition spread-pulsed laser deposition (CCS-PLD) system was designed and fabricated to overcome the difficulty of obtaining a large area with homogeneous composition and thickness, which is a disadvantage of PLD. Figure 2.13 shows a schematic image of the CCS-PLD system. In PLD, the film thickness is distributed with a maximum just above the plume plasma. In the case of a 20 mmϕ circular target and a distance between the substrate and the target of 7 cm, the homogeneous thickness area is limited to less than 10 mm × 10 mm because the position of the plume is fixed. On the other hand, the developed CCS-PLD makes it possible to obtain an area of homogeneous thickness as large as 20 mm × 20 mm owing to the variation in plume position achieved by scanning the ablation laser, shown in Fig. 2.14. A film with a larger composition spread area enables the composition dependence of the physical properties of the film to be evaluated with a higher composition resolution. One can also fabricate films on several different substrates at a time. A KrF excimer

laser (248 nm) was used for target ablation. A Pt heater and the composite material heater with a carbon fiber core were adopted for sample heating and could heat samples to ~800 °C. The apparatus had no RHEED instrument. The developed CCD-PLD apparatus was used to fabricate La_2NiMnO_6 films.

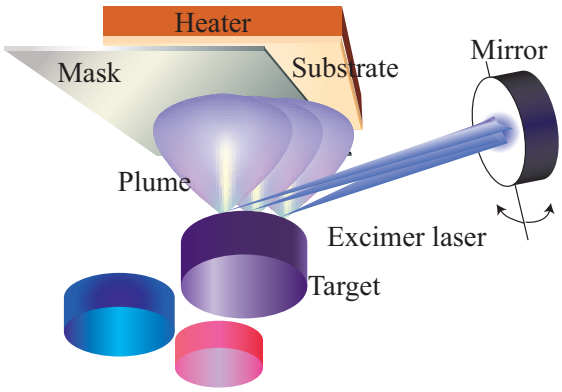

Figure 2.13: A schematic image of the CCS-PLD process. Plume position varies synchronizing the scans of the ablation laser on the surface of the target.

	Conventional PLD	CCS-PLD
Ablation laser	Fixed on a target	Scanning on a target
Target	Rotation	Fixed
Homogeneous thickness area	> 10 mm ×10 mm	20 mm × 20 mm
Thickness distribution	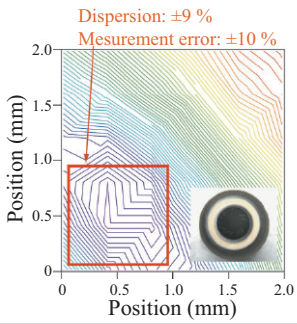	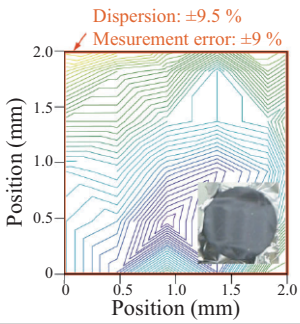

Figure 2.14: Comparison of homogeneous thickness area between a conventional PLD and the CCS-PLD.

2.4.2 *In situ* photoemission spectroscopy and laser molecular beam epitaxy system

Photoemission spectroscopy and x-ray absorption spectroscopy were performed using the *in situ* photoemission spectroscopy and laser MBE system [35] located at the undulator beamline of BL-2C [36] and Beamline MUSASHI (BL-2A) of KEK-PF. BL-2C had one undulator for soft x-rays (SX; 250–1400 eV). Beamline MUSASHI has two different undulators in a tandem configuration: One for vacuum ultra-violet (VUV) (30–300 eV) and the other for SX (250–2000 eV). The spot size at the sample position was 0.1 mm (vertical) × 0.5 mm (horizontal). The E/ΔE energy resolution is over 20,000 and over 10,000 for about 65 eV and from 250 eV to 900 eV, respectively. In VUV mode, vertical and horizontal linearly polarized radiation as well as left and right handed circularly polarized radiation can be used. High-energy resolution and high flux beam are supplied for the 30 eV to 250 eV energy range at Beamline MUSASHI. It was possible to easily switch between VUV and SX mode for different purposes. As shown in Figs. 2.15, the system consists of four chambers separated from each other by gate valves to maintain ultrahigh vacuum; (1) load lock chamber, (2) preparation chamber, (3) photoemission and x-ray absorption chamber, and (4) Laser MBE chamber. Samples are transferred under the ultrahigh vacuum condition using two sample banks and three transfer rods connected between (1) and (2), (2) and (3), and (2) and (4).

(1) Load lock chamber

The chamber for sample installation.

(2) Preparation chamber

In this chamber, samples are stored and low-energy electron diffraction (LEED) and Auger measurements are performed.

(3) Photoemission and x-ray absorption chamber

Gummadata Scienta SES-100 and SES-2002 electron energy analyzers are used at BL-2C and Beamline MUSASHI, respectively. X-ray absorption spectroscopy is carried out by measuring the compensation currents toward the sample holder from the earth. The chamber is equipped with a five-axis (x, y, z, θ and tilt) manipulator, called *i*-Gonio, which has liquid-He cryo and Si heating systems for temperature dependence measurements.

(4) Laser MBE chamber

A combinatorial laser MBE system (Mobile combi-PLD, PASCAL) has been designed with some smaller components for use in the limited space around the beamlines of KEK-PF. A 3rd-harmonic generation Nd-YAG solid-state laser (355 nm) is used for target ablation and its maximum power is about 100 mJ. A smaller continuous-wave semiconductor laser (808 nm) was used for sample heating, and its maximum output is about 100 W. This system can heat samples up to ~1200 °C. The RHEED instrument has a differential pumping system to make the monitoring during the high-pressure (~10^{-3} Torr) growth possible. LabVIEW programs are used to control all operations. The apparatus was used to fabricate $LaNiO_3$-$LaMnO_3$ and $LaMnO_3$-$SrTiO_3$ heterostructures.

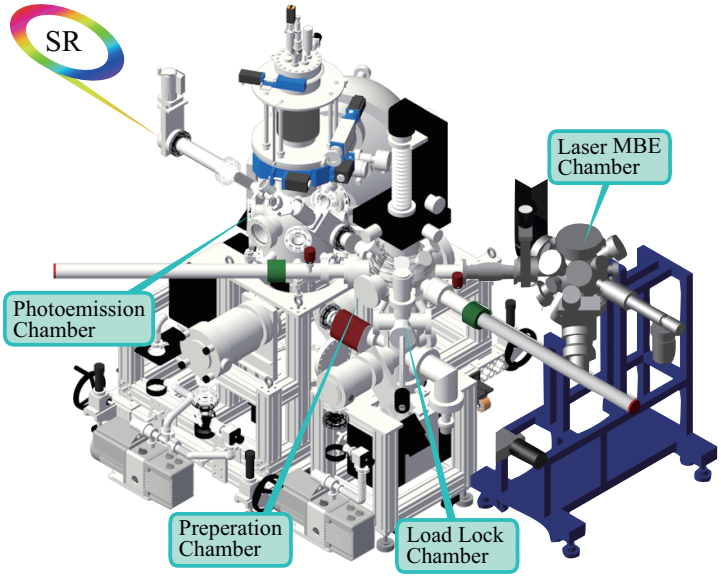

Figure 2.15: A schematic image of *in situ* photoemission spectroscopy and laser MBE system

2.4.3 X-ray magnetic circular dichroism measurement

X-ray magnetic circular dichroism measurement (XMCD) was performed using XMCD apparatus equipped with normal conducting coil magnets at the undulator beamline of BL-16A, KEK-PF. This apparatus can apply a maximum magnetic field of 1.2 T. It is equipped with a four-axis (x, y, z, θ) manipulator with a liquid-He cryostat for low temperature measurements. It is possible to use the total-electron-yield mode and total-fluorescence-yield mode with a microchannel plate detector. In this work, the total-electron-yield mode was used, in which the compensation currents to the sample were measured. BL-16A supplies not only vertical and horizontal linearly polarized radiations but also right-handed and left-handed

circular and elliptically polarized radiations in an energy range from 250 eV to 1500 eV [37]. In BL-16A, twin APPLE-II type undulators have been installed in a tandem configuration and the polarized radiation is switched at a frequency of 10 Hz by kicker magnets [38], resulting in the measurement of very small XMCD and XMLD signals. This yields a noise level of much less than 0.1 % in XMCD, as well as real-time observations of the changes in the dichroic signal [39]. The degree of circular polarization is ±95 % ±4 %.

2.4.4 Synchrotron radiation

When charged particles, particularly electrons, are accelerated close to the speed of light by a linear accelerator (Linac) and circular accelerator (Synchrotron) and bended by some magnets, photons are emitted in a narrow cone along the forward direction, called “synchrotron radiation”. The brilliance and directionality of synchrotron radiation improve with increasing electron speed and the degree of bending. Synchrotron radiation is characterized by high brilliance, high polarization, high directivity, short pulse, and wide energy spectrum. To generate the synchrotron radiation, three types of magnets are commonly used, bending, undulator insertion device, and wiggler insertion device. Bending magnets are used in the storage ring and synchrotron radiation generated by bending magnets has vertical directivity but horizontal isotropicity. It is white light with a peak in intensity at certain energy and is less bright than that generated by insertion devices. Insertion devices, in which electrons oscillate in a periodic magnetic field produced by a series of magnets, can generate brighter light. The light emitted by each serpentine motion are coherently added in the undulator insertion device,

whereas incoherently in the wiggler insertion device. Synchrotron radiation generated by the undulator has a sharp directionality and is a quasi-monochromatic with higher order light. In contrast, that generated by the wiggler is white light with higher brilliance.

In this work, undulator beamline BL-2C, MUSASHI (BL-2A) of KEK-PF was used for photoemission spectroscopy and x-ray absorption spectroscopy measurements, and BL-16A of KEK-PF was used for x-ray magnetic circular dichroism measurements. Bending beamlines BL-4C and BL-7C of KEK-PF were used for x-ray diffraction measurements.

Chapter 3

Optimization of growth condition of double perovskite oxides La_2NiMnO_6

3.1 Introduction

3.1.1 Double perovskite

Perovskite oxides have the chemical formula ABO_3, which contain a framework of corner-shared BO_6 octahedra and A cations in 12-coorinate sites. Double perovskite oxides has two different A and/or B cations which form superstructures by some kinds of A and/or B cation ordering, resulting in that their unit cell is twice that of a perovskite. $CaCu_3Ti_4O_{12}$ is one of the examples of A-site ordering double perovskite, in which Ca^{2+} and Cu^{2+} ions form an ordered structure [40] due to the nature of the Jahn-Teller Cu^{2+} ion. On the other hand, double perovskite oxides, which contain two kinds of B site cations, are described by the chemical formula $A_2BB'O_6$ and there are three different types of BO_6 octahedral arrangement: Random distribution, layered type ordering, and rock-salt type ordering as shown in Fig. 3.1. The spontaneous ordering of BO_6 and $B'O_6$ octahedra requires a larger difference in ionic radius and the formal valence between B and B" ions [41]. Disordering easily occurs in the case that the formal valence difference is less than 3 or ionic radius difference is less than 0.2 Å between B

and B" ions. For example, La_2FeCrO_6 and Bi_2FeCrO_6 have a random arrangement of FeO_6 and CrO_6 octahedra in bulk phase, because both Cr and Fe ions are trivalent [42, 43, 44]. A rare example exhibiting layered typeordering is Ca_2CuSnO_6. The layer of Jahn-Teller ion Cu^{2+} (d^9) and that of non Jahn-teller ion Sn^{4+} (d^{10}) stack alternatively along (001) direction, which is observed by a transmission electron microscope (TEM) (Fig. 3.2) [45]. In rock-salt type double perovskite oxides, BO_6 and $B'O_6$ octahedra arrange alternatively in all direction, resulting in the formation of B-O-B' bonds in all direction. This structure can be a (111)-oriented "natural superlattice" in which 1-monolayer (ML) ABO_3 and 1-ML $AB'O_3$ stack alternatively along (111) direction, as shown in Fig. 3.1. The most studied double perovskite oxide with rock-salt type ordering is Sr_2FeMoO_6. It is a half-metallic material exhibiting a magnetoresistance [46]. La_2NiMnO_6 (LNMO) is also a rock-salt type double perovskite oxide with NiO_6 and MnO_6 arrangement.

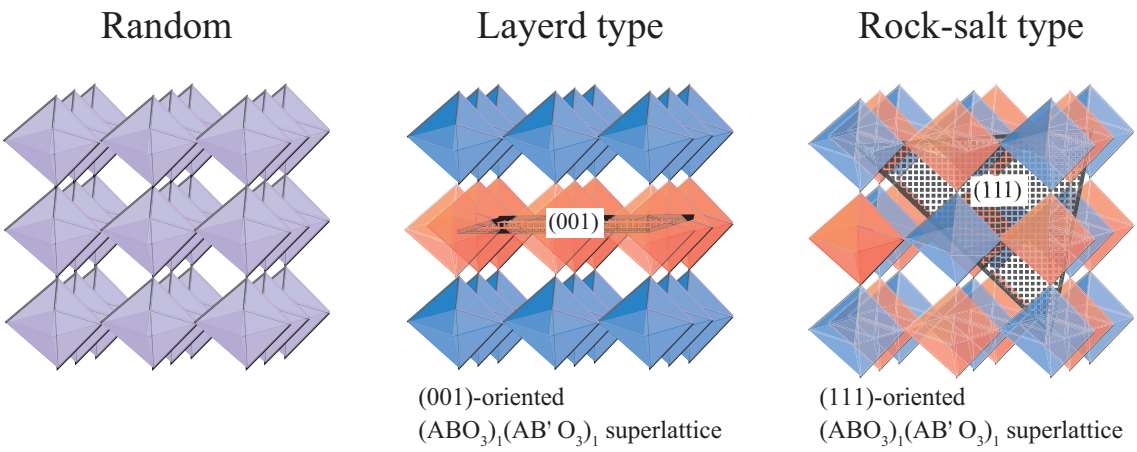

Figure 3.1: Three types of double perovskite oxides $A_2BB'O_6$ (red: BO_6, blue: $B'O_6$)

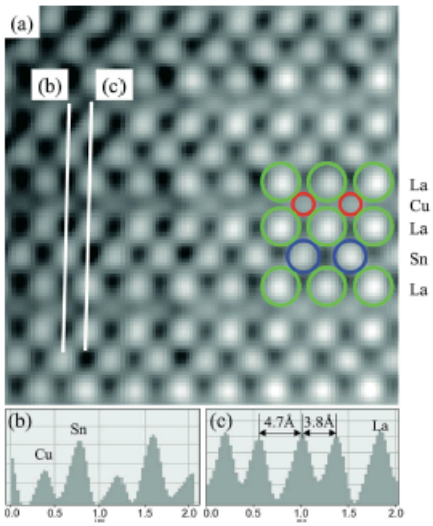

Figure 3.2: A scanning-TEM image of layered type double perovskite oxide Ca_2CuSnO_6 films [45].

3.1.2 Previous studies of La_2NiMnO_6

LNMO is a ferromagnetic semiconductor with rock-salt type ordering of NiO_6 and MnO_6 octahedra. It has a ferromagnetic transition temperature (T_C) near room temperature (~ 280 K) and saturated magnetic moment of 4 ~ 5 μ_B/f.u., while $LaMnO_3$ (LMO) is an antiferromagnetic insulator in stoichiometric bulk phase and $LaNiO_3$ (LNO) is a paramagnetic metal. LNMO shows a great advantage compared with other ferromagnetic semiconductor exhibiting a ferromagnetic ordering at very low temperature [e.g., EuO (T_C = 77 K) [47], $CdCr_2Se_4$ (T_C = 130 K) [48], $SeCuO_3$ (T_C = 25K) [49], and $BiMnO_3$ (T_C = 100 K) [50]. It also has a superiority over diluted ferromagnetic semiconductors such as (Ga,Mn)As (T_C <= 160 K)

[51, 52], Co:ZnO (T_C = 300 K) [53], Co:TiO_2 (T_C > 400 K) [54, 55], and Co:$SnO_{2-\delta}$ (T_C = 650 K) [56] in terms of its intensity of the saturated magnetization. Moreover, as shown in Fig. 3.3, large magnetocapacitance and magnetoresistance effects of single-phase bulk LNMO have been reported near room temperature [57], suggesting that the possibility of application of LNMO for realistic devices used with solid-state thermoelectric (Peltier) coolers. It has also reported that ferromagnetic semiconductor LNMO has applied as a barrier in a spin-filter tunneling junction [58] and a spin-pumping insulator for generating spin-current [59].

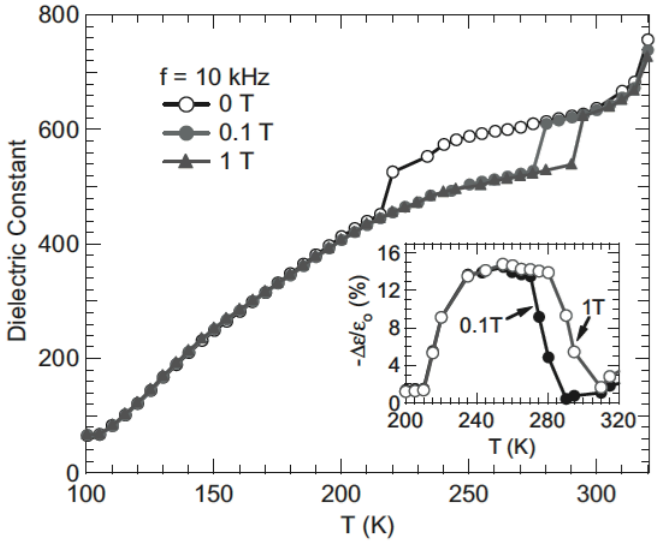

Figure 3.3: Temperature dependence of the dielectric constant of LNMO. The inset shows the magnetocapacitance effect [57].

Bulk LNMO has been studied over years in order to obtain better understandings of the magnetic exchange interaction in this compound. As for its spin states and magnetic

interactions, there are some controversies concerning the nature of magnetic coupling. In the earliest study, LNMO showed a relative conduction and no sign of B-site ion ordering. Thus, the observed ferromagnetic behavior was considered to be due to the vibronic ferromagnetic superexchange interaction between two Jahn-Teller ions of Ni^{3+} ($t_{2g}^6e_g^1$) and Mn^{3+} ($t_{2g}^3e_g^1$) [60, 61]. On the other hand, Blasse *et al*., argued that ferromagnetism of LNMO is attributed to Ni^{2+} ($t_{2g}^6e_g^2$)-O-Mn^{4+} ($t_{2g}^3e_g^0$) superexchange interaction based on their magnetic susceptibility data [62]. Since then, number of reports, including magnetic studies, ^{55}Mn NMR [63, 64], and x-ray absorption near-edge spectroscopy (XANES) [65] have supported that the superexchange interaction between Ni^{2+} and Mn^{4+} ions is the origin of ferromagnetic nature of LNMO, while two neutron diffraction studies reported disagree the oxidation states of Ni and Mn ions: Blasco *et al*., the formal valences of Ni and Mn are 2+ and 4+ respectively [66], whereas Bull *et al*., Ni^{3+} and Mn^{3+} Jahn-Teller ions are present in LNMO [67].

As for the crystal structure, LNMO with random distribution of NiO_6 and MnO_6 octahedra shows biphasic with orthorhombic *Pbnm* phase at low temperature that transforms to rhombohedral *R*3-*C* phase at high temperature. Rock-salt-type ordering of Ni and Mn ions transforms the orthorhombic *Pbnm* to the monoclinic $P2_1/n$ and the rhombohedral *R*3-*C* to *R*3-*m* or R3-. Both monoclinic and rhombohedral ordered phases show ferromagnetic properties with comparable values of T_C ~ 280 K [68]. High temperature rhombohedral phase and low temperature orthorhombic/monoclinic one coexist over a wide temperature range, including room temperature.

Synthesis conditions of LNMO have a large influence on its magnetic properties. As shown in Fig. 3.4 and Fig. 3.5, ordered LNMO grown under the carefully controlled condition

show a single ferromagnetic-paramagnetic transition temperature of about 280 K and saturated magnetic moment of 4~5 μ_B/f.u. [57, 69].

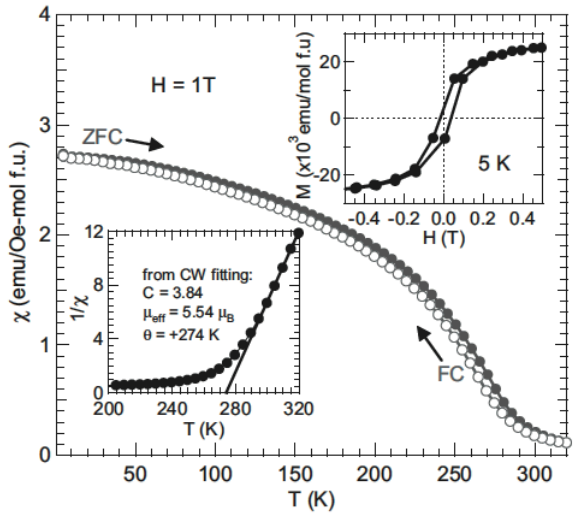

Figure 3.4: Temperature (T) dependence of magnetic susceptibility (χ) of LNMO. The inset shows 1/χ-T plot (lower left) and field dependent of magnetization (upper right) [57].

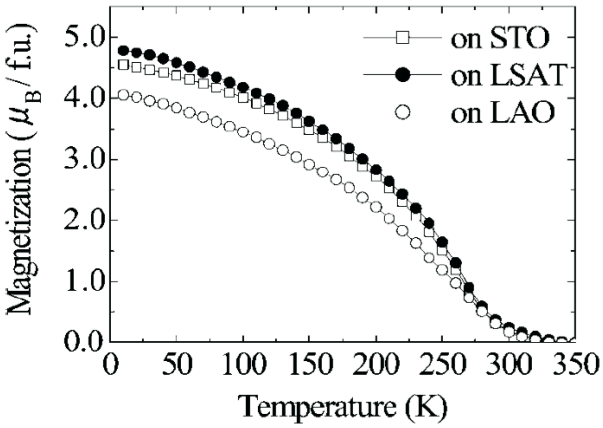

Figure 3.5: Temperature dependence of magnetization of LNMO epitaxial thin films. [69].

On the other hand, Joly *et al*., showed two different T_C derived from different combinations of Ni and Mn spin states: Low-T_C phase is due to Ni^{2+} and Mn^{4+} and high T_C phase contains Ni^{3+} and Mn^{3+}, as shown in Fig. 3.6 [70]. Dass *et al*., reported various temperature dependence of magnetization curves of bulk LNMO synthesized under difference conditions, shown in Fig. 3.7 and argued that low-T_C and high-T_C phase contain Ni^{3+}-Mn^{3+} and Ni^{2+}-Mn^{4+}, respectively [68], which is supported by studies of LNMO film [71]. As shown in Figs. 3.8 and 3.9, oxygen pressures during the deposition of LNMO film greatly affected its saturated magnetic moments and high oxygen pressure is necessary to attain the value close to spin-only ones (5 μ_B/f.u.) [69, 72].

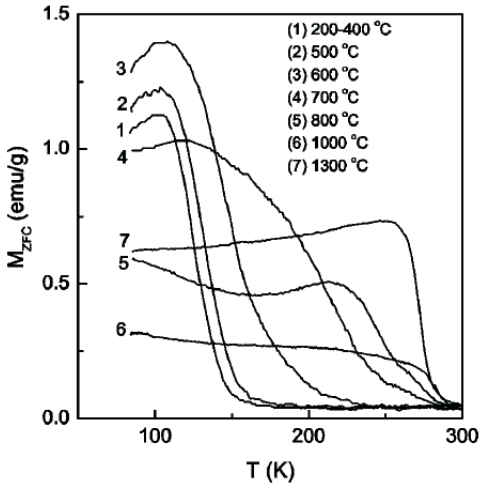

Figure 3.6: Temperature dependence of magnetization curves of $LaNi_{0.5}Mn_{0.5}O_3$ bulk samples annealed under the various temperatures [70].

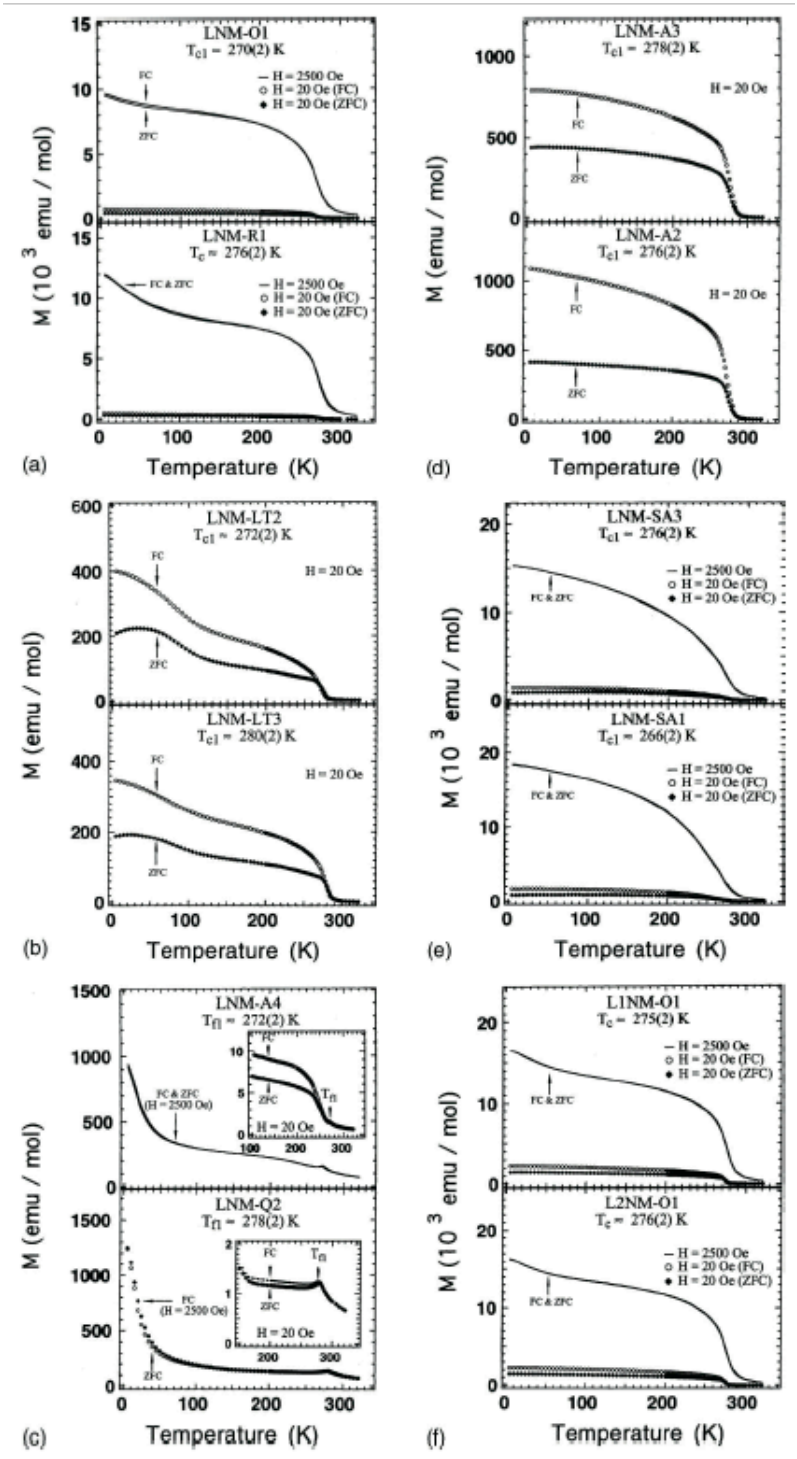

Figure 3.7: Temperature dependence of magnetization curves of LNMO bulk samples synthesized under the various conditions [68].

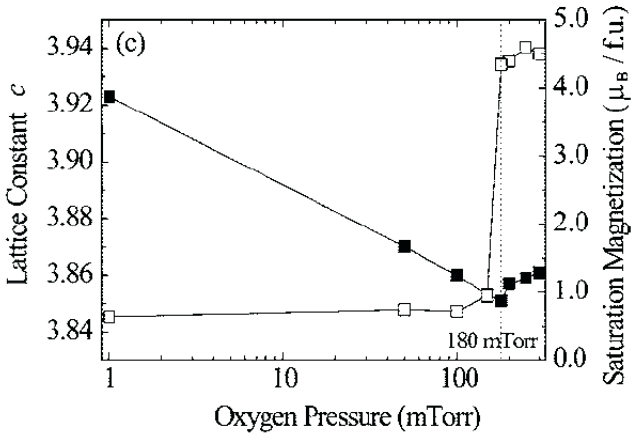

Figure 3.8: Saturation magnetizations measured in the field of 1 T at 5 K of LNMO films grown under the various oxygen pressure [69].

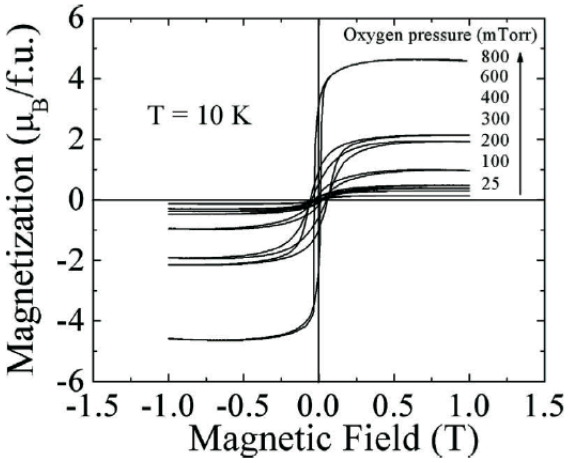

Figure 3.9: Hysteresis curves of LNMO films grown under the various oxygen pressure [72].

3.1.4 Purpose of this study

In order to investigate the interface between LNO and LMO, I have focused on double perovskite LNMO, which can be regarded as a "natural superlattice" of LNO and LMO, as a first step. As mentioned above, synthesis conditions of LNMO largely affect on its magnetic properties since the origin of ferromagnetism can be explained by the ferromagnetic superexchange interaction between Ni and Mn ions through oxygen. Defects, cation valencies and arrangement of B-site ions largely depending on synthesis conditions strongly influence on magnetic properties. Besides, it is necessary to fabricate it in thin film form for applying as spintronics devices. For device applications as well as a fundamental understanding of magnetic exchange interactions in LNMO, systematical understanding of the relationship between LNMO epitaxial thin film growth conditions and its magnetic properties is significantly important. In this study, I have investigated the dependence of magnetic properties on growth conditions, especially growth temperature and oxygen pressure. I have optimized the growth conditions of LNMO film that shows higher ferromagnetic transition temperature and higher magnetic moment.

3.2 Experiments

LNMO films were grown on (001) $SrTiO_3$ (STO) substrates by pulsed laser deposition (PLD) techniques in a continuous composition spread (CCS) - PLD chamber. A polycrystalline

stoichiometric LNMO target fabricated with conventional solid state reactions was ablated by KrF excimer laser (λ = 248 nm) with a repetition rate of 5 Hz. During deposition, STO substrates were kept in the 600 - 750 °C temperature range and pure oxygen gas of 10 - 1100 mTorr was continuously supplied into the growth chamber. Laser powers of the ablation are 0.5 J/cm^2 and 0.3 J/cm^2 under the oxygen pressure more than 180 mTorr and less than 50 mTorr, respectively. After thin film growth, films were cooled down to 500 °C with the rate of 15 °C /min. Then, the growth chamber was filled with 760 Torr pure oxygen gas and subsequently films were cooled down to room temperature. Out-of-plane lattice parameters and crystalline qualities were evaluated by x-ray diffraction (XRD). A Quantum Design, superconducting quantum interference device (SQUID) magnetometer was used to investigate magnetic properties of LNMO films. The compositions of the films were determined by x-ray fluorescence (XRF) (μEDX-1300, Shimazu) using a stoichiometric LNMO target as a reference. Synchrotron-radiation x-ray diffraction (SR-XRD) was carried out at BL-4C of KEK-PF.

3.3 Results and Discussion

In an attempt to explain the influence of growth conditions simply, I focus on x-ray diffraction patterns and magnetic properties of representative LNMO films grown under four different conditions of growth temperature and oxygen pressure, 700 °C, 500 mTorr for sample A, 750 °C, 1100 mTorr for B, 600 °C, 500 mTorr for C, 700 °C, 190 mTorr for D, respectively, as summerized in Table 3.1.

Table 3.1: Growth conditions of samples A - D

	A	B	C	D
Temperature (°C)	700	750	600	700
Oxygen pressure (mTorr)	500	1100	500	190

3.3.1 Crystalinity of La_2NiMnO_6

Crystal structures of LNMO films were characterized by XRD. Figure 3.10 shows XRD $2\theta/\theta$ patterns of LNMO films grown under the four different growth conditions (A-D).

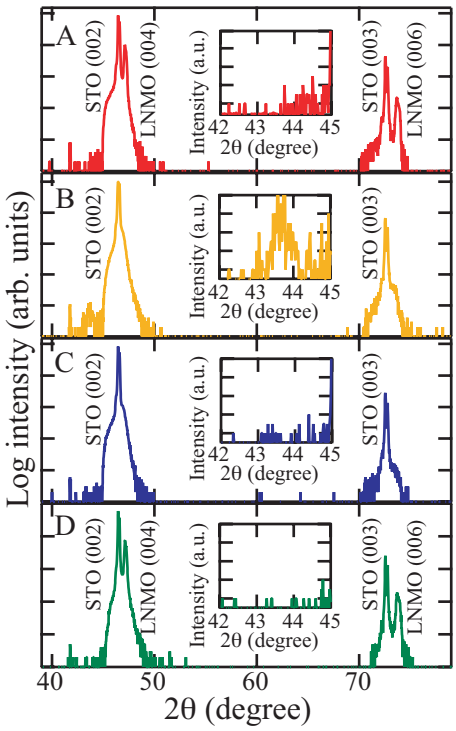

Figure 3.10: $2\theta/\theta$ XRD patterns for LNMO films grown on (001) $SrTiO_3$ substrates under four different growth conditions. The insets show $2\theta/\theta$ XRD patterns of secondary phases. XRD patterns are for (a) sample A, (b) sample B, (c) sample C, (d) sample D, respectively.

Sharp (*00l*) diffraction peaks of LNMO were clearly observed in samples A and D, indicating that LNMO films were epitaxially grown on (001) STO substrates. XRD superstructure peaks of double perovskite unit cell (*00l*) with *l* of odd numbers, are not seen because of the extinction rule of face-centered symmetry [73]. The full widths at half maximum (FWHM) of rocking curves for LNMO (004) diffraction peaks are 0.058 ° and 0.053 ° for sample A and D, respectively. These FWHMs are almost equal to those of STO substrates (0.053 ° - 0.055 °), indicating that LNMO films have high crystalline qualities. High crystalline qualities of samples A and D are also confirmed by the fact that observed (*00l*) peaks have doublet structures due to Cu $K_{\alpha1}$ and $K_{\alpha2}$ of x-ray source. Out-of-plane lattice parameters are 3.85 Å for samples A and D, which is a slightly smaller value than the pseudo-cubic perovskite lattice parameter of bulk LNMO (3.879 Å) reported by Rogado *et al*. [57]. This difference may be caused by the tensile strain in lateral direction from STO substrates (3.905 Å). In order to evaluate the in-plane orientation between LNMO film and the STO substrate, reciprocal space mapping of sample A was performed using SR-XRD. Figure 3.11 shows a reciprocal space mapping around (103) reciprocal point, where the reciprocal-space coordinates correspond to the cubic STO substrate. Both diffraction peaks of a STO substrate and the LNMO film clearly observed at the same *H*, which means the LNMO film coherently grows on STO substrate with the in-plane lattice constant matching that of a STO substrate. For samples B and C, LNMO diffraction peaks are not observed. Beside, there is a secondary peak probably assigned as NiO and/or La_2NiO_4 only in the sample B diffraction pattern. Since the existence of this secondary phase in sample B makes the crystalline quality of LNMO worse, LNMO peaks are not observed in the diffraction pattern. On the other hand, for sample C, the absence of LNMO peaks may be due to poor

crystalline quality because of low growth temperature. Comparing A and D to C, it would be suggested that higher growth temperature is essential for good crystalline films. A series of (002) XRD patterns shown in Fig. 3.12 and the map summarized of 19 XRD patterns grown under the various temperature and oxygen pressure, as shown in Fig. 3.13, also suggest the same trend.

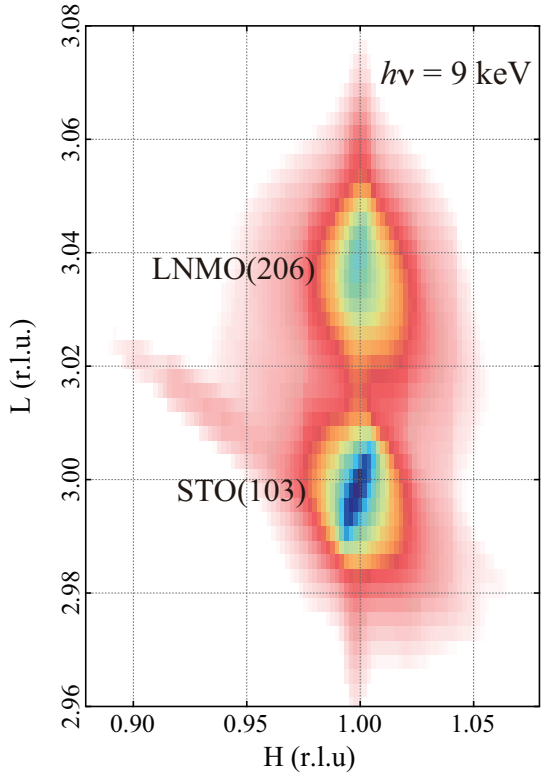

Figure 3.11: Reciprocal space mapping around (103) reflection for sample A. The reciprocal-space coordinates correspond to the cubic STO substrate.

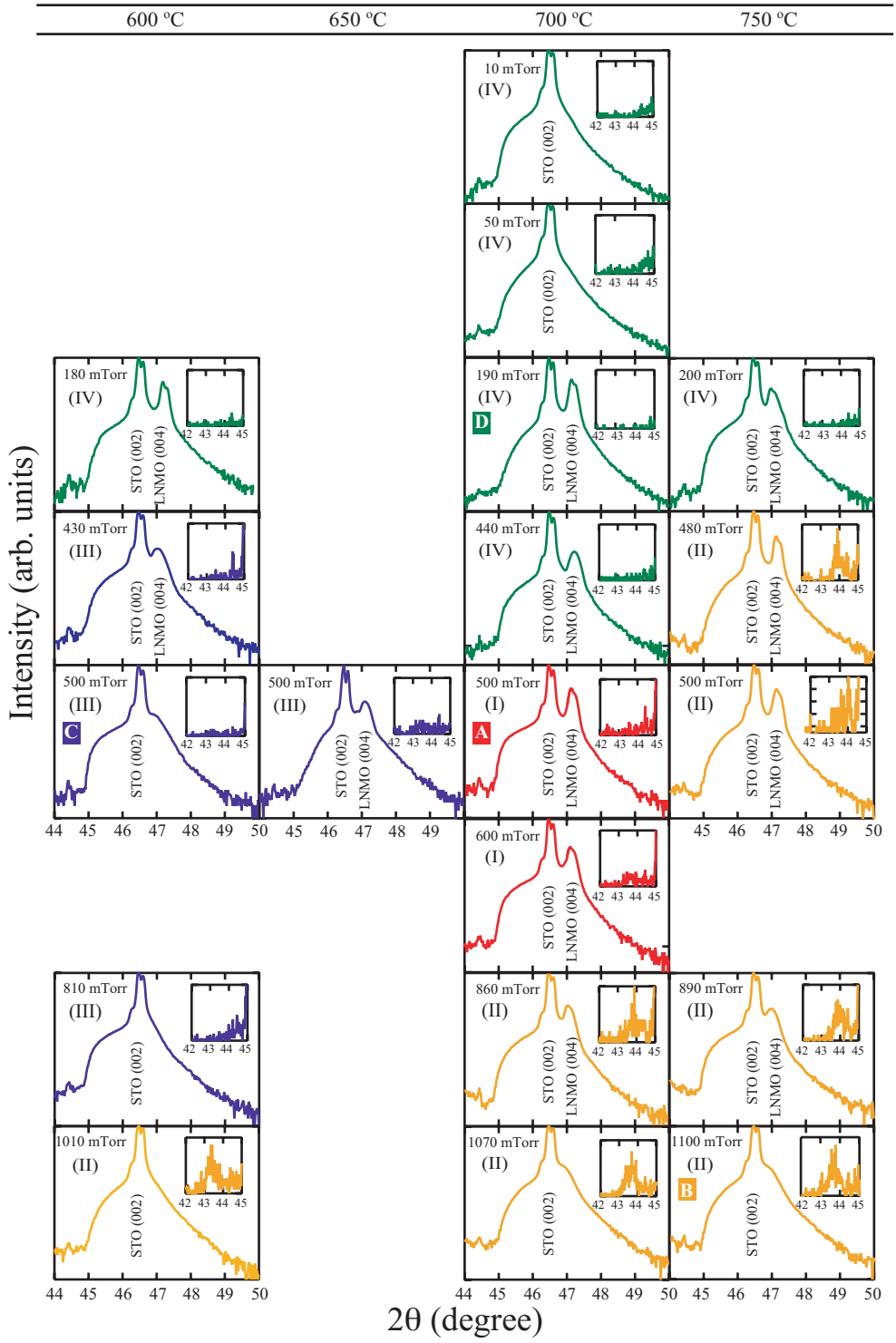

Figure 3.12: $2\theta/\theta$ XRD patterns around (002) reflection for LNMO films grown under the various growth conditions.

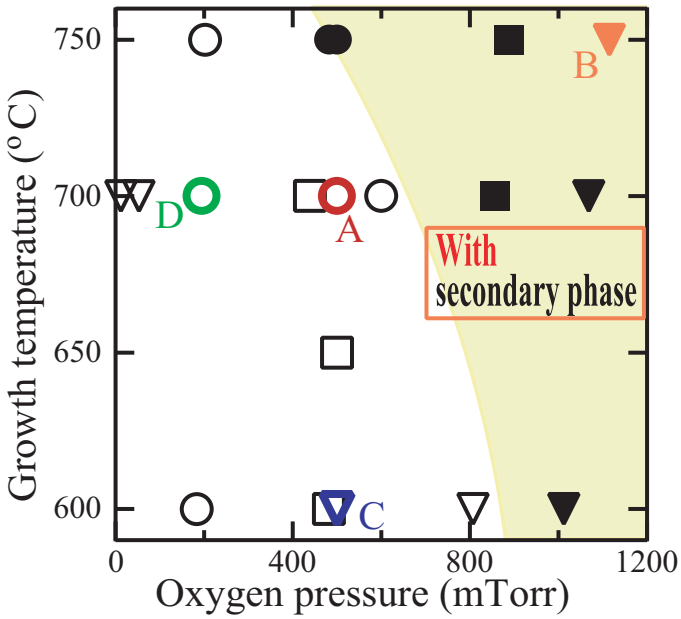

Figure 3.13: Map of crystal qualities depending on growth temperature and oxygen pressure. Each symbol represents the crystallinity of LNMO films. High and moderate crystal qualities were denoted by circle and square symbols, respectively. Highly crystalline LNMO films show doublet (004) peaks owing to Cu $K_{\alpha1}$ and $K_{\alpha2}$ radiations in XRD patterns. Films having no LNMO diffraction peaks were displayed by triangle. Films with (filled) and without (open) secondary phases are also shown.

3.3.2 Magnetic properties of La_2NiMnO_6

Various magnetic properties were observed for LNMO films which show different XRD patterns. Temperature and magnetic field dependences of the magnetization (M-T and M-H curves) of samples A to D are shown in Fig. 3.14 and Fig. 3.15 respectively. Magnetic

field conditions exhibiting maximum magnetic moments in raw M-H hysterisis curves are employed for M-T measurements in order to minimize the demagnetizing effects, as shown in the inset of Fig. 3.14.

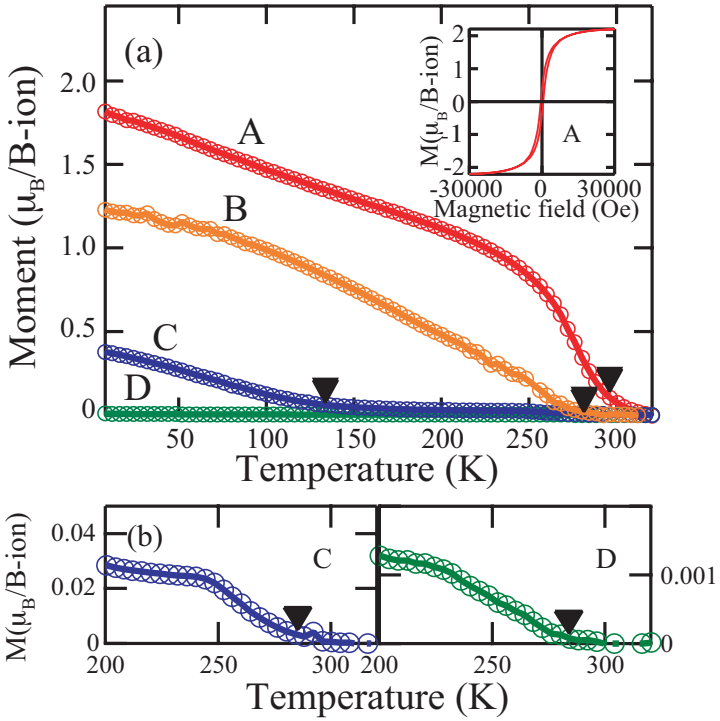

Figure 3.14: Temperature (T) and magnetic field (H) dependences of the magnetization (M) for LNMO films. (a) M-T curves under field cool for samples A through D. The inset displays the raw M-H curve of sample A measured at 8 K. Applied magnetic fields (denoted by the allow) for M-T measurements were determined based on the raw M-H curves, 7500 Oe for sample A, 2000 Oe for B, 4000 Oe for C and 200 Oe for D, respectively.▼ for each sample was determined by the cross point of the extrapolating line at the transition edge and a background one. (b) M-T curves around T_C for samples C and D.

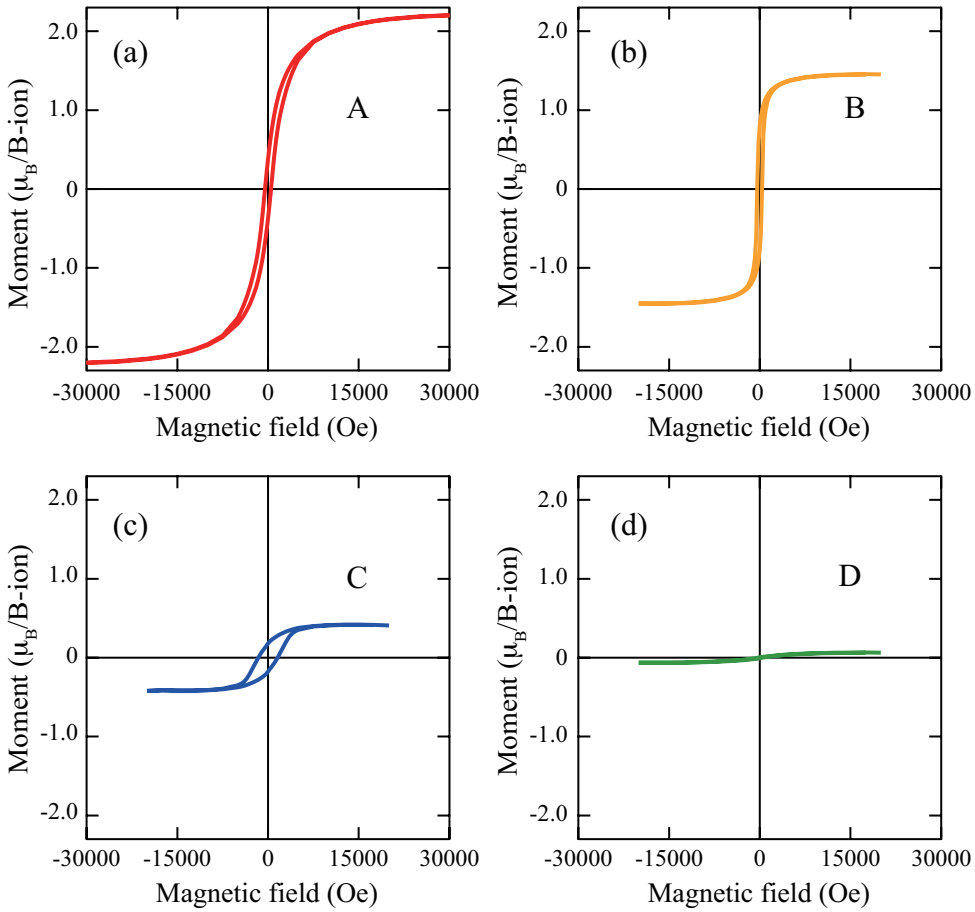

Figure 3.15: M-H hysterisis curves measured at 8 K of (a) sample A, (b) sample B, (c) sample C, and (d) sample D, respectively.

Sample A shows a clear ferromagnetic-paramagnetic transition at about 290 K. Saturated magnetization measured at 8 K is ~ 2.2 μ_B/B-site ion, as shown in Fig. 3.15. This is almost equal to the reported magnetization for ferromagnetic interaction of Ni^{2+} and Mn^{4+} in bulk and film LNMO [57, 68, 69, 72]. For sample B, magnetic moment gradually decreased with

increase of temperature and obscure transition was observed at about 280 K. Comparing samples A and B, sharp ferromagnetic transition around 290 K was observed in sample A which has a high crystalline quality phase and no secondary phases. On the other hand, obscure transition in M-T curve of sample B could be caused by the existence of secondary phases (NiO and/or La_2NiO_4) exhibiting antiferromagnetism. Sample C shows two different values for T_C of about 130 K and 290 K. Two different values for T_C may reflect the different ferromagnetic phases. Sample D has very small magnetic moment and T_C of about 280 K. Saturated magnetic moments and coercive fields measured at 8 K, and transition temperatures for samples A to D are summarized in Table 3.2.

Table 3.2: Magnetic properties of samples A - D

	A	B	C	D
Saturated magnetization (μ_B/B-ion)	2.2	1.4	0.42	0.064
Coercive field (Oe)	500	400	1600	380
Transition temperature (°C)	290	280	130, 290	280

Figure 3.16 depicts crystalline qualities and magnetic properties mapped in a growth temperature - oxygen pressure diagram on the basis of 10 M-T curves and 19 XRD patterns of LNMO films grown under the various growth temperature and oxygen pressure.

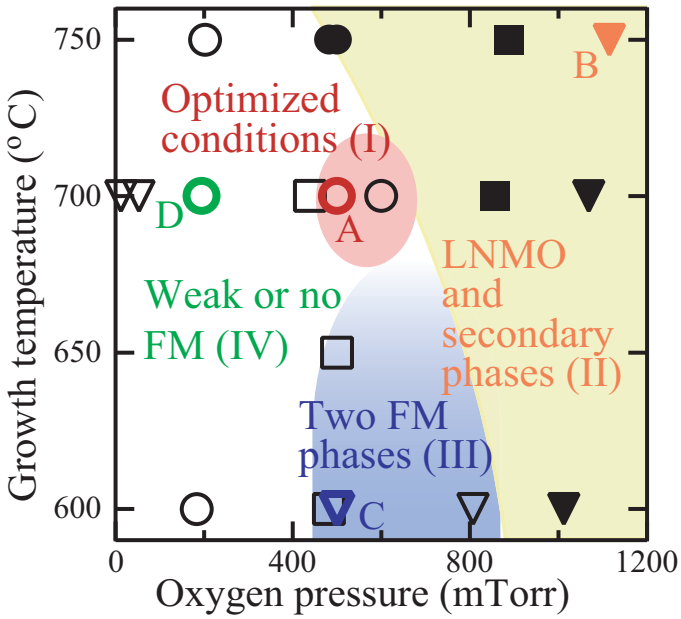

Figure 3.16: Map of crystal qualities and magnetic properties depending on growth temperature and oxygen pressure. Each symbol represents the crystallinity of LNMO films. Symbols are same with those in Fig. 3.12. High and moderate crystal qualities were denoted by circle and square symbols, respectively. Films having no LNMO diffraction peaks were displayed by triangle. Films with (filled) and without (open) secondary phases are also shown. LNMO films can be classified into four regions, (I) through (IV).

In the high growth temperature and high oxygen pressure region colored in yellow (region (II)), the existence of secondary phases was confirmed and films show obscure T_C. Table 3.3 shows cation concentrations evaluated by XRF measurements. Concentrations of Ni, Mn, and La were determined by sensitivity coefficients of Ni K_α, Mn K_α, and La L_α, respectively. LNMO films in region (II) have a large amount of La deficiencies and the ratio of La to (Ni + Mn) is about 0.64

evaluated by XRF measurements. La deficiencies may be induced by oxygen excess in LNMO due to high oxygen pressure in this region. Because it is difficult to introduce the oxygen interstitial into the perovskite structure, the excess oxygen tends to be accommodated by creating cation vacancies [74, 75]. It has been reported that oxygen excess is accommodated by vacancies preferentially on La site in $LaMnO_{3+\delta}$ [76]. In LNMO, it has also been reported that the excess oxygen has a preference for creations of La vacancies over those of Ni and Mn vacancies and these La deficiencies may induce the formation of secondary phases [68].

Table 3.3: Cation ratio of samples A - D evaluated by XRF measurement

	A 700 °C 500 mTorr	With secondary phases 700 °C 1100 mTorr	C 700 °C 500 mTorr	D 700 °C 190 mTorr	**ideal**
Ni mol %	25.7±0.2	34.2±1.1	26.3±0.2	24.5±0.3	**25**
Mn mol %	25.3±0.2	26.7±1.1	26.1±0.3	24.0±0.6	**25**
La mol %	49.0±0.2	39.1±1.1	47.0±0.3	51.5±0.8	**50**
A-site/B-site	0.96±0.01	0.64±0.03	0.91±0.01	1.06±0.03	**1**
Ni/Mn	1.02±0.01	1.28±0.08	1.01±0.02	1.02±0.02	**1**

In the blue region (region (III)) where growth temperature is low and oxygen pressure is relatively high, LNMO films have two different ferromagnetic phases. Minor ferromagnetic phase observed around 290 K can be explained by Ni^{2+}-O-Mn^{4+} superexchange ferromagnetic interaction [57], while other interactions may contribute to majority ferromagnetic phase exhibiting T_C of about 130 K. In this region, growth temperature may not be sufficient to

promote the rock salt type ordering of Ni and Mn ions. In order to evaluate the B-site ion ordering, the $\theta/2\theta$ XRD measurements along (*lll*) direction were performed for samples A and C [77]. The (*lll*) diffraction peals with *l* of odd number, which are derived from the superstructure due to B-site ion ordering, were suppressed for sample C while they were clearly observed for sample A [77, 78], indicating B-site ion ordering has not developed in sample C compared to sample A exhibiting good ferromagnetism. In suppressed B-site ion ordering, there might be not only Ni-O-Mn ordering but also locally Ni-O-Ni and Mn-O-Mn arrangements. In this local Mn-O-Mn arrangement, there is a possibility that Mn exists in not only Mn^{4+} but also Mn^{3+} states resulting in the local ferromagnetic states as observed in $Ca_{1-x}La_xMnO_3$ [79] and ferromagnetic interaction $LaMnO_{3+\delta}$ prepared under the oxidized conditions [80, 81], as shown in Figs. 3.17 and 3.18. In fact, $Ca_{1-x}La_xMnO_3$ show T_C of about 130 K [79] and semiconducting $LaMnO_{3+\delta}$ show T_C of about 110 - 160 K [80], which are close to the value observed for majority ferromagnetic phases of sample C. Singh *et al*., reported two ferromagnetic phases: A clear magnetic transition at 270 ~ 295 K as well as a minor transition at about 140 K ~ 150 K in the LNMO flim with absence of Ni/Mn long range ordering, as shown in Figs. 3.19 and 3.20 [71, 82]. They have demonstrated that Ni^{3+}-O-Mn^{3+} superexchange interaction is responsible for the low T_C phase, while Ni^{2+}-O-Mn^{4+} superexchange interaction is for the high T_C phase. However, Ni^{3+}-O-Mn^{3+} superexchange interaction is less likely to occur because my XAS results suggested that Ni^{2+} and Mn^{4+} are dominant on sample B and their amounts are almost the same with sample A exhibiting good ferromagnetic properties due to Ni^{2+}-O-Mn^{4+} superexchange interaction. A tiny amount of Mn^{3+} in the Mn^{4+} matrix due to the local disorder causes ferromagnetic phases like $Ca_{1-x}La_xMnO_3$ [79], as mentions above.

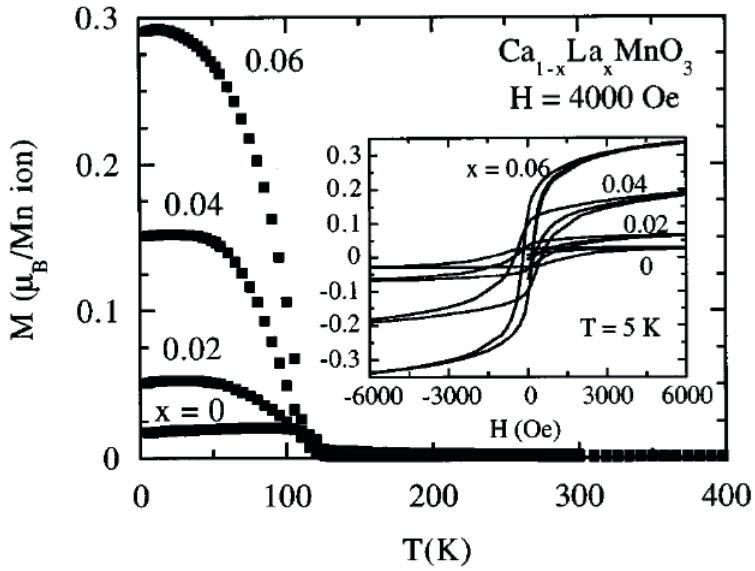

Figure 3.17: Magnetic properties of electron-doped $CaMnO_3$ ($Ca_{1-x}La_xMnO_3$) [79].

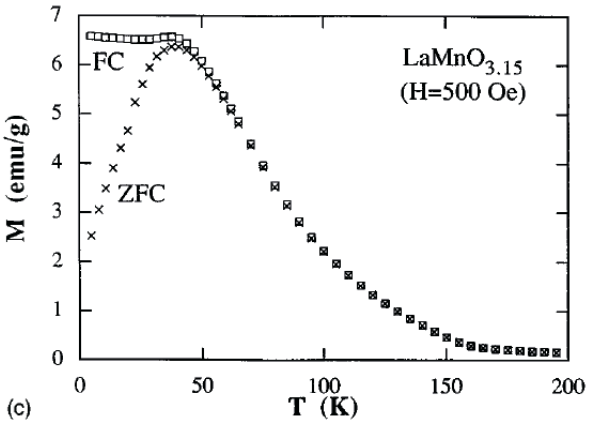

Figure 3.18: Temperature dependence of magnetization of $LaMnO_{3.15}$ [80].

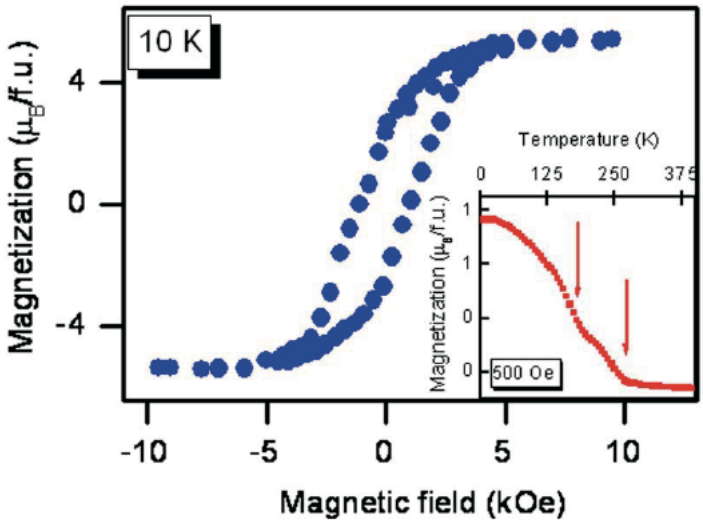

Figure 3.19: Temperature dependence of magnetization of LNMO film with absence long-range Ni/Mn ordering [71].

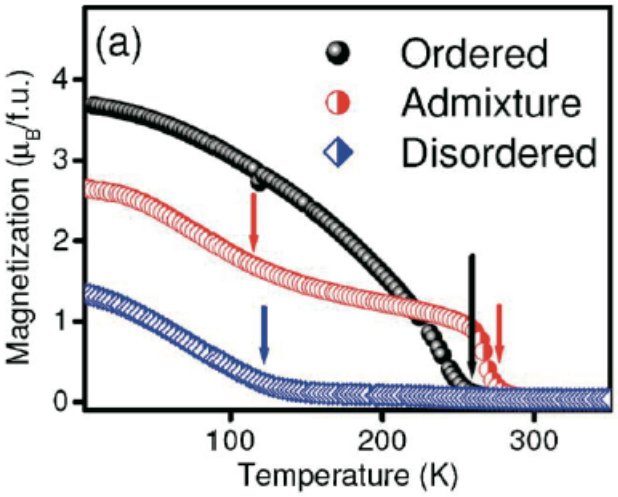

Figure 3.20: Temperature dependence of magnetization of disordered, admixture, and ordered LNMO films [82].

In the region (IV), LNMO exhibit weak ferromagnetism or no ferromagnetism. Oxygen vacancies due to low oxygen pressure during growth and structural distortions induced by the generation of oxygen vacancies could prevent the Ni-O-Mn superexchange ferromagnetic interaction. Structural distortions lead to change the bond angle and bond length having a strong influence on superexchange interaction. Guo *et al*., reported magnetic properties of LNMO films grown under the various oxygen pressures. In their work, the saturation magnetic moment degrades with decreasing the oxygen pressure, while the T_C essentially remains unchanged (270 - 290 K) [72], which is consistent with my results.

Synchrotron-radiation x-ray absorption spectroscopy (XAS) to evaluate valence states of Ni and Mn ions has been carried out at BL-2C of KEK-PF. The experimental detail are described in Chapter 4. Figure 3.21 shows Mn-L_3 and Ni-L_2 XAS spectra of samples A, C, and D. Regardless of oxygen pressure and growth temperature during thin film growth, XAS spectra reveal that Ni^{2+} and Mn^{4+} states are dominant for all samples A, C and D. A tiny amount of Ni^{3+} and Mn^{3+} states less quantifiable from our XAS spectra could be locally formed in the disordering and around oxygen vacancies of LNMO films grown under the inadequate conditions. In order to obtain LNMO films exhibiting good ferromagnetism in region (I), it is necessary to suppress the formation of Ni and Mn ions disordering and oxygen vacancies.

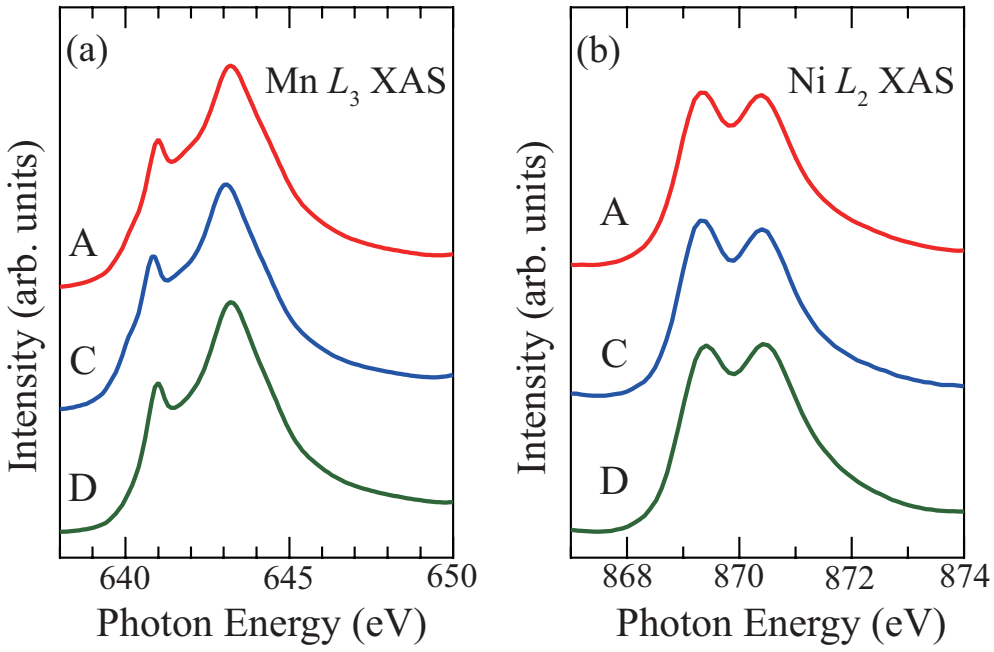

Figure 3.21: (a) Mn-L_3 XAS and (b) Ni-L_2 XAS spectra of samples A, C, and D.

In region (I), highly Ni^{2+}-O-Mn^{4+} ordering could be accomplished since LNMO shows T_C of ~ 290 K and ~ 2.2 μ_B/B-site ion magnetic moment as shown in Figs. 3.14 (a) and 3.15 (a). In fact, suggestive results of the Ni/Mn ordering have been obtained by $\theta/2\theta$ XRD scan along (*lll*) direction [77] and my SR-XRD measurements. Figure 3.22 (a) and (b) show the results of SR-XRD measurements, in which not only the (222) peak derived from fundamental reflection of LNMO but also the additional (113) peak derived from the superstructure due to the ordering are clearly observed. It can be concluded that these growth conditions could stabilize Ni^{2+}-O-Mn^{4+} superexchange ferromagnetic interaction, leading to good ferromagnetism.

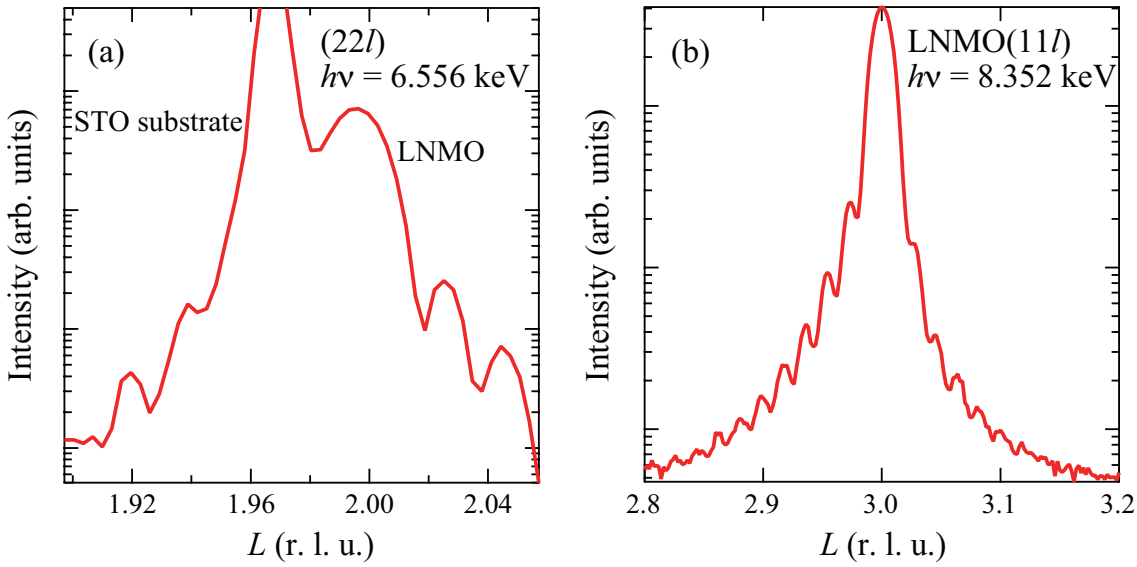

Figure 3.22: SR-XRD patterns of sample A around (a) (222) fundamental reflection and (b) (113) additional reflection derived from superstructure.

Finally I discuss the strain effect on magnetic properties of LNMO. Lattice parameter of pseudocubic bulk LNMO is 3.88 Å. The respective lattice constants of STO, $LaAlO_3$ (LAO), and $(LaAlO_3)_{0.3}$-$(SrAl_{0.5}Ta_{0.5}O_3)_{0.7}$ (LSAT) substrates are 3.905 Å, 3.870 Å, and 3.792 Å, and the strains from the substrates are +0.64 %, -0.26 %, and -2.32 % for STO, LAO, and LSAT, respectively. Guo *et al*., reported that thickness dependence of magnetic properties of LNMO film grown on an LAO substrate and concluded that the strain effects on the magnetic properties are quite small, as depicted in Fig. 3.23 [72]. Compared between LNMO films on an STO substrate and on an LSAT substrate grown under respective optimized conditions, very similar ferromagnetic properties were obtained for both substrates, indicating that strain from a

substrate has little effect on its ferromagnetic properties [83]. This may be because energy stabilization of 3*d* orbitals due to the strain does not largely change occupied spin states of Ni and Mn ions because $Ni^{2+}(3d\ t_{2g}^6 e_g^2)$ and $Mn^{4+}(3d\ t_{2g}^3 e_g^0)$ in LNMO are isotropic orbitals.

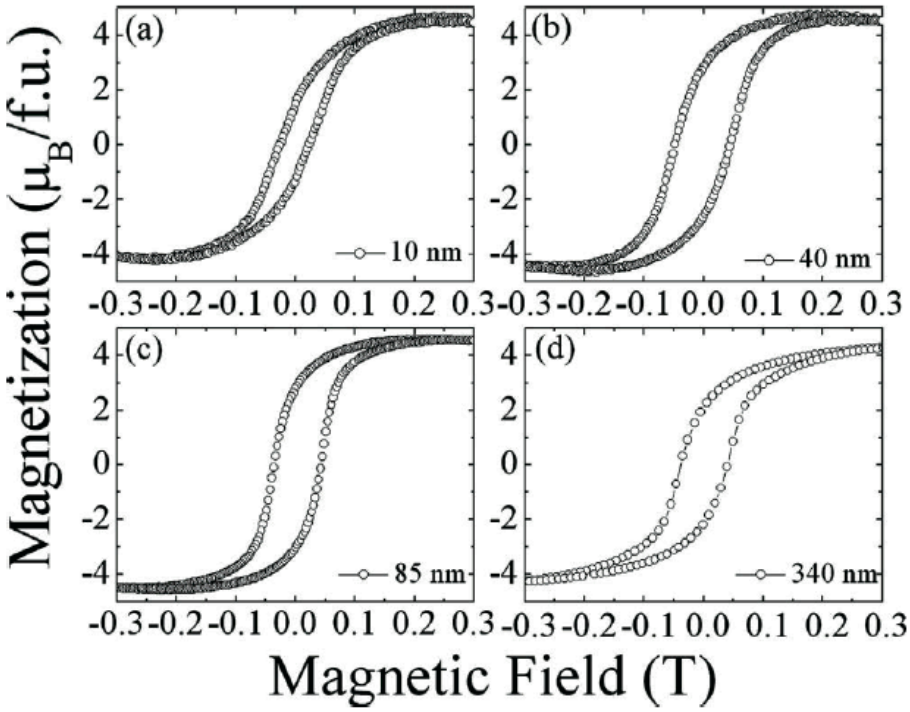

Figure 3.23: Hysteresis curves of LNMO films with the various thicknesses. The critical thickness of strain relaxation in the films is about 40-80 nm. However, Both strained and partially relaxed films show the same saturation magnetization [72].

3.4 Conclusion

In order to systematically investigate the relationship between the growth conditions of an LNMO thin film and its ferromagnetic properties, I have fabricated LNMO films under the various growth conditions and performed the characterizations of their crystal structures and ferromagnetic properties. It is found that ferromagnetisms are significantly influenced by growth temperature and oxygen pressure. Secondary phases caused by La vacancies due to too high oxygen pressure, disordering of Ni and Mn ions derived from not high enough of growth temperature, and oxygen vacancies due to low oxygen pressure could degrade ferromagnetic properties of LNMO. LNMO exhibiting ferromagnetism comparable to that of bulk LNMO can be obtained under the growth conditions where stable Ni^{2+}-O-Mn^{4+} superexchange interaction is accomplished.

Chapter 4
Electronic and magnetic states of double perovskite oxides La_2NiMnO_6

4.1 Purpose of this study

As mentioned in Chapter 3, the ferromagnetism of LNMO is considered to be Ni-O-Mn ferromagnetic superexchange interaction. In order to verify the origin of ferromagnetism of LNMO, I performed x-ray absorption spectroscopy (XAS) for evaluation of the valences of Ni and Mn ions, as well as x-ray magnetic circular dichroism (XMCD) for investigation of element-specific magnetic states.

LNMO has attracted attention because of not only its rich physics but also prospects for technological applications. Since LNMO has an advantage of its ferromagnetic transition temperature near room temperature [57, 68, 84, 69, 72], it is the one of the leading candidates amongst ferromagnetic semiconductors for spintronic device applications. However, there are only few theoretical and experimental reports on electronic structures of LNMO necessary for device applications. Fundamental properties, such as the band gap, electronic structure have not been elucidated yet. In this study, I used synchrotron-radiation photoemission spectroscopy (SR-PES) and XAS in order to study electronic structures of the valence band and conduction band for the LNMO film. The optical gap was evaluated using transmittance and reflectivity measurements.

4.2 Experiments

Epitaxial LNMO thin films exhibiting ferromagnetic properties comparable to bulk LNMO were grown on (100) $SrTiO_3$ (STO) and 0.05 wt. % Nb-doped (100) STO (Nb:STO) substrates by a pulsed laser deposition. The conductive Nb:STO substrates were necessary for preventing the charging effect in the photoemission and x-ray absorption measurements. As described in the previous chapter, LNMO thin films, which show that the ferromagnetic transition temperature of epitaxial LNMO thin films is around 280 K, with a saturated magnetization of about 2.2 μ_B/B-site ion (Sample A), were fabricated at the growth temperature of 700 °C and under an oxygen pressure of 500 mTorr.

Electronic structures of the valence band were studied using SR-PES and Mn 2*p* - 3*d* resonant PES using a Gummadata Scienta SES-100 electron energy analyzer. XAS spectra were measured by the total-electron-yield method to investigate the valences of Ni and Mn ions (Ni-$L_{2,3}$ and Mn-$L_{2,3}$ XAS) and conduction band structures (O-*K* XAS). PES, resonant PES and XAS were performed at the BL-2C of KEK-PF. Transmittance and reflectivity measurements in the energy range of 0.35 ~ 2.5 eV were carried out to evaluate the optical gap using a Fourier-transform interferometer (Bruker, IFS120HR/X) at BL43IR of SPring-8. A tungsten ramp source and an InSb detector were used for the energy region of 0.35 ~ 1.5 eV and a tungsten ramp source and Si photo detector were used for the energy region of 1.0 ~ 2.5 eV. As a reference of reflectivity, a gold or silver film deposited on the sample surface was utilized. PES, XAS, transmittance, and reflectivity spectra were taken at room temperature.

XMCD measurements were performed at BL-16A of KEK-PF. The magnetic field of about 1 T was applied 30 ° from the sample surface and parallel to the incident beam. The helicity of the incident beam was fixed, while the direction of the magnetic field was reversed to measure XMCD. The XMCD spectra were taken in a total-electron-yield mode at 30 K.

4.3 Results and Discussion

4.3.1 Study of valence of B-site ions

Figures 4.1 (a) and (b) depict the Ni-$L_{2,3}$ and Mn-$L_{2,3}$ XAS spectra measured in order to evaluate the respective valence states of Ni and Mn ions. Ni-$L_{2,3}$ (Mn-$L_{2,3}$) XAS spectra is derived from the transition from Ni (Mn) 2*p* to 3*d* following the absorption of x-ray and are composed of two peak reflecting the split of Ni (Mn) 2*p* states due to the spin-orbital coupling. Background of XAS spectra at the both Mn-$L_{2,3}$ and Ni-$L_{2,3}$ edge were assumed to be hyperbolic tangent functions. In Fig. 4.1 (a), the peak around 852-858 eV is derived from the transition of Ni $2p_{3/2} \rightarrow 3d$, called Ni-L_3 XAS, and that around 868-874 eV is from the transition of Ni $2p_{1/2} \rightarrow 3d$, called Ni-L_2 XAS. As the Ni-L_3 XAS partially overlaps the very strong La-M_4 absorption edge due to the close proximity of the two energy levels, Ni-L_2 XAS was focused on in order to assess the valence state of Ni in the LNMO film. Figure 4.2 show the references of Ni-$L_{2,3}$ XAS for Ni^{3+} and Ni^{2+} states in $Ni^{2+}O$, $PrNi^{3+}O_3$, and $NdNi^{3+}O_3$ [85]. The single peak structure in the Ni-L_2 XAS is reported for Ni^{3+}, while Ni^{2+} state shows two-peak structure appearing at the lower photon energy. The same trends are also reported for $Bi_{1-x}La_xNiO_3$ [86]. Compared the Ni-L_2 absorption peak of LNMO with reported ones of Ni^{3+} and Ni^{2+} [85, 86], the doublet-peak shape similarity of the XAS peaks in Ni-L_2 XAS of LNMO and in Ni^{2+} implies that the Ni^{2+} state is dominant in the LNMO film. This demonstrates that the valence of Ni changes from 3+ in the bulk phase to 2+ in LNMO. As for the valence of Mn ions, the peak around 640-650 eV is derived from the transition of Mn $2p_{3/2} \rightarrow 3d$, called Mn-L_3 XAS, and that around 651-658 eV is from the transition of Mn $2p_{1/2} \rightarrow 3d$, called Mn-L_2 XAS, shown in Fig. 4.1 (b). As a reference, Fig. 4.3 shows the Mn-$L_{2,3}$ XAS for $La_{1-x}Sr_xMnO_3$[87]. The spectral shapes clearly change following the valence change from Mn^{3+} to Mn^{4+} with increasing x. Especially, the shapes of Mn-L_3 XAS is greatly differenet between Mn^{3+} and Mn^{4+}. The Mn-L_3 XAS peak is broader for

Mn^{3+} than that for Mn^{4+} and the energy of the peak top shifted to the higher photon energy with the valence change form Mn^{3+} to Mn^{4+}. The same trend also reported for $LaMn^{3+}O_3$ and $Mn^{4+}O_2$ by Mitra *et al*. (Fig. 4.4) [88]. By comparing the Mn-L_3 absorption peak of LNMO with reported ones of Mn^{3+} and Mn^{4+}, the sharp shoulder structure and doublet-peak shape of LNMO and in Mn^{4+} implies that the Mn^{4+} state is dominant in the LNMO thin film, indicating that the Mn valence changes from 3+ in the bulk phase to 4+ in LNMO. Based on these results, it is concluded that the charge transfer of $Ni^{3+} + Mn^{3+} \rightarrow Ni^{2+} + Mn^{4+}$ occurs in LNMO, which is consistent with the result expected from the redox potential as mentioned in Chapter 1 [28].

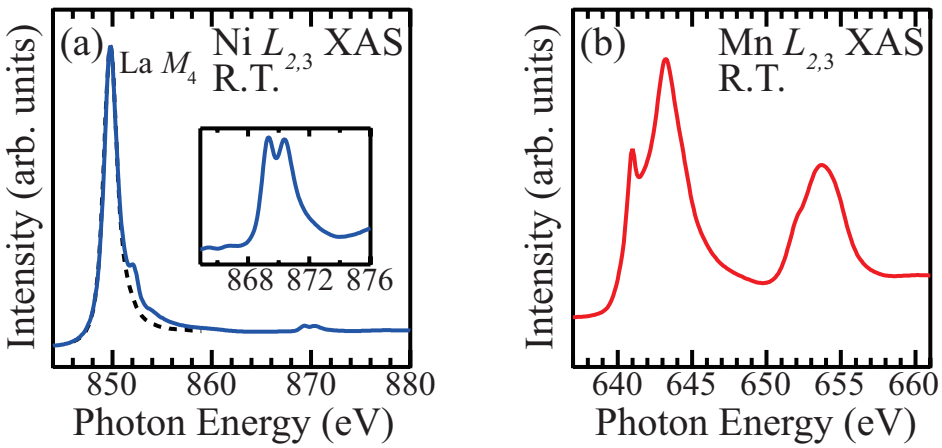

Figure 4.1: (a) Ni-$L_{2,3}$ XAS spectrum of an LNMO epitaxial thin film. The inset is the expanded spectrum around L_2 edge. Ni-L_3 XAS partially overlaps the La-M_4 absorption edge (dashed line). (b) Mn-$L_{2,3}$ XAS spectrum of an LNMO epitaxial thin film.

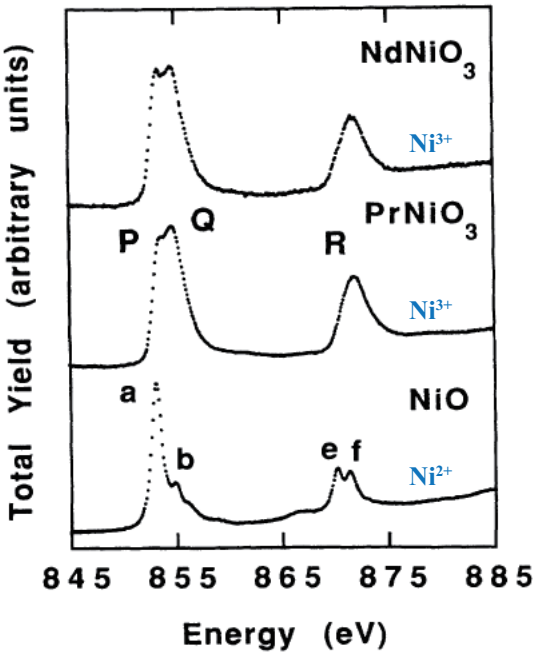

Figure 4.2: Ni-$L_{2,3}$ XAS spectra of $NdNi^{3+}O_3$, $PrNi^{3+}O_3$ and $Ni^{2+}O$ [85].

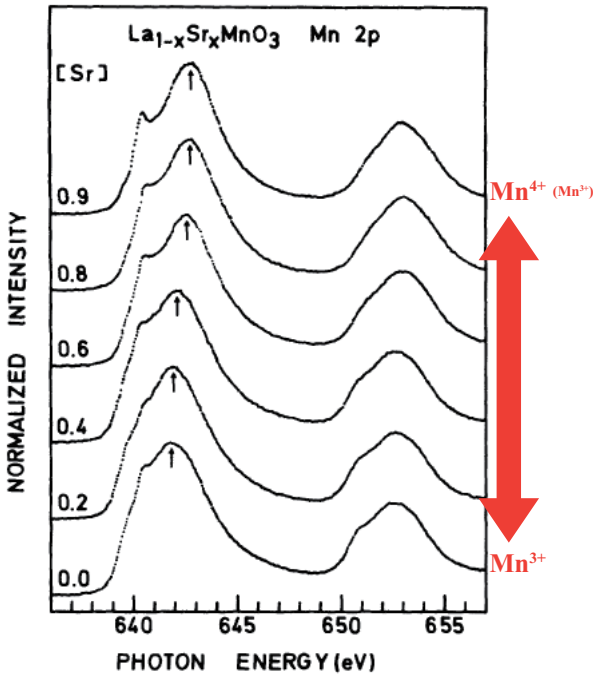

Figure 4.3: Mn-$L_{2,3}$ XAS spectra of $La_{1-x}Sr_xMnO_3$ [87].

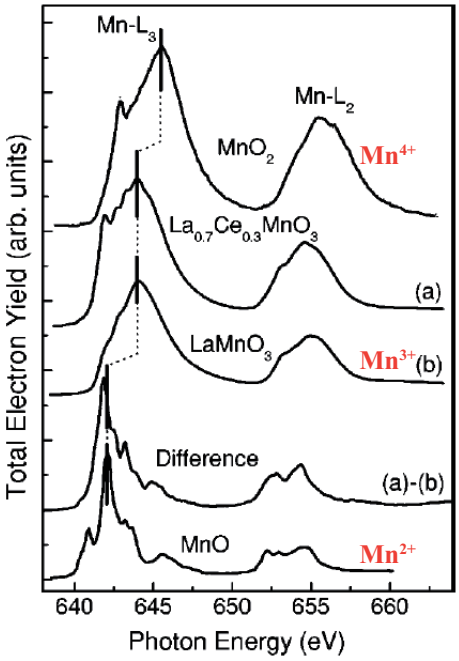

Figure 4.4: Mn-$L_{2,3}$ XAS spectra of $Mn^{4+}O_2$, $LaMn^{3+}O_3$ and $Mn^{2+}O$ [88].

4.3.2 X-ray magnetic circular dichroism study of magnetic states

In order to evaluate the element-specific magnetic states of Ni and Mn ions in LNMO, XMCD measurements were carried out. Figures 4.5 (a) and (b) shows Ni-$L_{2,3}$ and Mn-$L_{2,3}$ XAS spectra measured under the positive and negative magnetic bias of 1 T and temperature of 30 K. The Ni-$L_{2,3}$ XAS spectra have been extracted by subtracting the XAS spectrum of an LMO film representative of the La-M_4 edge from the corresponding raw XAS spectra of LNMO. The Ni-$L_{2,3}$ and Mn-$L_{2,3}$ XMCD spectra were obtained by the subtraction of a positive bias XAS and a negative bias XAS spectra, as depicted in Fig. 4.5 (c) and (d). Mn-$L_{2,3}$

XAS and XMCD spectra were normalized by the area intensity of Mn-$L_{2,3}$ XAS, while Ni-$L_{2,3}$ XAS and XMCD spectra were normalized by area intensity of Ni-L_2 XAS because Ni-L_3 XAS partially overlaps the very strong La-M_4 absorption edge as mentioned above. XMCD signals are clearly observed at both Ni and Mn absorption edges, indicating both Ni and Mn ion are magnetized in LNMO. The strong negative signs in the L_3 edge of both Ni and Mn XMCD spectra demonstrate that Ni 3*d* and Mn 3*d* spins align parallel to the magnetic field. Observed XMCD spectra are quite similar to those reported for LNMO [89, 90], as shown in Fig. 4.6 [89], and Mn^{4+} XMCD spectra reported by Burnus *et al*. [91]. The same sign of XMCD signals between Ni and Mn is an evidence of the Ni spins and Mn spins couple ferromagnetically. The effective spin moments of Ni and Mn were calculated by using XMCD sum rules to be 1.6 μ_B for Ni and 2.8 μ_B for Mn, respectively. These values are close to the spin only moments expected by spin structures of $Ni^{2+}(t_{2g}^6 e_g^2)$ and $Mn^{4+}(t_{2g}^6 e_g^2)$ and average spin moment of 2.2 μ_B/B-site ion is almost the same with saturated magnetic moment evaluated by SQUID measurements. Considering that XAS measurements demonstrate that Ni^{2+} and Mn^{4+} are dominant in LNMO, the origin of ferromagnetism in LNMO is confirmed to be Ni^{2+}-O-Mn^{4+} ferromagnetic superexchange interaction obeying Kanamori-Goodenough rule. These results indicate that charge transfer between Ni and Mn ions plays a crucial role for emergent of ferromagnetism in LNMO.

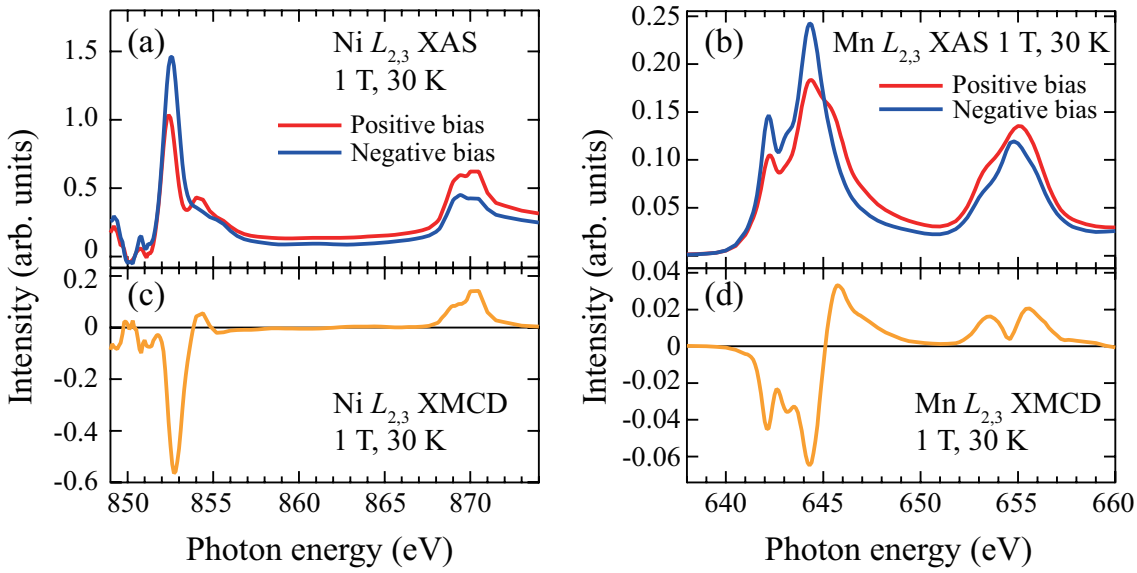

Figure 4.5: (a) Ni-$L_{2,3}$ and (b) Mn-$L_{2,3}$ XAS spectra of an LNMO epitaxial thin film obtained under the positive and negative magnetic bias of 1 T and temperature of 30 K. (c) Ni-$L_{2,3}$ and (d) Mn-$L_{2,3}$ XMCD spectra of an LNMO epitaxial thin film.

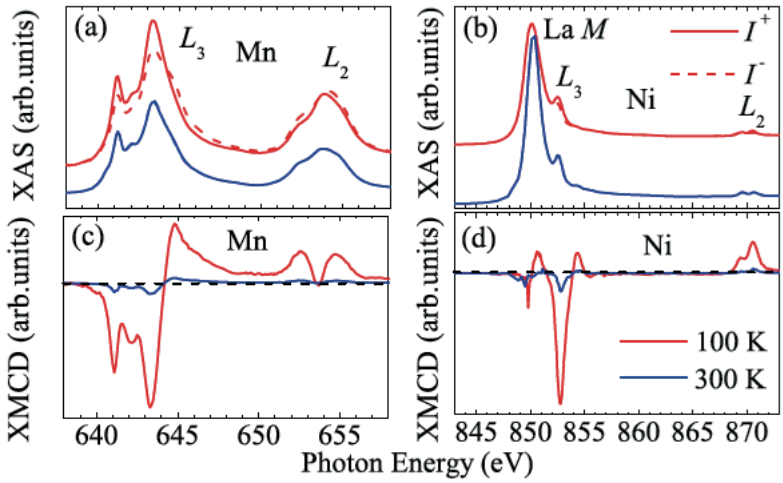

Figure 4.6: (a) Mn-$L_{2,3}$ and (b) Ni-$L_{2,3}$ XAS spectra of an LNMO epitaxial thin film obtained by the different polarization of x-rays. Solid curves are XAS spectra I^+ and dashed curves are XAS spectra I^-. (c) Mn-$L_{2,3}$ and (d) Ni-$L_{2,3}$ XMCD spectra $\Delta I = I^+ - I^-$ of an LNMO epitaxial thin film [89].

4.3.3 Photoemission study of valence band states

In order to clarify the components of the valence band, the valence band PES and Mn 2*p* - 3*d* resonant PES measurements were performed. Figure 4.7 shows Mn 2*p* - 3*d* on- and off-resonance PES spectra as well as the valence band PES spectrum of the LNMO thin film. The on- and off-resonance PES spectra were taken at respective photon energies of 642.6 eV and 634.6 eV, determined from the Mn-$L_{2,3}$ XAS spectrum. Beacuse the photoionization cross-section of Mn 3*d* states is strongly enhanced (suppressed) in the Mn 2*p* - 3*d* on- (off-) resonant PES measurements, the Mn 3*d* derived states are selectively obtained in the differential between on- and off-spectra. Since no spectral weight is observed at the Fermi level, the LNMO thin film can be regarded as a semiconductor. The valence band of LNMO is inferred to consist of a combination of O 2*p*, Ni 3*d*, Mn 3*d* states in addition to their hybridizations. Beacuse features A, B and C depicted in Fig. 4.7 are resonantly enhanced in the on-resonance PES spectrum, they are related to Mn 3*d* states, with feature A attributed mainly to the Mn 3*d* e_g state. Although the Mn-$L_{2,3}$ XAS spectrum indicates that the Mn^{4+} state is dominant in the LNMO film, a small but non negligible amount of the Mn^{3+} state could also exist in the LNMO thin film. Small spectral weight derived from the Mn 3*d* e_g state observed in feature A is due to this residual Mn^{3+} ($3d\ e_g^1 t_{2g}^3$) state. Feature B is due to the Mn 3*d* t_{2g} state, while feature C originates from a strongly mixed combination of O 2*p* and Mn 3*d* states [92]. We note that the three peaks present in the valence band PES spectrum (α, β and γ) are not observed in the on-resonance PES spectrum. However, since these features are also seen in the off-resonance PES spectrum where Mn 3*d* states are resonantly suppressed, we infer that peak α may originate from the contribution of the Ni 3*d* state, while β and γ are due to the O 2*p* dominant states [93, 94]. The expanded spectra near the Fermi level are shown in the inset of Fig. 4.7. Spectral weight is clearly observed in the on-resonance PES spectrum near the Fermi level, while it is mostly suppressed in the off-resonance PES spectrum. This indicates that the electronic state located at

the valence band maximum (VBM) for LNMO might be the state derived from Mn 3*d*.

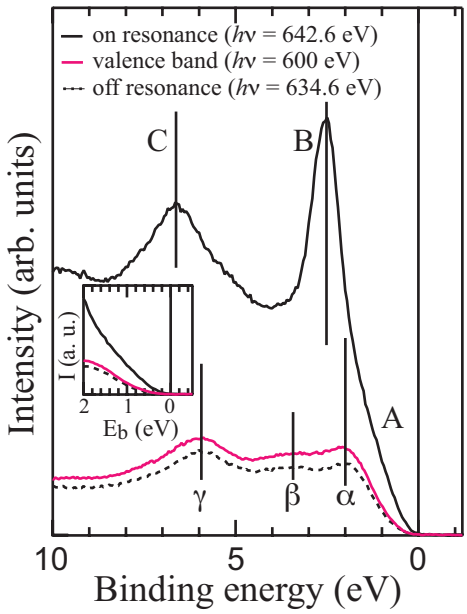

Figure 4.7: Valence band and Mn 2*p* - 3*d* on- and off-resonance PES spectra for an epitaxial LNMO thin film. On-resonance (black solid), off-resonance (dash) and valence band (pink) PES spectra were measured at respective photon energies of 642.6, 634.6 and 600 eV. An expanded image of the spectra near the Fermi level is shown in the inset.

4.3.4 Study of band gap

In order to evaluate the optical gap of LNMO, the transmittance and reflectivity measurements were carried out. The transmittance and reflectivity spectra are shown in Fig. 4.8 (a). The transmittance is multiplied by 1-$Rs(\omega)$ (Rs: reflectivity of the substrate). The refractive index $n(\omega)$ and the extinction coefficient $\kappa(\omega)$ were numerically derived using the

Newton-Raphson method [30], shown in Fig. 4.8 (b). The thickness of an LNMO film for calculations of the optical conductivity was evaluated by a surface roughness profiler (Veeco, Dektak6M) to be about 1000 Å. Figure 4.9 shows the optical conductivity $\sigma(\omega)$ obtained by the following equation.

$$\sigma(\omega) = \omega n(\omega)\kappa(\omega)/2\pi \qquad (4.1)$$

Energy of the optical gap can be observed as a gradual onset of the spectral intensity rather than a peak structure as reported for $LaMO_3$ (M: 3*d* transition metal), shown in Fig. 4.10[95Fig1] [95]. Therefore, the optical gap of LNMO was determined through linear interpolation of a sharp rise of the spectral intensity (dashed line in Fig. 4.9). The optical conductivity spectrum allows us to conclude that LNMO is a semiconductor with an optical gap of about 1.5 eV.

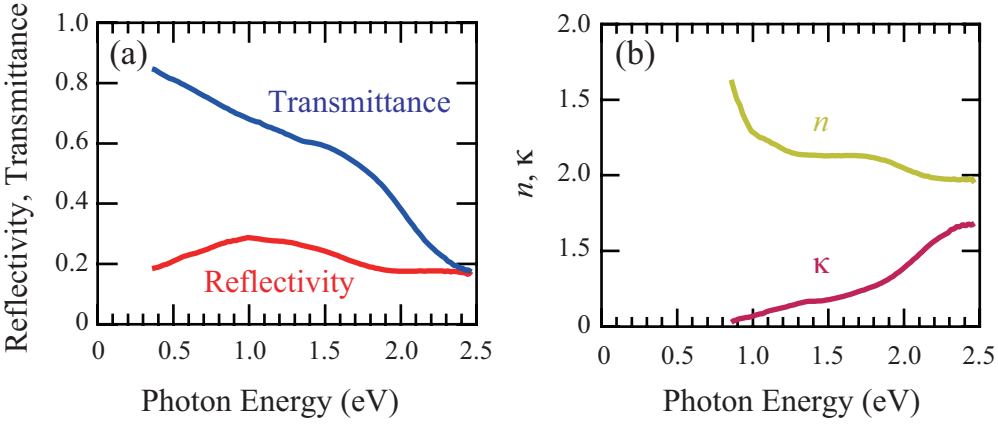

Figure 4.8: (a) Transmittance and reflectivity spectra and (b) refractive index $n(\omega)$ and the extinction coefficient $\kappa(\omega)$ spectra of an LNMO epitaxial thin film.

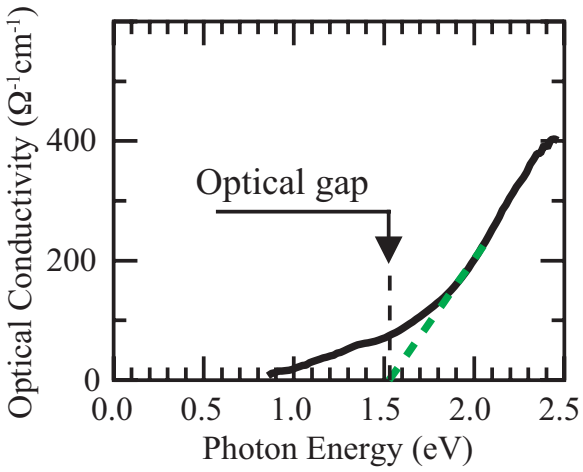

Figure 4.9: Optical conductivity spectrum of an LNMO epitaxial thin film. The optical gap was determined by linear interpolation of the green dashed line.

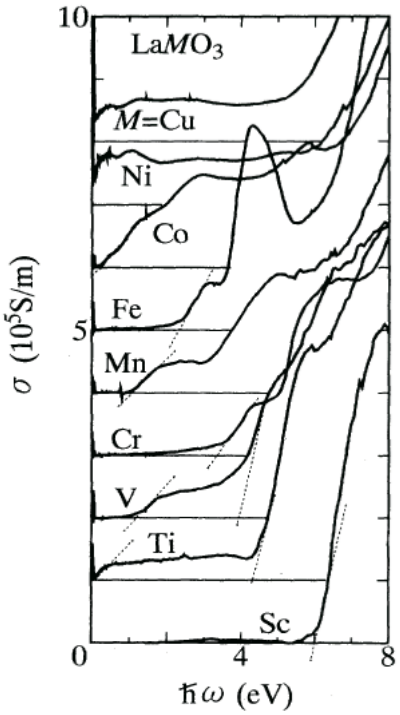

Figure 4.10: Optical conductivity spectra of $LaMO_3$ (M = Sc - Cu). The optical gap was determined by linear interpolation of the dashed line [95].

4.3.5 X-ray absorption study of conduction band states

The conduction band structure is investigated using the O-*K* XAS spectra, as depicted in Fig. 4.11. O-*K* XAS spectra, absorption spectra due to O 1*s* → 2*p* transition, reflect the unoccupied states of metal ions strongly hybridized with oxygen because O 2*p* states and metal states hybridize resulting in an unoccupied band beyond the Fermi level. Therefore, states of the conduction can be obtained by studying O-*K* XAS spectra. The broad peak II centered at 536 eV can be mainly associated to the La 5*d*-O 2*p* state and the two peaks III around 538-549 eV to be derived from hybridized states of Ni 4*sp*, Mn 4*sp* and O 2*p*. This interpretation is consistent with O-*K* XAS spectra of $LaNiO_3$ and $LaMnO_3$ [96, 97]. Figure 4.12 shows changes of O-*K* XAS spectra of $LaNiO_{3-\delta}$ with the valence change between Ni^{3+} and Ni^{2+} reported by Abbate *et al*. [96]. The peak around 528.5 eV corresponds to the Ni^{3+}-O 2*p* state in $LaNiO_3$ and this peak shifts to a higher photon energy and is hidden by the stronger peak derived from La 5*d* for Ni^{2+}-O 2*p* in $LaNiO_{2.5}$. Kuiper *et al.* also reported the same trends for $La_{2-x}Sr_xNiO_{4+\delta}$ [98]. On the other hand, as for the Mn 3*d*-O 2*p* states, the position of the absorption edge is almost the same between Mn^{3+} and Mn^{4+} shown in Fig. 4.13 [87, 97]. Because the valence states of B-site ions in an LNMO film are Ni^{2+} and Mn^{4+} as mentioned before, the Ni^{2+} 3*d*-O 2*p* state in the XAS spectrum can occur at a higher photon energy than the absorption edge, which is hidden by the stronger La 5*d*-O 2*p* state (structure II) and peak I corresponds to the Mn^{4+} 3*d*-O 2*p* state. These results suggest that the conduction band minimum (CBM) might be derived mostly from the Mn 3*d* state.

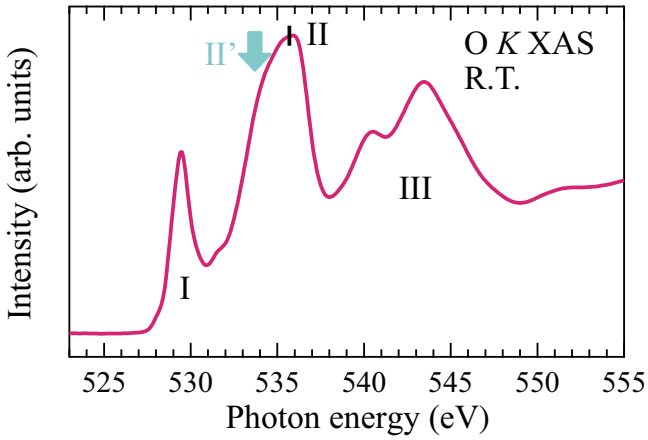

Figure 4.11: O-*K* XAS spectrum of an LNMO epitaxial thin film.

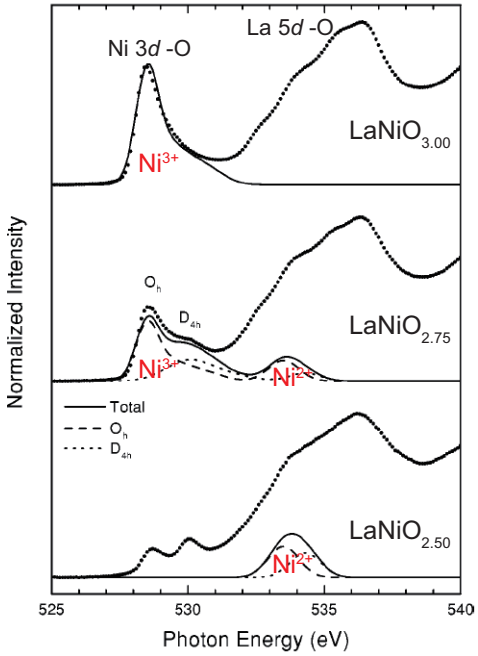

Figure 4.12: O-*K* XAS spectrum of $LaNiO_{3-\delta}$ (dots) compared to the cluster-model-calculation (solid lines) [96]

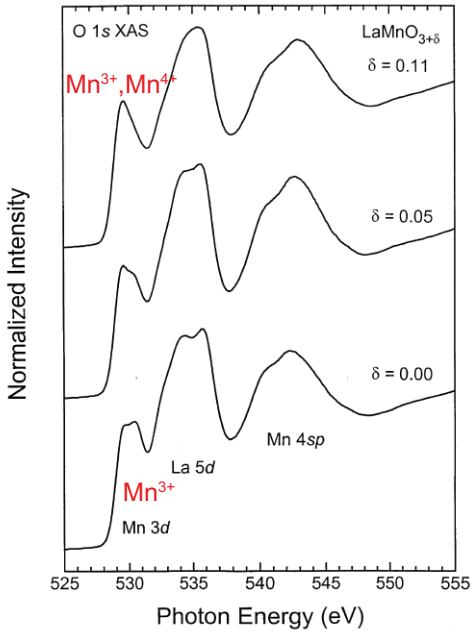

Figure 4.13: O-*K* XAS spectrum of $LaMnO_{3+\delta}$ [97].

4.3.6 Electronic structure of valence band and conduction band

Based on the aforementioned results, we constructed the energy band diagram of the valence band and the conduction band for LNMO. Figure 4.14 shows combined spectra of the valence band and the conduction band as measured by the valence band PES and O-*K* XAS. The optical gap (~ 1.5 eV) extrapolated from optical conductivity measurements was used to normalize the PES and XAS spectra. Valence band maximum is located 0.3 eV below the Fermi level evaluated by the intersection point between the extrapolation of the linear portion of the leading edge and the background level in valence band spectra. Therefore, LNMO could be regarded as a *p*-type semiconductor according the energy of the Fermi level in the band gap of about 1.5 eV. It was confirmed that LNMO films show a *p*-type conduction by Seebeck

measurements [99]. Figure 4.15 are also the schematic image of the partial density of states for the valence band and conduction band for LNMO obtained resonance valence band spectra and O-*K* XAS spectra. Valence band is composed of Ni 3*d*, Mn 3*d*, O 2*p* states, and their hybridization. As mentioned before the VBM is derived from Mn 3*d* e_g states due to the small amount of residual Mn^{3+}. As for the conduction band, it consists of the hybridization of O 2*p* state and Mn 3*d*, Ni 3*d*, La 5*d*, and Ni 4*sp*, and Mn 4*sp* state. The CBM is also composed of Mn 3*d* state.

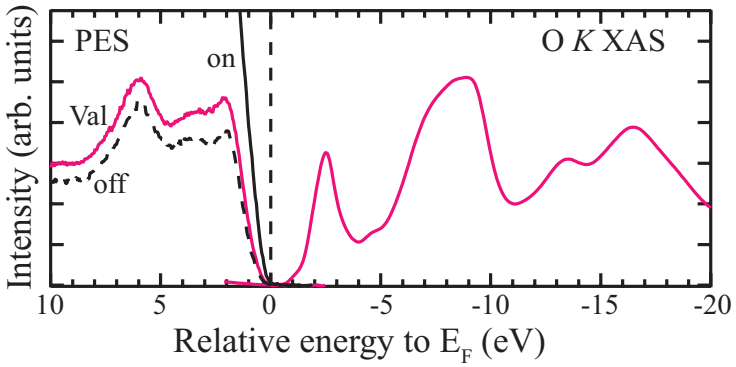

Figure 4.14: Electronic structure of valence band and conduction band of a LNMO epitaxial thin film derived from valence band PES and O-*K* XAS. The energy of the XAS spectrum was determined on the basis of the optical gap (~ 1.5 eV). Mn 2*p* - 3*d* on- and off-resonance spectra are also shown.

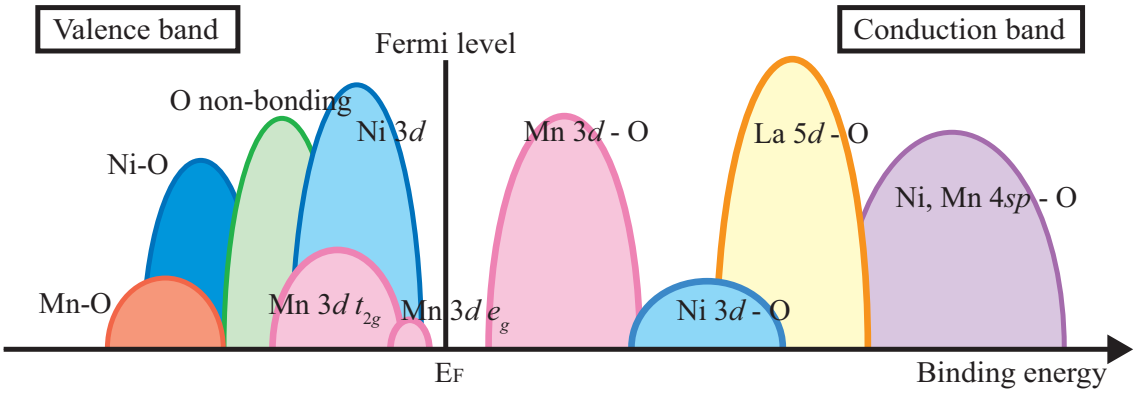

Figure 4.15: A schematic image of the electronic structure of valence band and conduction band of a LNMO epitaxial thin film obtained valence band PES and O-*K* XAS.

Figures 4.16 and 4.17 shows the results of first-principles density functional calculations reported Das *et al*. and Mater *et al*. [100, 101]. Both reports demonstrate that the ferromagnetic insulating state is the most stable in LNMO, which is consistent with experimental results. In these calculations, Ni 3*d* e_g, Ni 3*d* t_{2g}, Ni 3*d* t_{2g}, and O 2*p* states are observed in the valence band, while Ni 3*d* e_g, Mn 3*d* e_g, and Mn 3*d* t_{2g} states are located in the conduction band, indicating that nominal valences of Ni an Mn ions are Ni^{2+} ($3d\ t_{2g}^6 e_g^2$) and Mn^{4+} ($3d\ t_{2g}^3 e_g^0$), respectively. It is noted that Das *et al*. and Mater *et al*. reported the VBM for LNMO consists of the Ni 3*d* state based on the calculation, while the Mn 3*d* state was observed at the VBM from the resonant and the valence band PES. The disagreement can be attributed to the existence of a small amount of the Mn^{3+} ($3d\ t_{2g}^3 e_g^1$) state believed to be caused by the local Ni/Mn disordering as well as by oxygen vacancies in epitaxial LNMO thin films. Indeed, the Mn^{3+} ion has a 3*d* e_g electron, as opposed to the Mn^{4+} ion which has no e_g electron. Thus, if all Mn ions in the LNMO film are in the 4+ state, no Mn 3*d* e_g state at the VBM will be observed.

Instead, the Ni 3*d* state will appear at the VBM, which will be agreement with the reported calculations. As for the conduction band, the CBM of the LNMO is due to the Ni^{2+} 3*d* state, as per the first-principle density functional calculation. However, the O-*K* XAS spectrum indicates that the Ni^{2+} 3*d* state is located at higher photon energy than the absorption edge. Moreover, the CBM of the LNMO film is inferred from the Mn^{4+} 3*d*-O 2*p* state, which is inconsistent with the results obtained using the first-principle density functional calculation. Clearly, further investigation on the electronic band structure of LNMO from the both experimental and theoretical scope is needed.

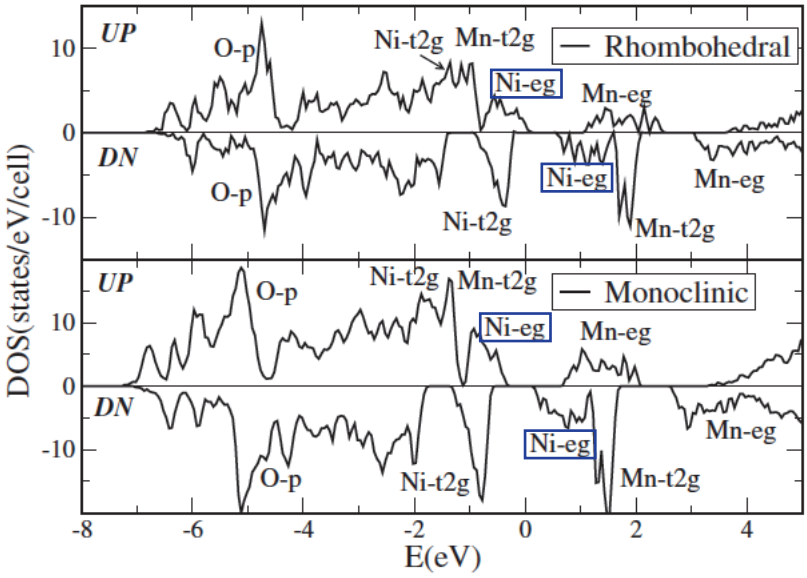

Figure 4.16: Density of state of LNMO in geometry optimized rhombohedral and monoclinic phases calculated by GGA [100].

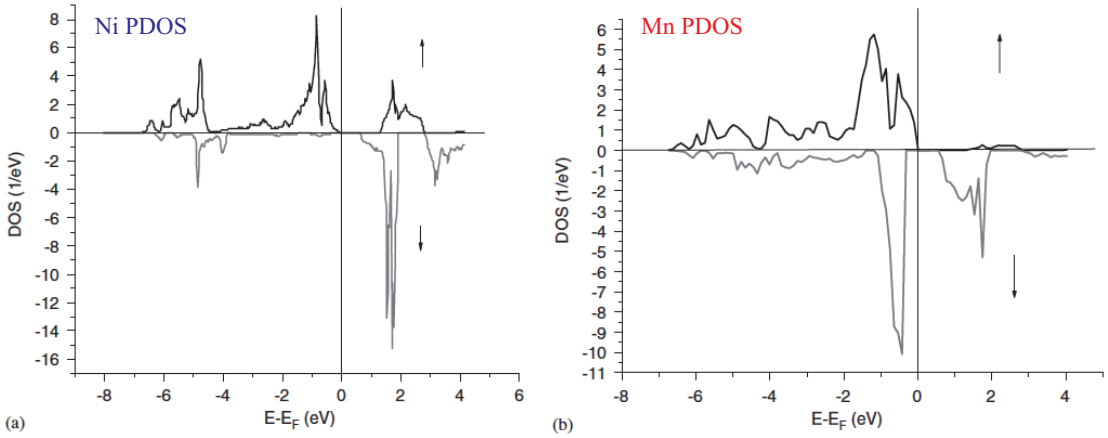

Figure 4.17: Site and spin-projected density of state of Mn and Ni in LNMO calculated by GGA or LSDA [101].

4.4 Conclusion

In order to study the charge transfer phenomena between Ni and Mn ions and verify the origin of the ferromagnetism in LNMO, I have investigated the valence states of Ni and Mn ions and their magnetic coupling by XAS and XMCD. Based on the Ni-$L_{2,3}$ and Mn-$L_{2,3}$ XAS measurements, Ni^{2+} and Mn^{4+} states are dominant in epitaxial LNMO thin film. Ni-$L_{2,3}$ and Mn-$L_{2,3}$ XMCD measurements indicate that spins in Ni^{2+} and Mn^{4+} ions are coupled ferromagnetically. Therefore, it is concluded that a Ni^{2+}–O–Mn^{4+} ferromagnetic superexchange interaction is the origin of ferromagnetism in LNMO. The charge transfer between Ni and Mn ions play an important role for the ferromagnetism in LNMO. The electronic structures of the valence band and the conduction band in LNMO films were evaluated using SR-PES, XAS as well as optical spectroscopy. The Mn 2*p* – 3*d* resonant and valence band PES spectra allow us to infer that the electronic state located at the VBM for LNMO mainly consists of the Mn 3*d* state, while O-*K* XAS measurements reveal that the CBM is composed mostly of the Mn 3*d*-O

2*p* hybridized state. The optical gap is estimated to be about 1.5 eV based on the optical conductivity derived from optical spectra.

Chapter 5
Charge transfer across the heterointerface between perovskite oxides $LaNiO_3$ and $LaMnO_3$

5.1 Introduction

5.1.1 Previous studies of charge transfer and interfacial magnetism in $LaNiO_3$-$LaMnO_3$ heterostructures

In stoichiometric bulk form, $LaMnO_3$ (LMO) is an A-type antiferromagnetic insulator with Neel temperature of about 140 K. At low temperature, spins align ferromagnetically in-plane, while antiferromangetically inter-plane. On the contrary, LMO thin film often shows ferromagnetism due to oxygen excess and/or cation vacancy or strain effects from a substrate. $LaNiO_3$ (LNO) is a prototype of a paramagnetic metal. Recently, the heterointerface between LNO and LMO has been particularly studied as a typical example of interfacial magnetism. Gibert and coworkers have reported the appearance of novel interfacial magnetic interaction in LNO-LMO superlattices depending on the orientations [27]: An unusual spin order occurs in the paramagnetic LNO layer in the interface region which is in contact with the "ferromagnetic" LMO layer, resulting in the appearance of a certain exchange bias between the two oxides. Interestingly, this exchange bias was observed only for (111) superlattices, but was absence for (001)-orientation, as shown in Fig. 5.1. Very recently, x-ray magnetic circular dichroim (XMCD) measurements have confirmed that magnetic moment reside in an LNO

which should be paramagnetic in the bulk phase and the induced net spins of Ni and Mn ions in (111)-oriented LNO-LMO superlattices couple ferromagnetically [102].

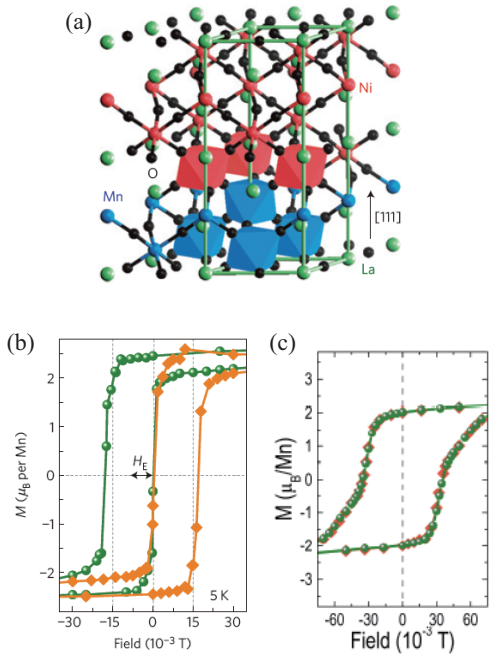

Figure 5.1: (a) Schematic images of the atomic planes near an interface of (111)-oriented LNO-LMO superlattice. Hysteresis curves of (a) (111)-oriented $[(LNO)_7/(LMO)_7]_{15}$ superlattice and (b) (001)-oriented $[(LNO)_7/(LMO)_7]_8$ superlattice [27].

As for (001)-oriented LNO-LMO supperlattices, a recent study has also demonstrated the occurrence of ferromagnetism in the interface region, as shown in Fig. 5.2 [25, 102]. Let me compare the LNO-LMO heterostructures to double-perovskite La_2NiMnO_6 (LNMO). The double-perovskite LNMO exhibits ferromagnetic behavior, in which LNO and LMO layers alternately stack along the [111] direction resulting in the rock-salt-type ordering of Ni and Mn ions. That is, LNMO can be regarded as a (111)-oriented $(LNO)_1$-$(LMO)_1$ "natural" superlattice. As mentioned in Chapter 2 and 3, first, as a result of charge transfer between the Ni and Mn

ions, the formal valence change $Ni^{3+} + Mn^{3+} \rightarrow Ni^{2+} + Mn^{4+}$ takes place. Then, the rock-salt type ordering of the Ni and Mn ions induces ferromagnetism owing to the ferromagnetic superexchange interaction expected by the Kanamori-Goodenough rule in all directions along the nearest neighboring ions [57, 68]. On the other hand, in the case of (001)-oriented superlatteces, the stabilization of interfacial ferromagnetism derived from superexchange interaction obeying Kanamori-Goodenough rule is geometrically not expected: Inter-plane spins (Ni-O-Mn bonds) are coupled ferromagntically as an analogy of LNMO, while antiferromagnetic coupling are expected in in-plane Ni-O-Ni and Mn-O-Mn bonds. Thus, the ferromagnetism observed (001)-oriented superlattices cannot be explained only by ferromagnetic superexchange interaction like that in LNMO.

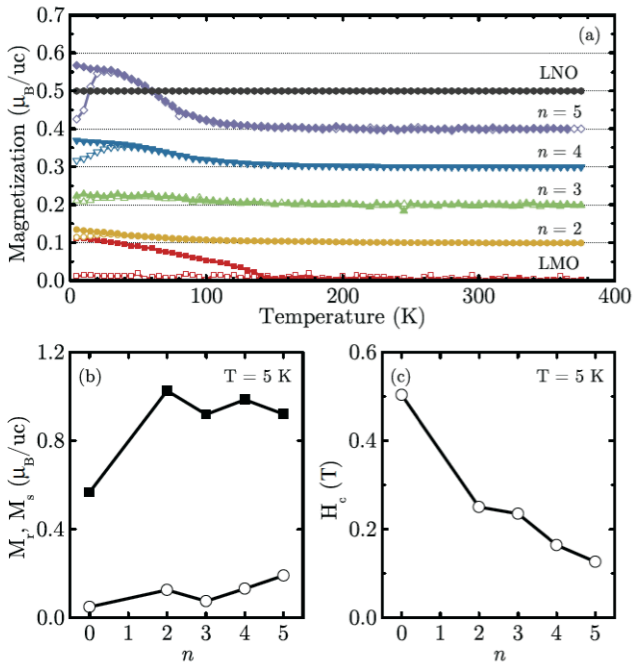

Figure 5.2: (a) Temperature dependence of magnetization and (b) Remanent magnetization (open symbols) and saturation magnetization (filled symbols), and (c) Coercive field as a function of LNO thickness for (001)-oriented $[(LNO)_n/(LMO)_2]_m$ superlattice [25].

5.1.2 Purpose of this study

The novel physical properties that emerge at such heterointerfaces may significantly depend on the charge redistribution near the heterointerfaces, in particular the resultant spatial distribution across the interface. For LNO/LMO superlattices, it has been previously demonstrated by spectroscopic measurements that the charge transfer between the Ni and Mn ions ($Ni^{3+} + Mn^{3+} \rightarrow Ni^{2+} + Mn^{4+}$, as in the case of La_2NiMnO_6) occurs across the interface, but no spatially (depth) resolved measurements were provided in these works [25, 102]. Thus, to understand and control the exotic magnetic properties emerging at the heterointerface, it is necessary to elucidate not only the valence change due to the charge transfer but also the spatial distribution of the transferred charge across the interface of LNO/LMO.

I have investigated the interfacial electronic structure of LNO/LMO heterostructures using *in situ* x-ray absorption spectroscopy (XAS). In particular, by utilizing the elemental selectivity of XAS, I have determined the changes in the formal valences of the Ni and Mn ions at the interface caused by the charge transfer. Furthermore, the spatial distributions of transferred charges in the LNO and the LMO layers were investigated by systematic thickness-dependent XAS measurements. It has been found that the spatial distribution is different between two layers. I discussed a possible origin of this difference in the spatial distribution of the transferred charges in terms of the charge spreading model, which treats the transfer integral between neighboring transition metal ions and the Coulomb interaction [103].

5.2 Experiments

Digitally controlled LNO/LMO and LMO/LNO bilayer structures were fabricated onto 0.1 at. % Nb-doped $SrTiO_3$ (STO) (001) substrates in a laser molecular-beam epitaxy chamber

connected to a photoelectron spectroscopic system at beamline BL-2A MUSASHI of KEK-PF. A Nd-doped yttrium-aluminum-garnet laser in the frequency-triplet mode (λ = 355 nm) at a repetition rate of 1 Hz was used for ablation. A sintered LNO and LMO pellets were used as the targets. The TiO_2-terminated Nb:STO substrates were annealed at 1050 °C under an oxygen pressure of 1×10^{-7} Torr to obtain atomically flat and chemically clean surfaces. During LNO and LMO deposition, the substrate was kept at temperatures of 450–500°C and 600–700°C, respectively, and the oxygen pressure was maintained at 1×10^{-3} Torr. The thicknesses of the LNO and the LMO films were precisely controlled by monitoring the intensity oscillation of the specular spot with reflection high-energy electron diffraction (RHEED) during the growth. For the LNO/LMO (LMO/LNO) bilayers, the overlayer LNO (LMO) thickness of *n* (*m*) was varied from 0 monolayer (ML) to 5 ML and 20 ML, while the bottom LMO (LNO) thickness was fixed at 20 ML. The heterostructures were subsequently annealed at 400°C for 45 min under an atmospheric pressure of oxygen to fill residual oxygen vacancies. After cooling to below 100°C, the samples were transferred into the analysis chamber under an ultrahigh vacuum of 10^{-10} Torr. XAS spectra were acquired at room temperature by measuring the sample drain current. Background of XAS spectra at the both Mn-$L_{2,3}$ and Ni-$L_{2,3}$ edge were assumed to be hyperbolic tangent functions. Ni- $L_{2,3}$ XAS and Mn-$L_{2,3}$ XAS spectra were normalized by the area intensity of Ni- $L_{2,3}$ XAS and Mn-$L_{2,3}$ XAS, respectively. I also confirmed the formation of a chemically abrupt interface of LMO/LNO (LNO/LMO) by high-angle annular dark-field scanning transmission-electron microscopy (HAADF-STEM) and atomically resolved electron energy-loss spectroscopy (EELS) measurements have been performed using an FEI Titan Cubed aberration-corrected transmission electron microscope operated at 300 kV, as well as *in situ* photoemission spectroscopy (PES) measurements using a Scienta SES2002 analyzer. Photon energies and binding energies were calibrated by measuring a gold film electrically connected to the samples.

The surface morphology of the measured films was analyzed by *ex situ* atomic force microscopy in air. The crystal structure was characterized by synchrotron-based x-ray diffraction (SR-XRD) measurements performed at the BL-4C beamline of KEK-PF.

5.3 Results and Discussion

7.3.1 Growth and characterization of $LaNiO_3$-$LaMnO_3$ bilayers

The typical intensity oscillations of the specular spot with RHEED used for thickness control is depicted in Fig. 5.3. Figures 5.4 (a) and (b) show RHEED patterns of 20-ML LNO/LMO and 20-ML LMO/LNO, respectively. Clear streak patterns indicate that single crystal and flat surfaces are obtained for both LNO/LMO and LMO/LNO bilayers. AFM images of 20-ML LNO/LMO and 20-ML LMO/LNO, which are the thickest bilayers, are depicted in Figs. 5.5 (a) and (b), respectively. Atomically flat surfaces with step-and-terrace structures, which reflect the morphology of the Nb:STO substrate, are clearly observed for not only the thickest bilayers but also all the measured samples, indicating that not only the surface as well as the buried interfaces are atomically flat for all samples. In order to evaluate the in-plane orientation between LNO/LMO and LMO/LNO bilayers, and Nb:STO substrate, reciprocal space mappings were carried out using SR-XRD. Figure 5.6 shows a reciprocal space mappings around (103) reciprocal point of 20-ML LNO/LMO and 20-ML LMO/LNO bilayers, where the reciprocal-space coordinates correspond to the cubic Nb:STO substrate. For both bilyaers, complex diffraction pattern derived from bilayer (Asterisk in Fig. 5.6), which is the combination of the diffraction peaks of an LNO and an LMO layer in addition to Laue's

intensity oscillations, is clearly observed along the same *H* value with the Nb:STO diffraction peak. This indicates both LNO/LMO and LMO/LNO bilayers coherently grows on Nb:STO substrate with the same in-plane lattice constant with a Nb:STO substrate.

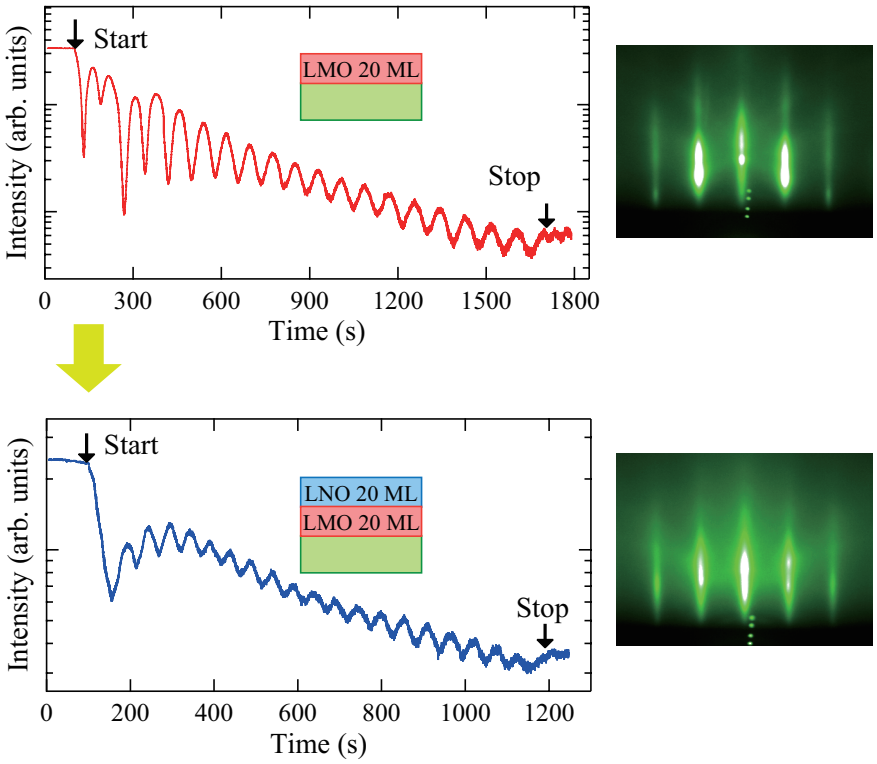

Figure 5.3: Intensity oscillations of the specular spot of RHEED pattern during the 20-ML LNO/20-ML LMO bilayer growth and RHEED patterns after each layer growth.

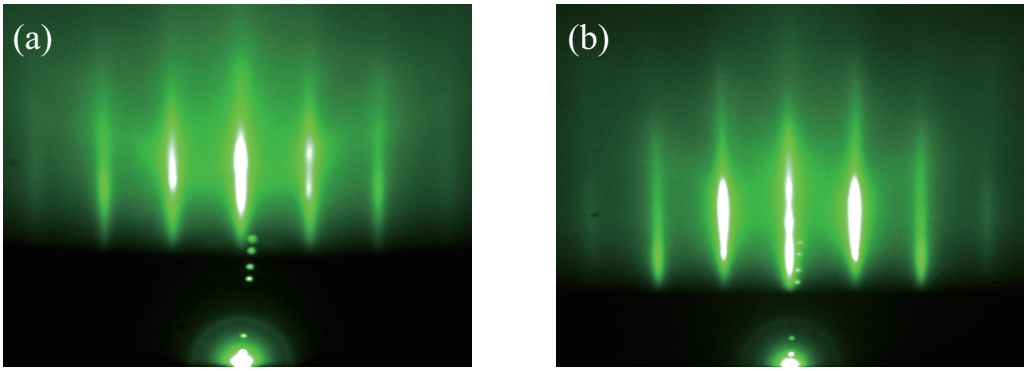

Figure 5.4: RHEED patterns of (a) 20-ML LNO/20-ML LMO bilayer and (b) 20-ML LMO/20-ML LNO bilayer.

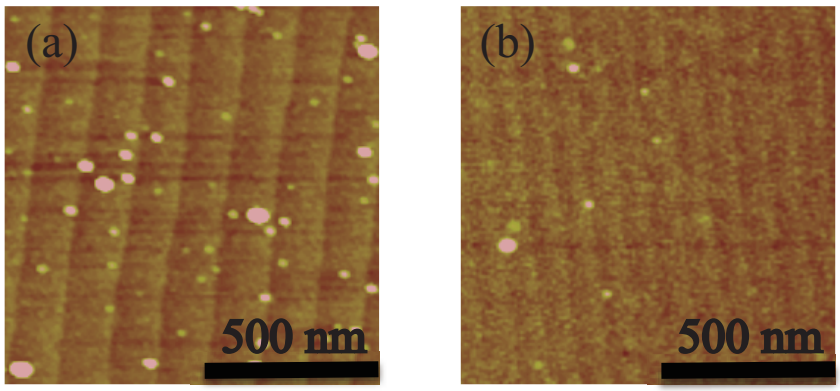

Figure 5.5: AFM images of (a) 20-ML LNO/20-ML LMO bilayer and (b) 20-ML LMO/20-ML LNO bilayer.

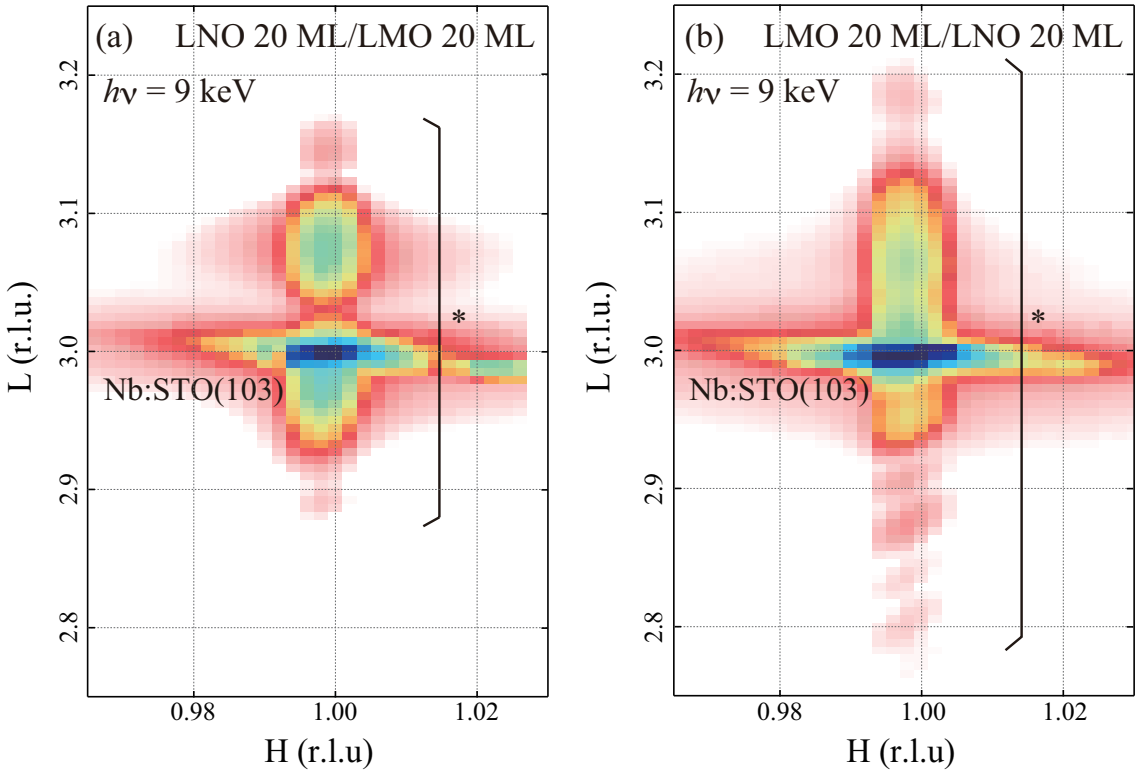

Figure 5.6: Reciprocal space mappings around (103) reflection of (a) 20-ML LNO/LMO and (b) 20-ML LMO/LNO bilayers. Asterisk (*) represents the diffraction patterns of combination of an LNO and an LMO layer, and Laue's intensity oscillations. The reciprocal-space coordinates correspond to the cubic STO substrate.

5.3.2 Confirmation of chemical abruptness at the interface

In order to evaluate the interface roughness of the LNO/LMO and LMO/LNO bilayers, HAADF-STEM and atomically resolved EELS measurements have been performed. Figure 5.7 shows HAADF-STEM images and EELS maps of constituent elements for both the bilayers, together with the intensity plots of corresponding Ni and Mn atoms. Integrated intensity plots of La-$M_{4,5}$ and Ni-$L_{2,3}$ edge, and Mn-$L_{2,3}$ edge along growth direction are depicted in Fig. 5.8. In HAADF-STEM images, because the intensity is roughly scaled by $Z^{\sim 1.7}$, where Z

is the value of atomic number, the brighter spots correspond to the position of La (Z = 57) atoms and weaker spots with similar intensity between correspond to Ni (Z = 28) and Mn (Z = 25) atoms. Owing to energy proximity of La and Ni edge, and La EELS peaks are strong in their intensity, only Ni spectra cannot be extracted from La-$M_{4,5}$ and Ni-$L_{2,3}$ EELS spectra. The bright circular spots in the image of each EELS map, which are depicted by open circle symbols, indicate that the existence of the atoms. However, I cannot decide the presence or absence of the atoms by blurred images depicted by circle symbols with dashed line in the 1 ML interface regions of both La-$M_{4,5}$ and Ni-$L_{2,3}$ map, and Mn-$L_{2,3}$ one. Because the integrated intensity value of EELS spectra in itself shown in Fig. 5.8 has the uncertainness of the background derived from delocalization effects in TEM measurements, I plot the intensity difference between the peak and the valley of spectra in order to assign the presence or absence of atoms, as shown in rightmost graphs of Fig. 5.7 (a) and (b). As for Ni atoms, the small difference between the peak and the valley indicates the existence of Ni atom whereas the large difference means the absence of Ni atom because the peaks of the integrated intensity of La-$M_{4,5}$ and Ni-$L_{2,3}$ EELS spectra are derived from La atoms while Ni atoms are located at the position with intensity valley. On the other hand, as for Mn atoms, the large intensity difference of peak-to-valley suggests the presence of Mn atoms because intergrated intensity peaks of Mn-$L_{2,3}$ EELS spectra are derived from Mn atoms. As can be seen in Fig. 5.7, it is evident that the chemically abrupt interfaces are formed for both LNO/LMO and LMO/LNO bilayers: The spatially resolved EELS elemental maps demonstrate that the interface roughness due to possible intermixing of Ni and Mn ions is less than 1 ML for the both bilayers. Furthermore, there is no detectable structural difference between LNO/LMO and LMO/LNO interfaces irrespective of the growth order.

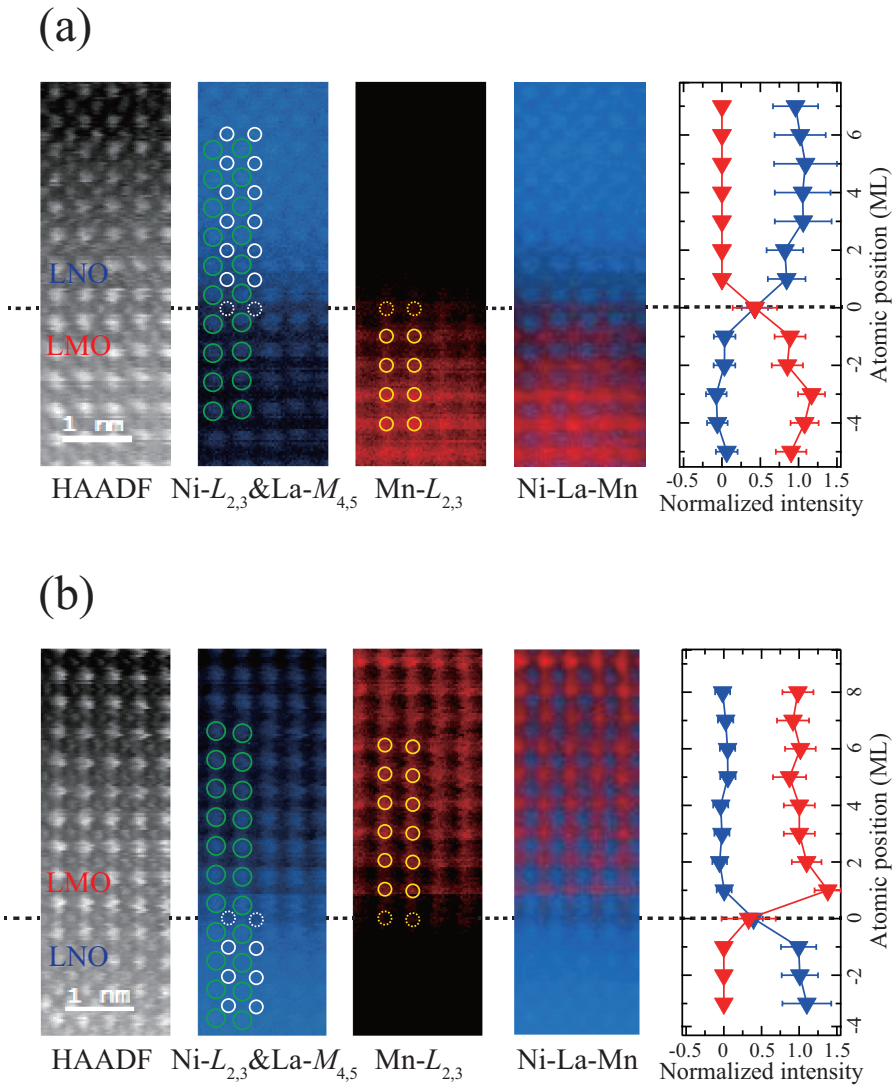

Figure 5.7: Cross-sectional HAADF-STEM images and atomically resolved EELS maps for (a) LNO/LMO and (b) LMO/LNO bilayers, together with the intensity plots of corresponding Ni (blue data markers) and Mn (red data markers) atoms. EELS maps are ordered from left to right for Ni-$L_{2,3}$ and La-$M_{4,5}$ edge, Mn-$L_{2,3}$ edge, and the sum of these EELS images with Ni&La in blue and Mn in red. The bright spots in the EELS maps are corresponding to each atom: Atomic positions of La, Ni, and Mn are depicted by green, white, and yellow open circles, respectively. In the intensity plot, the signals from Ni and Mn atoms are extracted from the EELS maps, and plotted as a function of atomic position. Black dashed line indicates the interface between the two constituent oxides.

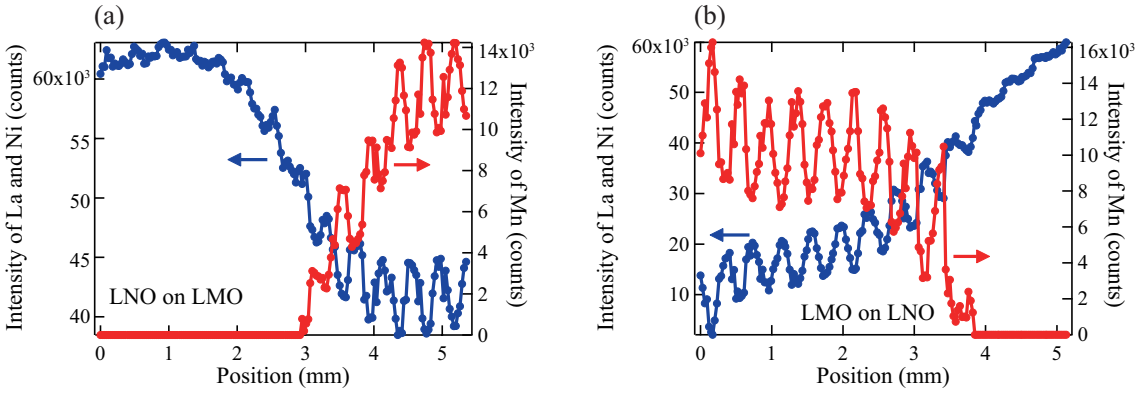

Figure 5.8: Integrated intensity plot of Ni-$L_{2,3}$ and La-$M_{4,5}$ edge (blue), and Mn-$L_{2,3}$ edge (red) for (a) LNO/LMO and (b) LMO/LNO bilayers.

The formation of chemically abrupt interfaces has been further confirmed by comparing the relative intensities of core levels as a function of overlayer thickness with a simulated photoelectron attenuation function. Figures 5.9 (a) and (b) show the core-level spectra of LNO/LMO bilayers with varying LNO overlayer thickness of *n* and LMO/LNO bilayers with varying LMO overlayer thickness of *m*, respectively. With increasing the thickness of the LNO (LMO) overlayer, the intensity of the Ni-3*p* (Mn-3*p*) core-level peak emitted from the overlayer increases, while that of Mn-3*p* (Ni-3*p*) derived from the underlayer exponentially smears. These behaviors of the core-level intensity as a function of overlayer thickness strongly suggest the formation of chemically abrupt interfaces in both bilayers.

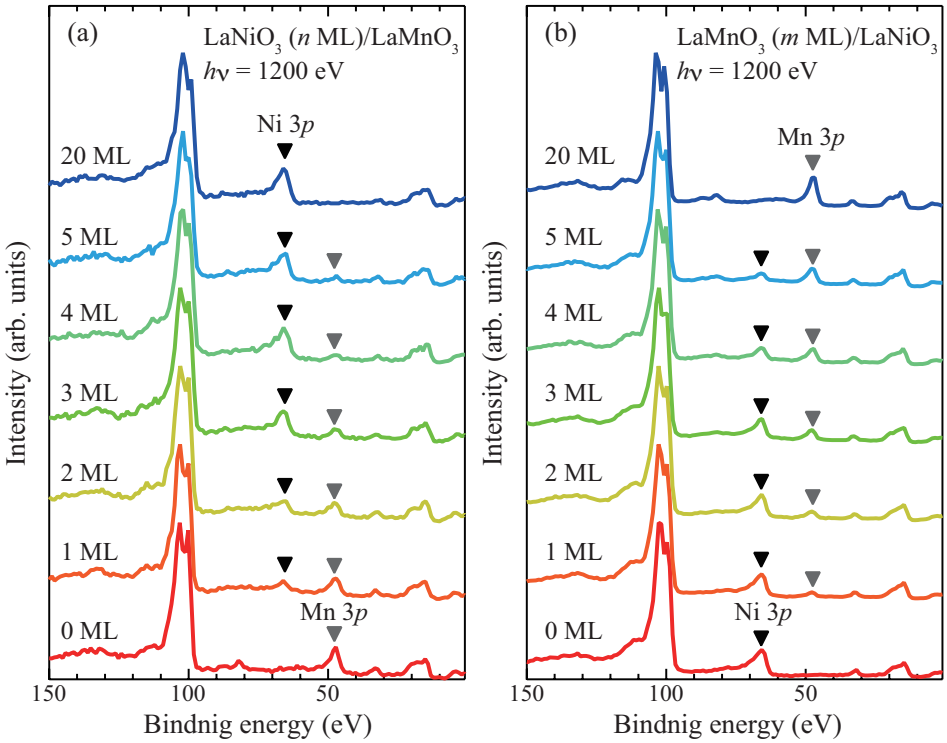

Figure 5.9: Core-level spectra of LNO (*n* ML) /LMO (a) and LMO (*m* ML)/LNO (b) with varying overlayer thickness of *n* and *m*.

To evaluate this abruptness quantitatively, I plotted the core-level intensity ratio of underlayer to overlayer in Fig. 5.10 as a function of overlayer thickness. Furthermore, I compared the results with a simulation based on the photoelectron attenuation function. Assuming a chemically abrupt interface, the core-level intensity ratio ($I_{underlayer}$/ $I_{overlayer}$) is given by the following equation;

$$\frac{I_{underlayer}}{I_{overlayer}} = \frac{Const.}{\exp\left(\frac{a}{\lambda}\cdot n\right)-1} \qquad (5.1)$$

Here, *a* is the lattice constant, *n* is the number of the overlayer, and λ is the mean free path of photoelectrons. The mean free path of photoelectrons in LNO and LMO layer is estimated to be 1.90 nm and 1.98 nm, respectively, according to the TPP-2M code [104]. The value of *a* is assumed to be equal to the *c*-axis lattice parameter of strained LNO film (3.81 Å) and LMO film (3.95 Å) grown on Nb:STO substrates, which are evaluated by $2\theta/\theta$ scans of 100-ML LNO and 100-ML LMO films in XRD measurements, respectively. The good agreement between the experimental and calculated results clearly indicates that a chemically abrupt interface is formed for both LNO/LMO and LMO/LNO heterostructures within the experimental margins.

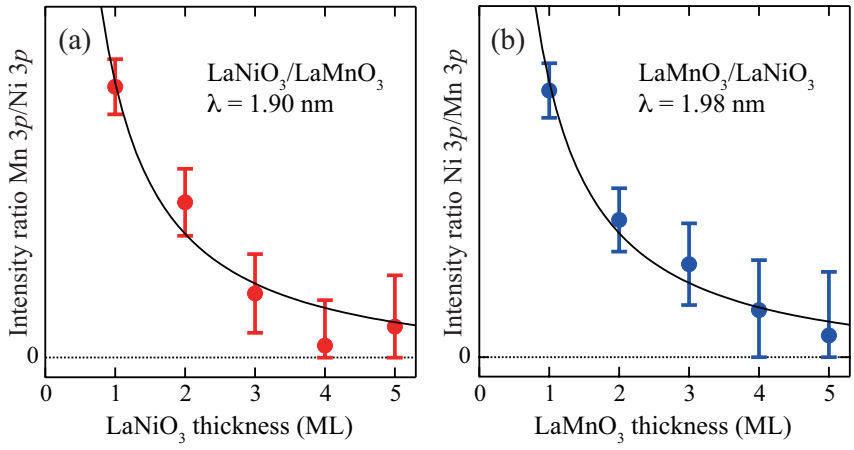

Figure 5.10: Plots of the intensity ratio of core levels as a function of the overlayer thickness (closed circles with error bars), with the simulated curve based on Eq. 5.1 (black line). (a) Ratio of Mn 3*p* to Ni 3*p* core-level intensity for LNO/LMO bilayers. (b) Ratio of Ni 3*p* to Mn 3*p* core-level intensity for LMO/LNO.

May *et al*. have reported that structural asymmetry of interfacial roughness in LMO-$SrMnO_3$ (SMO) superlattices: LMO/SMO interface is atomically smooth within 1 ML, while SMO/LMO interface has plateaus and valley with height of 2 ML [105]. As for LNO/LMO heterostructures, it has been also reported in very recent studies [106] that there is a structural interface asymmetry in these systems: The LNO/LMO interface displayed 2–3 ML roughness in contrast to a sharp LMO/LNO interface. However, in this study, from the STEM observations and the analysis of core-level intensity, it has been confirmed that the chemically abrupt interfaces are formed at both present LMO/LNO and LNO/LMO heterojunctions, although it is difficult to eliminate the possibility of the existence of local roughness at the interface completely from these analyses.

5.3.3 Valence change due to the charge transfer

Figure 5.11 shows the Ni-$L_{2,3}$ (Mn-$L_{2,3}$) XAS spectrum, Ni (Mn) $2p \rightarrow 3d$ transition, of the LNO (LMO) overlayer of an LNO/LMO (LMO/LNO) bilayer with the LNO (LMO) overlayer thickness of n (m) = 1, together with that of an LNO (LMO) film as a reference for the Ni^{3+} (Mn^{3+}) state. Because the Ni-L_3 edge structure partially overlaps with the La-M_4 edge owing to the close proximity of the two energy levels, the Ni-$L_{2,3}$ XAS spectra were extracted by subtracting the contribution of the La-M_4 edge from the raw spectra, as shown in the inset of Fig. 5.11 (a). For both the LNO and LMO layers, the spectral shapes of the single-layer and the bilayer films exhibit considerable differences.

Comparing the Ni-$L_{2,3}$ spectra with those of $R$$NiO_3$ [R: rare earth] (Ni^{3+}) and NiO (Ni^{2+}) in previous reports [85] (see Fig. 4.2), the formal valence of the Ni ions is changed from 3+ in the original LNO film to almost 2+ in the LNO overlayer. This result strongly suggests that electrons are transferred from the LMO layer to the LNO layer in the interface region. The

occurrence of electron transfer from Mn to Ni ions is further supported by the fact that spectral changes indicative of such a formal valence modulation have not been observed in thickness-dependent XAS measurements of LNO/$LaAlO_3$ interfaces, as depicted in Fig.5.12, because the valence of Al ion is robust [107].

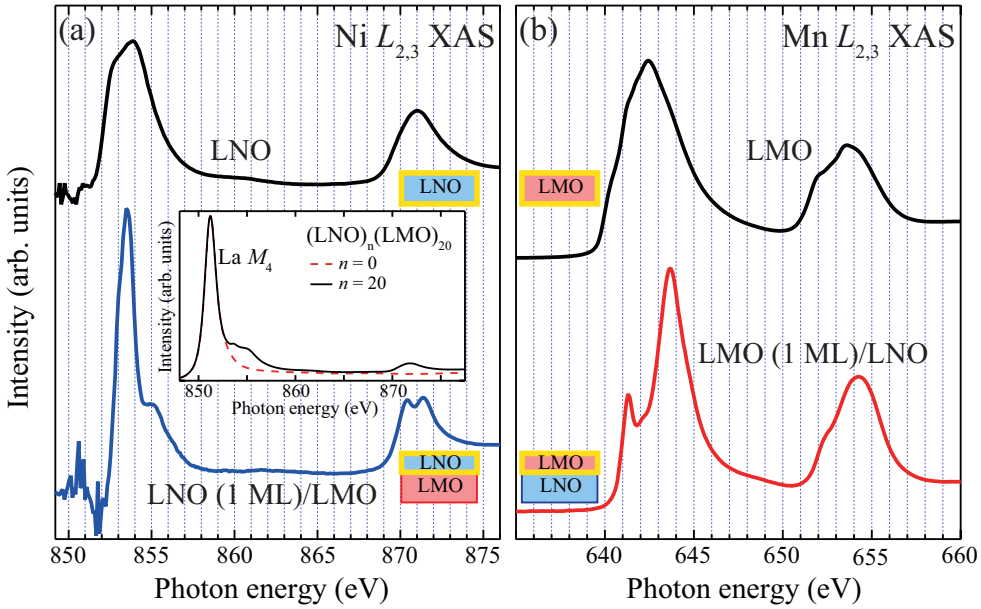

Figure 5.11: (a) Ni-$L_{2,3}$ XAS spectra of an LNO film and the 1-ML LNO overlayer of an LNO/LMO bilayer structure. The inset shows the XAS spectra taken around the Ni-$L_{2,3}$ and La-M_4 edges for LNO and LMO films. The Ni-$L_{2,3}$ XAS spectra have been extracted by subtracting the XAS spectrum of an LMO film representative of the La-M_4 edge from the corresponding raw XAS spectra of LNO. (b) Mn-$L_{2,3}$ XAS spectra of an LMO film and the 1-ML LMO overlayer of an LMO/LNO bilayer structure.

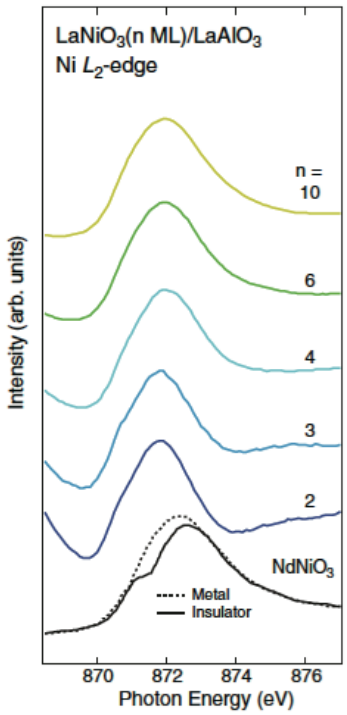

Figure 5.12: Ni-L_2 XAS spectra of LNO films on $LaAlO_3$ substrates [107].

As for the counterpart LMO layers, the Mn-$L_{2,3}$ XAS spectra in Fig. 5.11 (b) show the simultaneous occurrence of hole doping in LMO layers as expected. An additional sharp pre-edge structure appears at around 641.3 eV and the position of the most prominent peak shifts towards higher photon energies by about 1.6 eV. This is the same spectral change from Mn^{3+} to Mn^{4+} proposed by Abbate *et al*. (See Fig. 4.3) [87] and this result indicates significant evolution of the Mn^{4+} states in the LMO overlayer of the LMO/LNO bilayers from the Mn^{3+} states in the original LMO films.

Because the constituent perovskite oxide layers of my samples have the common A-site composition of an LaO atomic layer, the MnO_2 and NiO_2 atomic layers are not subjected to chemical carrier-concentration modulation at the interface caused by the intermixing of A-site cations, which has been shown to lead to inadvertent doping. Thus, these results clearly demonstrate the occurrence of electron transfer from Mn ions to Ni ions across the interface. It

should be noted that almost the same results were obtained for the sandwiched structures of LNO/LMO/LNO for LMO layers, as well as LMO/LNO/LMO for LNO layers. The observed trend of interfacial charge transfer of $Ni^{3+} + Mn^{3+} \rightarrow Ni^{2+} + Mn^{4+}$ is consistent with results reported for LNO/LMO superlattices [25, 102] and $La_{0.75}Sr_{0.25}MnO_3$/LNO bilayers [21], as well as for double perovskite La_2NiMnO_6 [57, 68] and agreement with the trend expected from the redox potential as mentioned in Chapter 1 [28].

In order to further consider the origin of the charge transfer, I have investigated the electronic structure of the valence band at the heterojunction. Figure 5.13 shows the electronic structures predicted at the LNO/LMO heterointerface. The left side is the valence band spectra of LNO and LMO obtained by PES measurements. The valence band of LNO (LMO) are considered to consists of O 2*p* and Ni (Mn) 3*d* states, as well as their hybridization. As depicted in Fig. 5.13, each structure in the valence band of LNO (LMO) can be assigned as the Ni (Mn) 3*d* e_g, Ni (Mn) 3*d* t_{2g}, O 2*p* and hybridization of Ni (Mn) 3*d* and O 2*p* states, respectively [92, 93] and the schematic images of the valence band structure are illustrated on the right side of Fig. 5.13. When an LNO/LMO heterojunction is formed, the same oxygen ion located at the interface is shared by both LNO and LMO. And then the electronic structures are realigned with the same energy position of each O 2*p* states, resulting in the difference of chemical potentials between the LNO and LMO side, shown in the right side of Fig. 5.14 In order to make a settlement of this difference, it is inferred that electron transfer occurs [108] from the Mn 3*d* state to the Ni 3*d* state though the shared oxygen ion at the heterointerface.

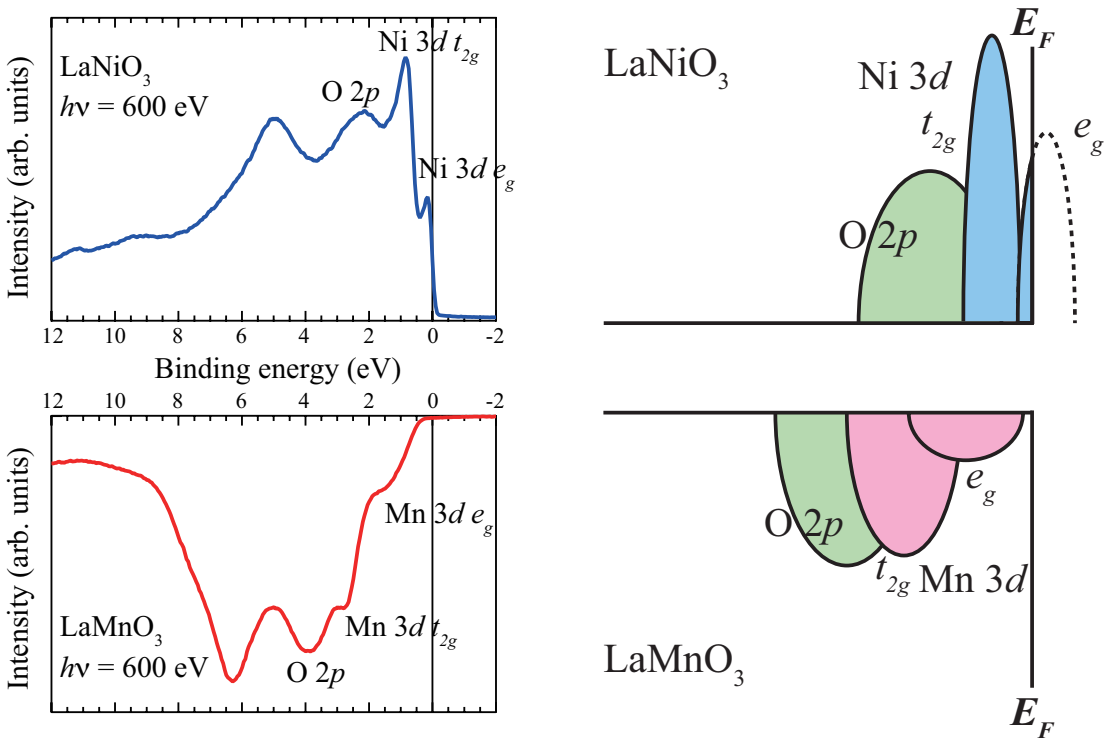

Figure 5.13: (Left) Valence band spectra of LNO and LMO measured by *in situ* PES. (Right) Schematic images of valence band of LNO and LMO.

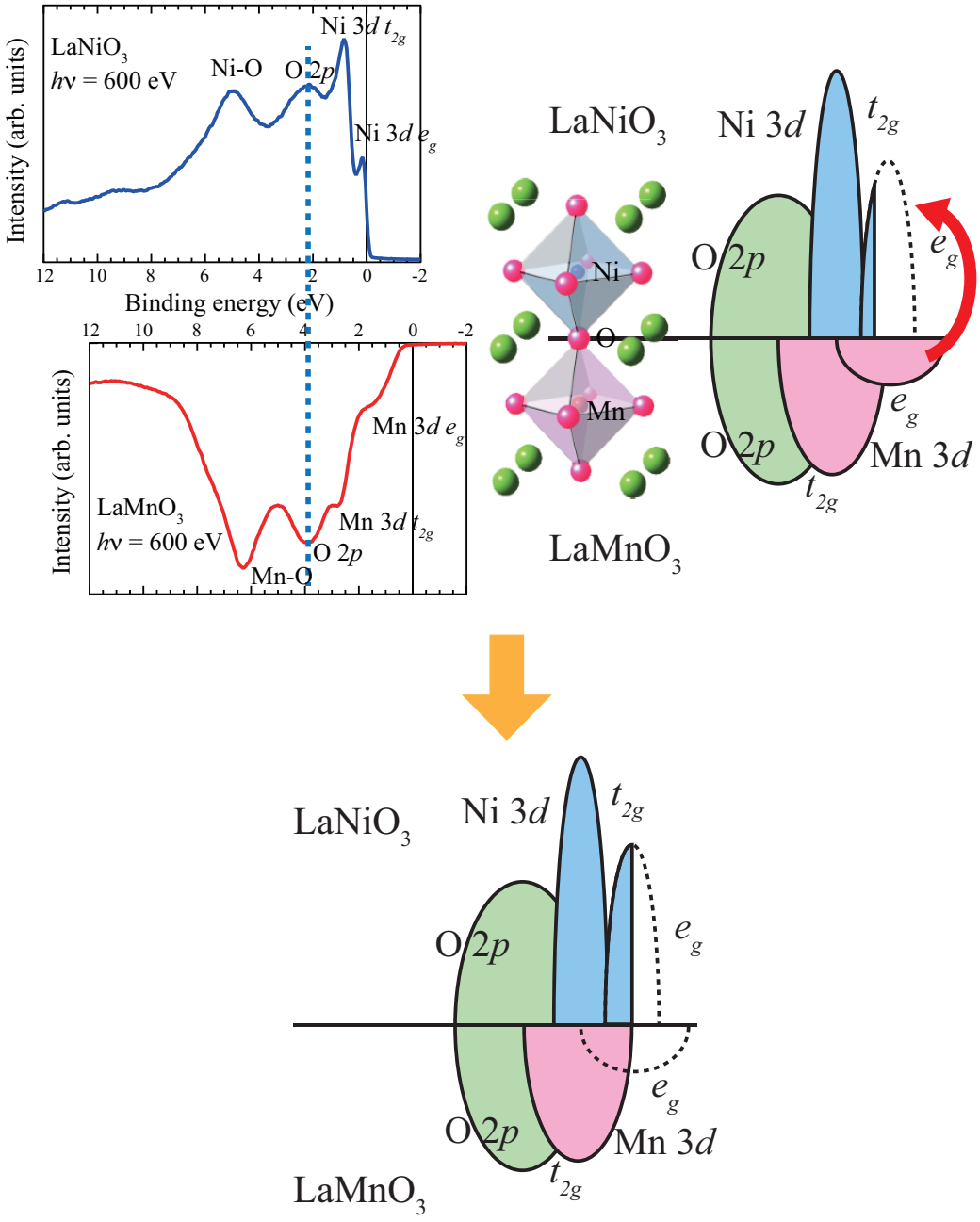

Figure 5.14: The electronic structures predicted at the LNO/LMO interface. In order to make a settlement of the difference of the chemical potentials between LNO and LMO, the electron transfer from Mn to Ni are expected to occur.

5.3.4 Approach for evaluation of the spatial distribution of charge transfer

The next crucial issue is how the charges are spatially distributed across the heterointerface. In general, the spatial (depth) distribution of formal valence states in heterostructures is addressed by measuring the thickness dependence of the *overlayer*, as shown in Fig. 5.15 (a)–(c). The overlayer thickness is controlled by the deposition time [Fig. 5.15 (a)→(c)] or the etching time of sputtering [Fig. 5.15 (c)→(a)]. However, owing to the surface sensitivity of photoelectron measurements, the analysis of these measurements usually suffers from spurious surface-derived states and a complicated analytical procedure due to photoelectron attenuation [22]. In order to overcome these difficulties, I propose an analytical procedure that enables the spatial distribution of the interfacial charge transfer to be determined utilizing the elemental selectivity of XAS: Probe the change in the electronic structure of the *underlayer* (buried interface) as a function of overlayer thickness, as shown in Fig. 5.15 (d)–(g). When a junction is formed, the spectral shape of the underlayer (original film) changes, reflecting the occurrence of the interfacial charge transfer [Fig. 5.15 (d) and (e)]. With increasing overlayer thickness, the spectral shape of the underlayer continuously changes as long as the overlayer thickness is less than the characteristic length scale of charge transfer [Fig. 5.15 (e)→(f)]. Once the overlayer thickness is comparable to the characteristic length, i.e., the interfacial charge transfer is completed after the deposition of an overlayer with a certain thickness, the spectral change of the underlayer should be saturated [Fig. 5.15 (f)→(g)]. Thus, one can determine the length scale of the charge transfer in the *overlayer* oxides by measuring the saturation of spectral change in the *underlayer* oxides.

Although it is difficult to evaluate the amount of transferred charges itself, the present analytical procedure has several advantages in comparison with the conventional method. First,

owing to the elemental selectivity of XAS, the interface of the underlayer with the overlayers is defined as the "surface" of the underlayer [21]. Namely, changes in the interfacial electronic structure on the underlayer side are detected from the interface side. Second, as a result of the elemental selectivity, information on the buried material is obtained separately without influence from surface-derived states (i.e., surface reconstruction and/or off-stoichiometry due to preferential sputtering effect) of the overlayer material. Third, because changes in the XAS spectra of the underlayer are used as an "indicator" of charge transfer, it is not necessary to consider the photoelectron attenuation (probing depth) of XAS measurements and the associated complicated analytical procedure at each overlayer thickness to determine the charge transfer length.

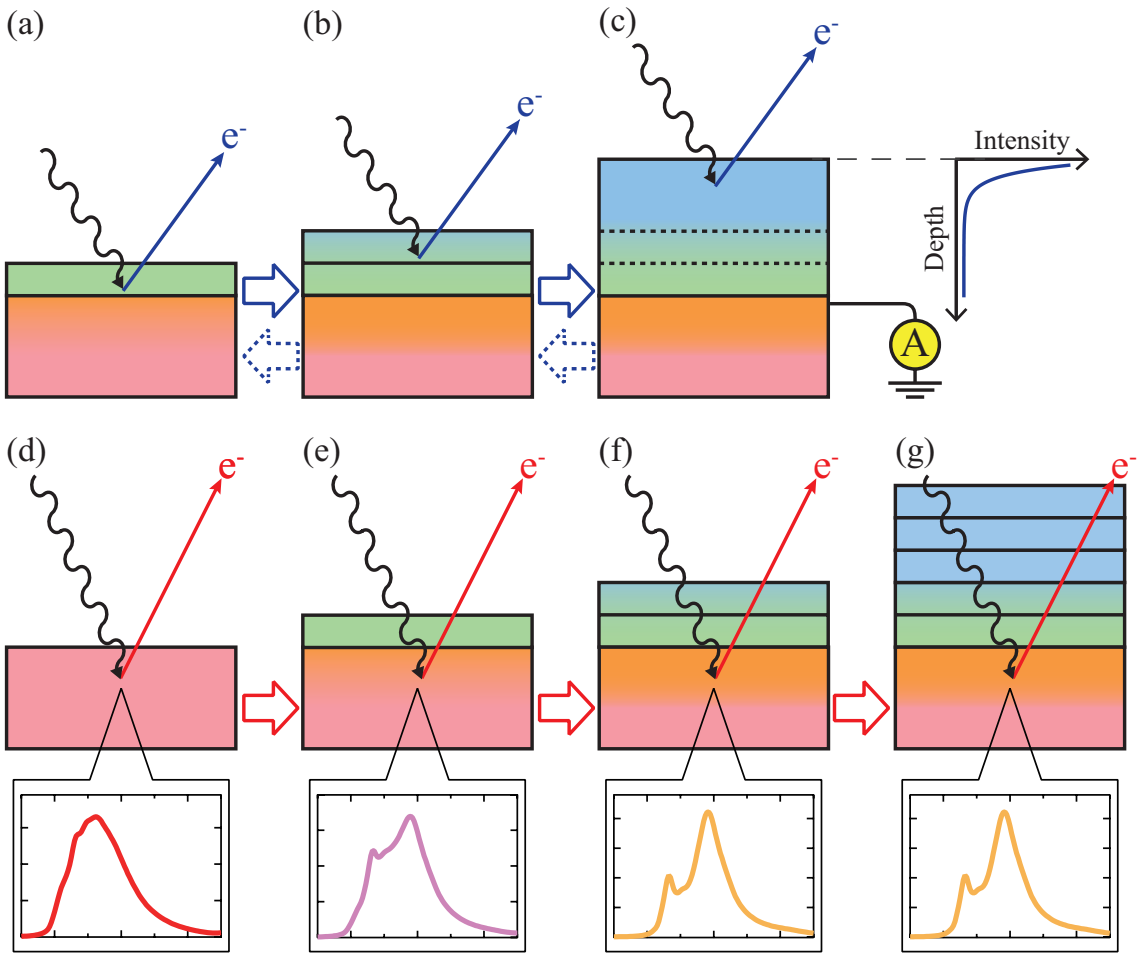

Figure 5.15: Schematic images of the conventional method (a)–(c) and the proposed approach in the present study (d)–(g) used to investigate the interfacial charge transfer phenomena. In the conventional method, the change in the electronic structure of the overlayer is investigated as a function of overlayer thickness. In the proposed method, the change in the electronic structure of the *underlayer* (buried interface) is evaluated as a function of overlayer thickness using the elemental selectivity of XAS measurements.

5.3.5 Spatial distribution of the transferred charge

Figure 5.16 (a) shows the Mn-$L_{2,3}$ XAS spectra of the LMO *underlayer* of LNO/LMO bilayers with varying LNO overlayer thickness *n*. In order to show the variation more clearly, Figure 5.17 (a) depicts a comparison of the Mn-L_3 XAS spectra of LNO/LMO bilayers with that of the 1-ML LMO overlayer grown on LNO shown in the bottom panel of Fig. 5.11 (b) used as the reference XAS spectrum for Mn^{4+} states. When 1-ML LNO is deposited, the spectra exhibit small but distinct changes: An additional shoulder structure appears at the photon energy of ~643.7 eV, which is attributed to the evolution of additional Mn^{4+} state in the interface region of the LMO underlayer as a result of charge transfer. As the overlayer thickness is increased from 1 ML, the spectra remain unchanged within the experimental accuracy (shown in Fig. 5.18 (a)), suggesting that charge transfer between LNO and LMO layer comes to equilibrium at only 1-ML LNO deposition. This result indicates that the transferred electrons from the LMO side are confined in the interface region of the 1-ML LNO layer.

In the case of counterpart hole distribution in the LMO layers, the similar thickness dependence is observed in the Ni-$L_{2,3}$ XAS spectra of the LNO *underlayer* of LMO/LNO bilayers as a function of LMO overlayer thickness, as shown in Fig. 5.16 (b). Fig. 5.17 (b) shows a comparison of Ni-L_2 XAS spectra of the LMO/LNO bilayer with the 1-ML LNO overlayer grown on LMO in the bottom panel of Fig. 5.11 (a) used as the reference for Ni^{2+} states because the Ni-L_3 edge can be more influenced by the subtraction process of La-M_4 edge. When the LMO layers are deposited, a sharp peak structure characteristic of Ni^{2+} states gradually appears at ~853.6 eV in Ni-L_3 edge and shoulder structure evolves at ~870.5 eV in Ni-L_2 edge. The sharp peak and additional shoulder structure evolve as the LMO overlayer thickness is increased to 3–4 ML, reflecting the increase in the amount of extra Ni^{2+} states in the LNO underlayer near the interface. Judging from the saturation of the spectral changes in the Ni-$L_{2,3}$ XAS spectra (shown in Fig. 5.18 (b)), the induced holes in the LMO caused by the

charge transfer are distributed in the region 3–4 ML from the interface. By combining the results of the XAS measurements of LNO/LMO and LMO/LNO bilayers, it is clear that the interfacial region subject to the charge transfer is different for each of the two constituent layers: Extra electrons are accommodated in 1 ML of the LNO layers, while extra holes are distributed over 3–4 ML in the counterpart LMO layer.

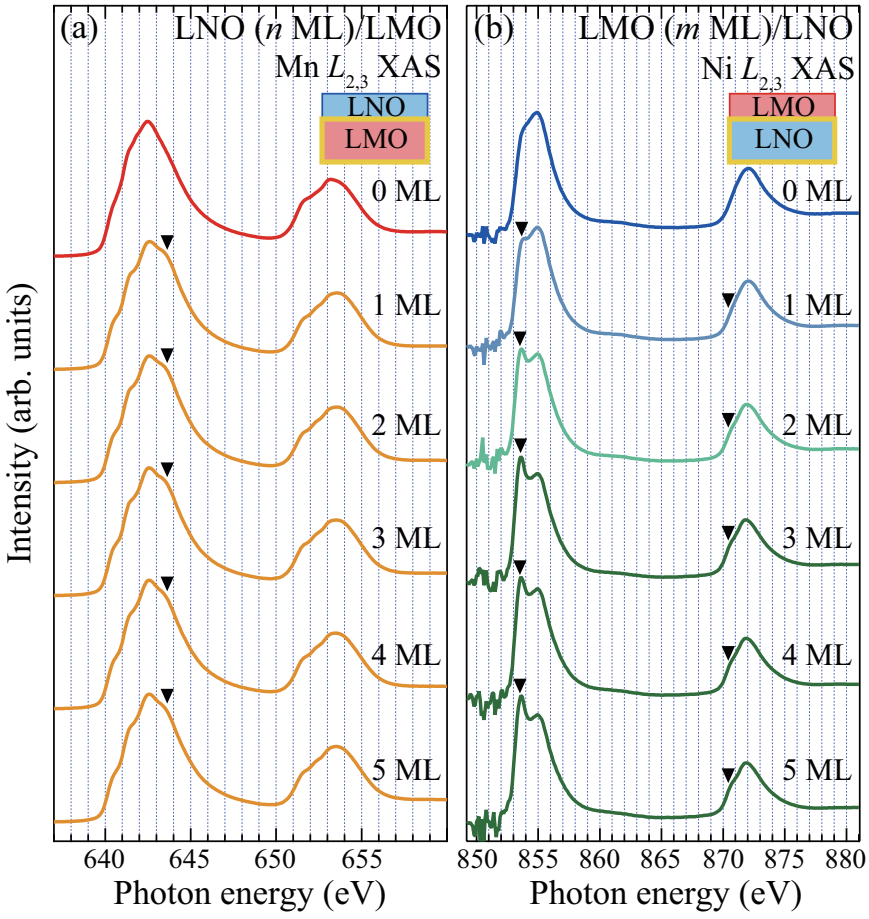

Figure 5.16: (a) Mn-$L_{2,3}$ XAS spectra of the LMO *underlayer* of LNO/LMO bilayers with varying LNO overlayer thickness n. (b) Ni-$L_{2,3}$ XAS spectra of the LNO *underlayer* of LMO/LNO bilayers with varying LMO overlayer thickness m. The contribution of the La-M_4 edge has been subtracted. The triangular arrows indicate the representative changes due to the interfacial charge transfer.

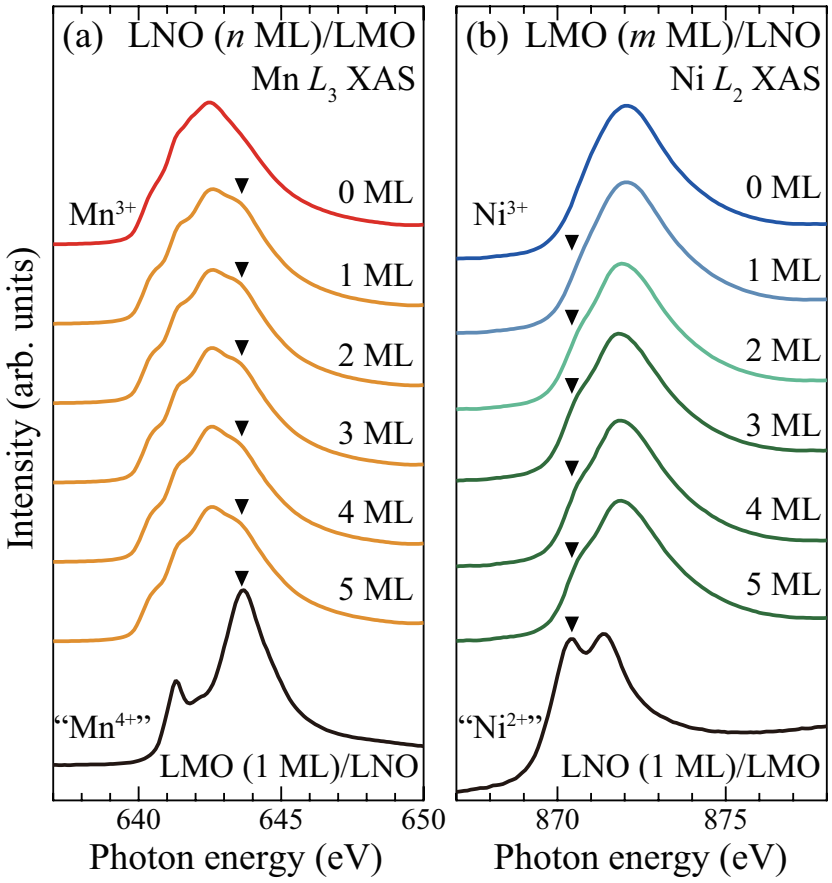

Figure 5.17: (a) Mn-L_3 XAS spectra of the LMO *underlayer* of LNO/LMO bilayers with varying LNO overlayer thickness *n*, in comparison with that of the 1-ML LMO overlayer grown on LNO. The shoulder structures at the photon energy of ~643.7 eV that are attributed to Mn^{4+} states are indicated by arrows. (b) Ni-L_2 XAS spectra of the LNO *underlayer* of LMO/LNO bilayers with varying LMO overlayer thickness *m*, in comparison with that of the 1-ML LNO overlayer grown on LMO. The shoulder structures derived from Ni^{2+} states are indicated by arrows.

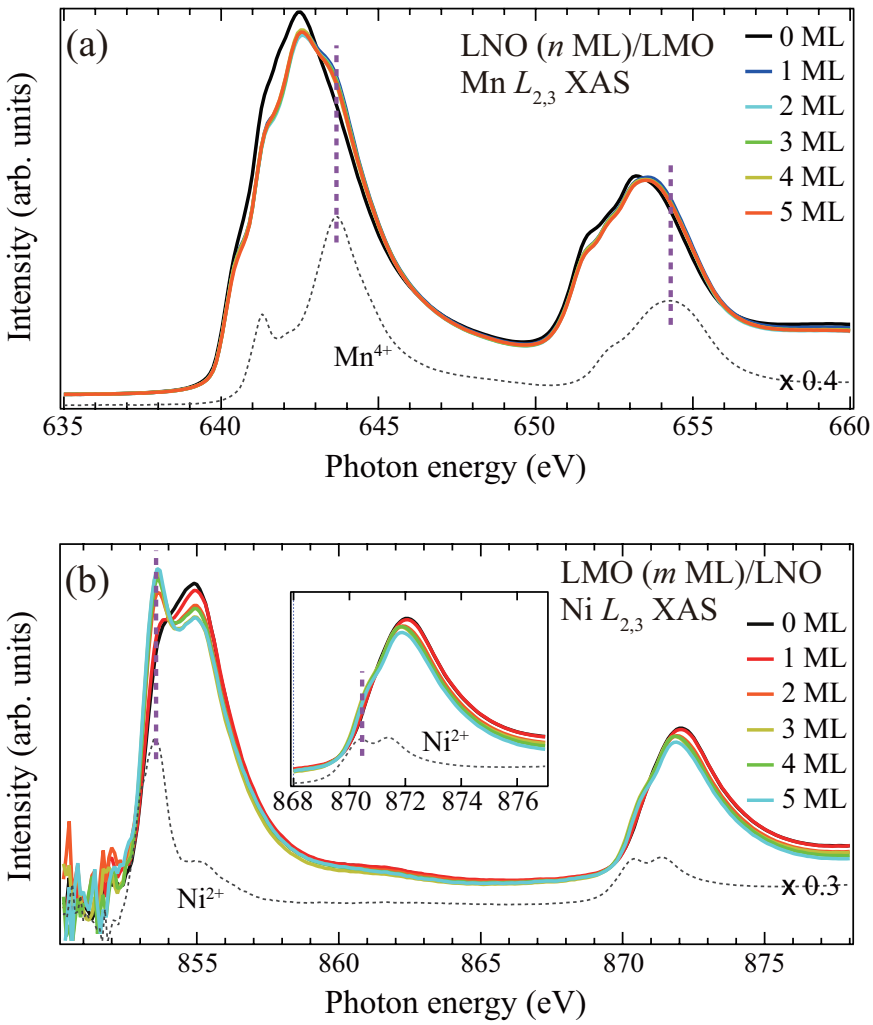

Figure 5.18: Piled XAS spectra for a clear display of the spectral change with the variation of overlayer thickness. (a) Mn-$L_{2,3}$ XAS spectra of the LMO *underlayer* of LNO/LMO bilayers with varying LNO overlayer thickness n. (b) Ni-$L_{2,3}$ XAS spectra of the LNO *underlayer* of LMO/LNO bilayers with varying LMO overlayer thickness m.

I have also characterized XAS spectra of the *overlayer* as a function of the overlayer thickness. Figure 5.19 (a) shows Ni-$L_{2,3}$ XAS spectra of the LNO *overlayer* of LNO/LMO

bilayers with varying LNO overlayer thickness. As mentioned above, the formal valence of 1-ML LNO is almost 2+ relative to Ni^{3+} states in 20-ML LNO overlayer, which is the same with that of bulk LNO. It has been confirmed that Ni^{3+} states systematically evolve in the LNO overlayer with increasing the thickness of LNO. This result indicates that the region of valence change from Ni^{3+} to Ni^{2+} is confined close to the LNO/LMO interface and Ni is trivalent far from the interface. In the case of counterpart Mn valence, Fig. 5.19 (b) shows Mn-$L_{2,3}$ XAS spectra of the LMO *overlayer* of LMO/LNO bilayers. The Mn^{4+} is dominant in 1-ML LMO, while the formal valence of Mn is 3+ in 20-ML LMO overlayer. Mn-$L_{2,3}$ XAS spectra demonstrate that the ratio of Mn^{3+} to Mn^{4+} gradually increases with following the increase of the LMO ovelayer thickness, which enables me to conclude that the region of valence change from Ni^{3+} to Ni^{4+} is located near the heterointerface and the valence of Mn is 3+ far from the interface. Although spectral changes of the overlayer XAS are more apparent than those of the underlayer, characterizations of the valence in the *overlayer* make it difficult to evaluate the spatial distribution of the transferred charge for some reasons. First, the XAS spectra of the overlayer may be influenced from surface-derived states. Second, especially for Mn-$L_{2,3}$ XAS, it is hard to reproduce the mixed valence spectra by a linear combination of Mn^{3+} and Mn^{4+} XAS spectrum, which is sometimes used to evaluate the ratio of the valence states in mixed valence compounds [8]

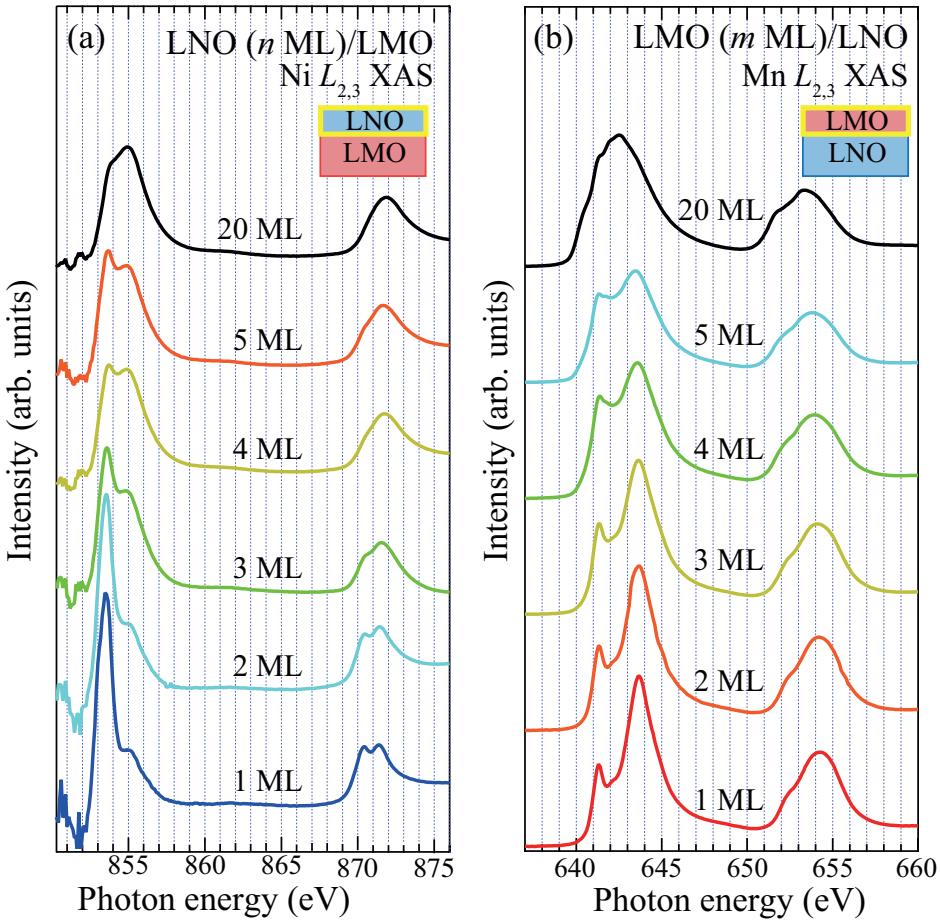

Figure 5.19: (a) Ni-$L_{2,3}$ XAS spectra of the LNO *overlayer* of LNO/LMO bilayers with varying LNO overlayer thickness *n*. (b) Mn-$L_{2,3}$ XAS spectra of the LMO *overlayer* of LMO/LNO bilayers with varying LMO overlayer thickness *m*.

5.3.6 Comparison to previous reports and theoretical calculations

There are some reports about the length scale of charge distribution in perovskite manganite. As for insulating manganites, such as in LMO/$SrMnO_3$ superlattices, the distances

of charge distribution have been evaluated from transport and magnetization measurements (2–4 ML) [13, 19] and polarized neutron reflectivity measurements (~3 ML) [20]. Surprisingly, this length is also similar for conducting manganite: ~4 ML for $La_{0.8}Sr_{0.2}MnO_3$/ $La_{0.2}Sr_{0.8}MnO_3$ superlattices [13] and $YBa_2Cu_3O_{7-\delta}/La_{0.7}Ca_{0.3}MnO_3$ superlattices [109], and ~3 ML for $YBa_2Cu_3O_7/La_{0.67}Ca_{0.33}MnO_3$ superlattices [23]. It should be noted that a characteristic length scale of charge redistribution in perovskite manganite do not depend on its conductivity and the present value of 3–4 ML is a good agreement with those reported for other perovsktie manganites.

I discuss a possible origin of the difference in the length scale of charge transfer between LNO and LMO. First, the Thomas–Fermi (TF) screening length, L_{TF}, for the heterostructure was considered. L_{TF} is given by the following equations [110]:

$$L_{TF} = \left[\frac{\varepsilon\hbar^2}{e^2 m^*}\left(\frac{\pi^4}{3n_0}\right)^{1/3}\right]^{1/2} \quad (5.2)$$

where, ε is the dielectric constant, $\hbar$ is the Planck constant, m^* is the effective mass, n_0 is the carrier density, and e is the elementary charge. Using the range of reported values for LNO (ε of 11.29-13.75ε_0 [111], m^* of 10.3m_0 [112], and n_0 estimated by 1 electron per unit cell) and LMO [ε of 50ε_0 [113], m^* of 15.6m_0 [114, 115], n_0 of 6×10^{20} cm^{-3} as described in Chapter 7], where ε_0 is for vacuum and m_0 is for free electrons, L_{TF} is evaluated to be 0.07–0.08 nm (0.2 ML) and 0.20–0.25 nm (0.5–0.6 ML), respectively. Although these L_{TF} values approximately correspond to the experimental results for metallic LNO, there is a considerable difference for LMO. As mentioned above, because the charge transfer of perovskite manganites shows a common screening length of 3–5 ML irrespective of their ground states, namely the difference in their carrier concentrations, which range from 10^{18} cm^{-3} to 10^{22} cm^{-3}, it has been suggested that the TF screening model is not a good approximation for describing the charge transfer phenomena

occurring at the oxide heterointerfaces. This is simply because the TF approximation only considers the screening of charge in uniform electron gas, where carriers are assumed to be uniformly distributed in space and freely move. The resultant L_{TF} then strongly depends on the carrier concentration. Thus, a theoretical model with a more realistic treatment of the nature of oxide heterostructures, such as the strong on-site Coulomb interactions and the localized character of conduction electrons in 3*d* orbitals, is necessary to describe the difference in screening length.

In order to discuss the microscopic origin of the difference in charge distribution between LNO and LMO, we adopt a more realistic model that treats the Coulomb interaction and electron hopping between transition metal sites. Lin and coworkers [103] have calculated the charge density across an oxide heterostructure based on dynamic mean field theory, and found that the strength of electron hopping among B-site ions, *t*, relative to the Coulomb interaction, $e^2/\varepsilon a$, is a fundamental parameter that expresses charge spreading in constituent oxides, where *t* is the transfer integral, and *a* is the lattice parameter. According to the model, the charge screening length, L_{CS}, is defined as,

$$L_{CS} = \varepsilon t a^2/e^2 \qquad (5.3).$$

Here, we evaluate this screening length in the present case of LNO/LMO heterointerfaces. Parameter *t* is given by,

$$t \approx (pd\sigma)^2/\Delta_{\mathrm{eff}} \quad (5.4)$$

where $(pd\sigma)$ is the Slater–Koster parameter [116] and Δ_{eff} the effective charge transfer energy [2]. Hence, *t* is calculated to be 1.0 eV (0.8 eV) using $(pd\sigma)$ of −1.57 eV (−1.99 eV) [117] and Δ_{eff} of 2.4 eV [93] (4.9 eV [92, 95]) for LNO (LMO), where Δ_{eff} is evaluated from the energy

difference between an occupied non-bonding O 2*p* state and an unoccupied Ni (Mn) 3*d* state [2]. The value of *a* is assumed to be equal to the *c*-axis lattice parameter of strained LNO film (3.81 Å) and LMO film (3.95 Å) grown on Nb:STO substrates, as mentioned above. Using these parameters, L_{CS} is estimated to be 1.4 nm (3.7 ML) for the LNO side and 4.4 nm (11.1 ML) for the LMO side. Although these estimated values are approximately three times larger than the experimental values, which may caused by the overestimation of value of transfer integtral *t* due to not considering the anisotropic hopping of charge, and the spin ordering effect, the ratio of charge spreading length between the two oxides itself (about 3.2) is in good agreement with the present experimental results. In the charge spreading model, the localized electrons hop between transition-metal sites through O 2*p* states and the electron hopping is described by the energy balance between the transfer integral between sites and the Coulomb repulsion. Thus, by considering the case of heterointerface, the charge discretely redistributes from layer (NiO_2 or MnO_2 atomic layer in the present case) to layer. This is a reason of why the charge screening length, L_{CS}, includes the lattice constant "*a*" of a constituent oxide as a parameter. In other words, the unit of screening length in the charge spreading model is a lattice constant [corresponding to one monolayer] of a constituent perovskite oxide. This simple theoretical prediction may describe the spatial distribution of the strongly correlated electrons observed at the interfaces of the transition metal oxides rather than the TF screening model, and thus suggests that the strength of the transfer integral relative to the Coulomb interaction is key to describing the difference in charge spreading length between LNO and LMO. For a quantitative description of the screening length, a more realistic treatment of the electronic structures of the constituent oxides is necessary.

5.4 Conclusion

The charge transfer phenomena across the LNO/LMO heterointerface have been investigated by *in situ* XAS measurements. Ni-$L_{2,3}$ and Mn-$L_{2,3}$ XAS spectra clearly show the occurrence of electron transfer from Mn to Ni ions in the interface region. I have determined the spatial distribution of the transferred charge between the two constituent oxides using the elemental selectivity of the XAS measurements. Analysis of a thickness series of the XAS spectra for LNO/LMO and LMO/LNO bilayers reveals that the spatial distribution of the transferred charges is significantly different between the two constituent layers: 1 ML for LNO and 3–4 ML for LMO. Comparing the theoretical predictions, the observed spatial distribution may be described by the charge spreading model, which takes the transfer integral between neighboring transition metal ions and the Coulomb interaction into account.

Chapter 6
Interfacial ferromagnetism at the heterointerface between perovskite oxides $LaNiO_3$ and $LaMnO_3$

6.1. Purpose of this study

In Chapter 5, *in situ* x-ray absorption spectroscopy (XAS) has carried out to study the charge transfer at the $LaNiO_3$ (LNO)/ $LaMnO_3$ (LMO) hetrointerface. It is found that the electron transfer occurs from Mn to Ni ions and its spatial distribution is significantly different between the two constituent layers: 1 monolayer (ML) for LNO and 3–4 ML for LMO. In order to investigate the relationship between the charge transfer phenomena and the interfacial ferromagnetism, I have performed x-ray magnetic circular dichroism (XMCD) measurements of LNO/LMO heterostructures. I have obtained the magnetic states of Ni and Mn ions by utilizing the elemental selectivity of XMCD.

6.2 Experiments

Digitally controlled LMO/LNO/LMO and LNO/LMO/LNO trilayer structures were fabricated onto 0.1 at. % Nb-doped $SrTiO_3$ (STO) (001) substrates in a laser molecular-beam epitaxy chamber connected to a photoelectron spectroscopic system at beamline BL-2A MUSASHI of KEK-PF. The detailed growth conditions of an LNO and an LMO thin film are already described in Chapter 5. The thicknesses of the LNO and the LMO layers were precisely

controlled by monitoring the intensity oscillation of the specular spot with reflection high-energy electron diffraction (RHEED) during the growth. For the LMO/LNO/LMO trilayers, the middlelayer LNO thickness of *n* was varied from 2 ML to 5 ML, while the top and bottom LMO thicknesses were fixed at 5 ML and 20 ML, respectively. For the LNO/LMO/LNO trilayers, the middlelayer LMO thickness of *m* was varied from 2 ML, 6 ML, to 12 ML, whereas the top and bottom LNO thicknesses were fixed at 5 ML and 20 ML, respectively.

The surface morphology of the measured trilayers was characterized by atomic force microscopy in air. XMCD and XAS spectra were measured at BL-16A of KEK-PF. The magnetic field of about 1 T was applied 30 ° from the sample surface and parallel to the incident beam. The helicity of the incident beam was fixed, while the direction of the magnetic field was switched parallel and antiparallel to it. The XMCD spectra were taken in a total-electron-yield mode at 15 K.

6.3 Results and Discussion

6.3.1 Growth and characterization of $LaNiO_3/LaMnO_3$ trilayers

The typical intensity oscillations of the specular spot with RHEED of a trilayer structure used for thickness control is depicted in Fig. 6.1. Figures 6.2 (a) and (b) show RHEED patterns of LMO/5-ML LNO/LMO and LNO/12-ML LMO/LNO, respectively. Clear streak patterns indicate that single crystal and flat surfaces are obtained for both LMO/LNO/LMO and LNO/LMO/LNO trilayers. Figures 6.3 (a) and (b) depict AFM images of LMO/5-ML LNO/LMO and LNO/12-ML LMO/LNO, which are the thickest trilayers, respectively. Atomically flat surfaces with step-and-terrace structures reflecting the morphology of the

Nb:STO substrate are clearly observed for not only the thickest trilayers but also all the measured samples, indicating that the surface as well as the buried interfaces are atomically flat for all samples. These high-quality trilayers have been investigated by XAS and XMCD.

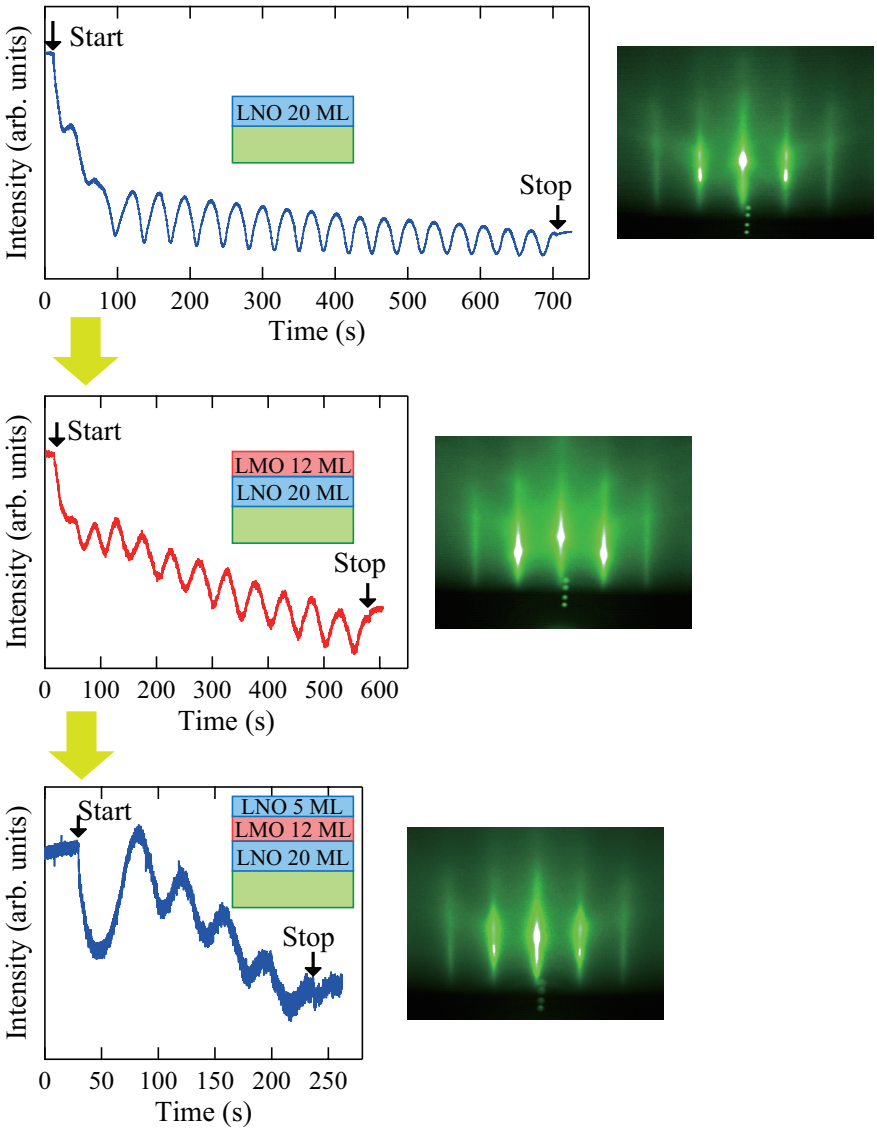

Figure 6.1: Intensity oscillations of the specular spot of RHEED pattern during the 5-ML LNO/12-ML LMO/20-ML LNO trilayer growth and RHEED patterns after each layer growth.

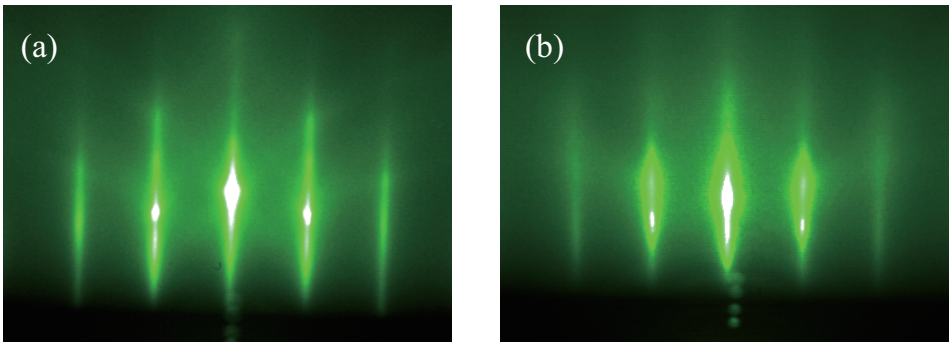

Figure 6.2: RHEED patterns of (a) 20-ML LMO/5-ML LNO/20-ML LMO trilayer and (b) 5-ML LNO/12-ML LMO/20-ML LNO trilayer.

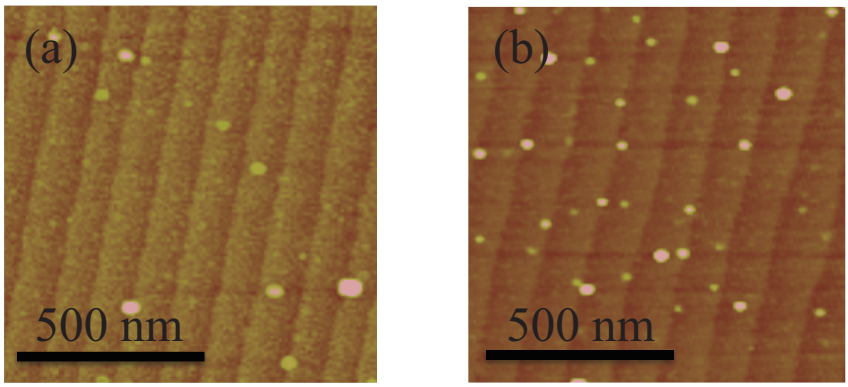

Figure 6.3: AFM images of (a) 20-ML LMO/5-ML LNO/20-ML LMO trilayer and (b) 5-ML LNO/12-ML LMO/20-ML LNO trilayer.

6.3.2 X-ray magnetic circular dichroism study of interfacial ferromagnetism

In order to element-specifically characterize magnetic states of Ni and Mn ions in

LNO-LMO trilayers, XMCD spectra were measured. XAS and XMCD spectra were obtained by the average and the subtraction of a positive magnetic bias XAS and a negative magnetic bias XAS spectrum, respectively. Because the Ni-L_3 edge structure partially overlaps with the very strong La-M_4 absorption edge owing to the close proximity of the two energy levels, the Ni-$L_{2,3}$ XAS spectra were extracted by subtracting the XAS spectrum of an LMO film representative of the La-M_4 edge from the corresponding raw XAS spectra. Background of XAS spectra at the both Mn-$L_{2,3}$ and Ni-$L_{2,3}$ edge were assumed to be hyperbolic tangent functions. Mn-$L_{2,3}$ XAS and XMCD spectra were normalized by the area intensity of Mn-$L_{2,3}$ XAS, whereas Ni-$L_{2,3}$ XAS and XMCD spectra were normalized by area intensity of Ni-L_2 XAS because Ni-L_3 XAS partially overlaps La-M_4 absorption edge and it has a somewhat large analytical error. Figures 6.4 (a) and (b) show Ni-$L_{2,3}$ XAS and XMCD spectra of LMO/LNO/LMO trilayer structures and a 20-ML LNO single-layer film measured under the positive and negative magnetic bias of 1 T and temperature of 15 K. The expanded XAS and XMCD spectra around Ni-L_2 absorption edge are depicted in Fig. 6.5. With increasing the thickness of an LNO layer, a sharp peak structure characteristic of Ni^{2+} states gradually attenuate at about 852.5 eV in Ni-L_3 edge and doublet structure changes into single-peak structure in Ni-L_2 edge, which means the evolution of Ni^{3+} states in an LNO layer with increasing n. This is consistent with the results described in Chapter 5: The electron transfer occurs from Mn to Ni and the transferred electron is confined in 1-ML LNO at the interface. It should be noted that the difference of Ni-$L_{2,3}$ XAS spectra between LMO/LNO (2 ML)/LMO in Fig. 6.4 (a) and LNO (1 ML)/LMO in Fig. 5.11 (a) of Chapter 5, although Ni^{2+} states are dominant in the both structures, may come from the difference of measurement temperature and helicity in the incident beam. The former spectrum was measured at 15 K by circularly polarized x-rays, whereas the latter one was obtained at room temperature by a horizontal linearly polarized beam. Figure 6.6 shows the Ni-$L_{2,3}$ XAS spectra of LMO/LNO/LMO trilayer (the same samples in Fig. 6.4) measured at room temperature by a horizontal linearly polarized

x-ray at Beamline MUSASHI (BL-2A) of KEK-PF, in which the very similar XAS spectrum is obtained for LMO/LNO (2 ML)/LMO trilayer to that of LNO (1 ML)/LMO in Fig. 5.11 (a) of Chapter 5.

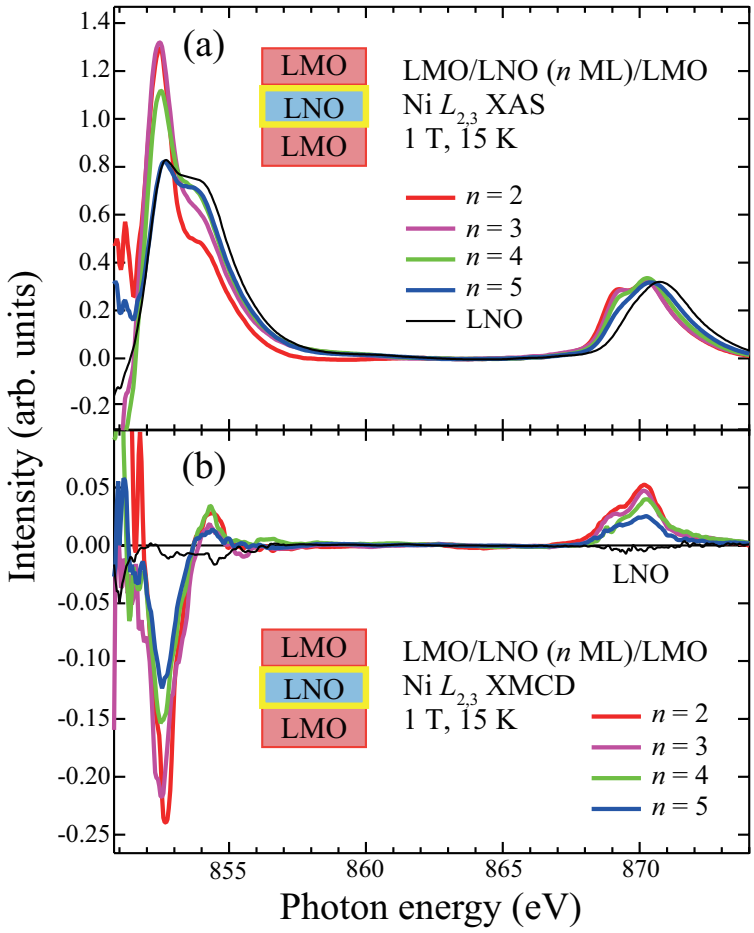

Figure 6.4: (a) Ni-$L_{2,3}$ XAS and (b) Ni-$L_{2,3}$ XMCD spectra of LMO/LNO/LMO trilayers with varying LNO middlelayer thickness n measured together with LNO under the magnetic bias of 1 T and temperature of 15 K. The contribution of the La-M_4 edge has been subtracted from XAS spectra.

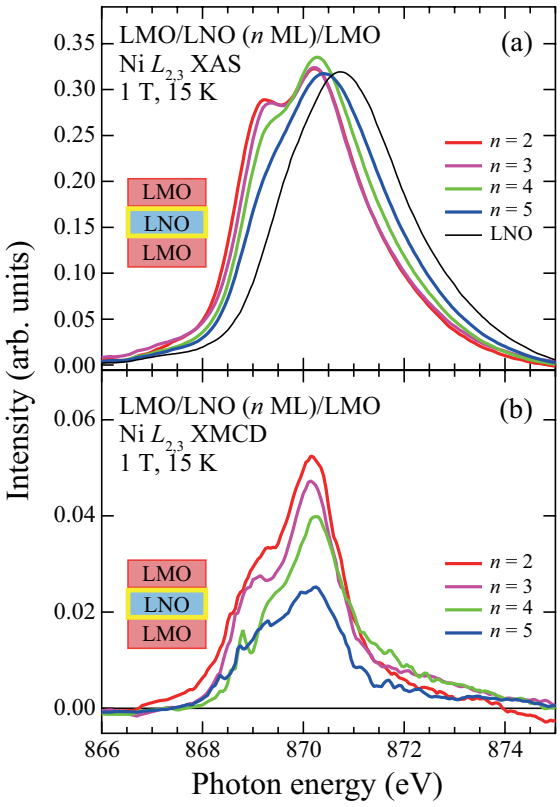

Figure 6.5: Expanded (a) Ni-L_2 XAS and (b) Ni-L_2 XMCD spectra of LMO/LNO/LMO trilayers with varying LNO middlelayer thickness n together with LNO measured under the magnetic bias of 1 T and temperature of 15 K.

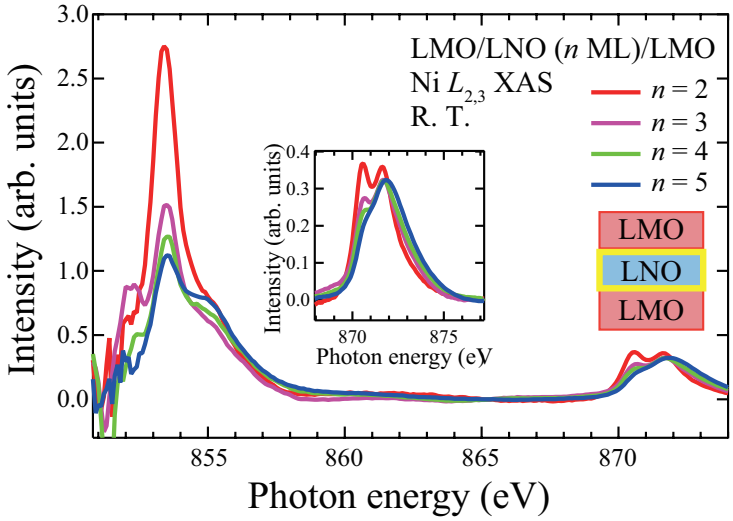

Figure 6.6: Ni-$L_{2,3}$ XAS spectra of LMO/LNO/LMO trilayers with varying LNO middlelayer thickness n measured by a horizontally polarized x-ray at room temperature.

Although no XMCD signal is observed in LNO reflecting its paramagnetic property, XMCD signals are clearly observed for all LMO/LNO/LMO trilayers. Thus, it can be concluded that the magnetization is induced in Ni ions by fabricating the heterojunction to a LMO layer. By comparing XMCD spectra among trilayers of the different LNO thickness, it is found that the intensity of XMCD spectra monotonically decreases with increasing *n*, as summerized in Fig. 6.7. That is, the net spin moments per Ni ion decrease following the increase of an LNO middlelayer thickness. Furthermore, the electronic states of Ni ions contributing to XMCD signals have been investigated. Figure 6.8 shows the normalized Ni-L_2 XMCD spectra by a maximum intensity for a clear display of the spectral shape. Importantly, the spectral shape remains mostly the same within the experimental accuracy for all LMO/LNO/LMO trilayers, which in turn is very similar to a Ni^{2+} XMCD spectrum, observed in LNMO films, as shown in Fig. 4.5 (c) and Fig. 4.6 (d) of Chapter 4 [89]. Considering that Ni^{2+} states exist in the 1-ML LNO at the interface as mentioned in Chapter 5 and the decrease of the net moments with increasing an LNO thickness, it can be demonstrated that magnetizations reside only in Ni^{2+} ions of 1-ML LNO at the hetrointerface. I calculated the effective spin moments by XMCD sum rules [33, 34], as shown in Fig. 6.9. Although it should be noted that the calculated values have large analytical errors due to the strong La M_4-absorption and small Ni $L_{2,3}$-XAS and XMCD signals, the spin moments are much smaller than that of LNMO and spin only values expected from $Ni^{2+}(t_{2g}^6 e_g^2)$ electronic configuration. It may be caused by instability of ferromagnetism in (001)-oriented LMO/LNO/LMO trilayers because magnetic interaction of Ni^{2+}-O-Ni^{2+} is expected to be antiferromagnetic by Kanamori-Goodenough rules while the strong ferromagnetic Ni^{2+}-O-Mn^{4+} superexchange interaction develops for all directions in La_2NiMnO_6 (LNMO).

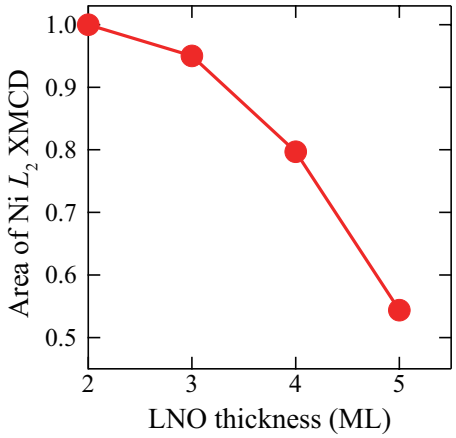

Figure 6.7: Plots of the area intensity ratio of Ni-L_2 XMCD as a function of the LNO middlelayer thickness.

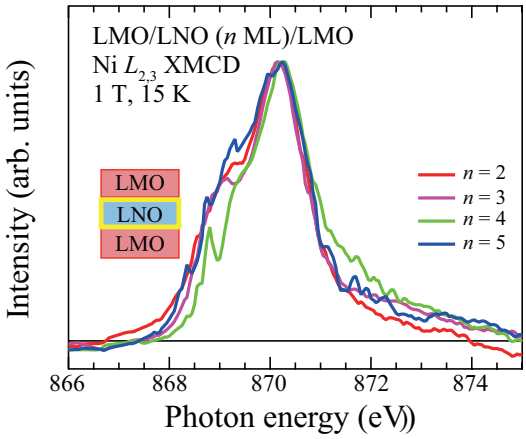

Figure 6.8: Normalized Ni-L_2 XMCD spectra of LMO/LNO/LMO trilayers with varying LNO middlelayer thickness n by a maximum intensity of each spectrum.

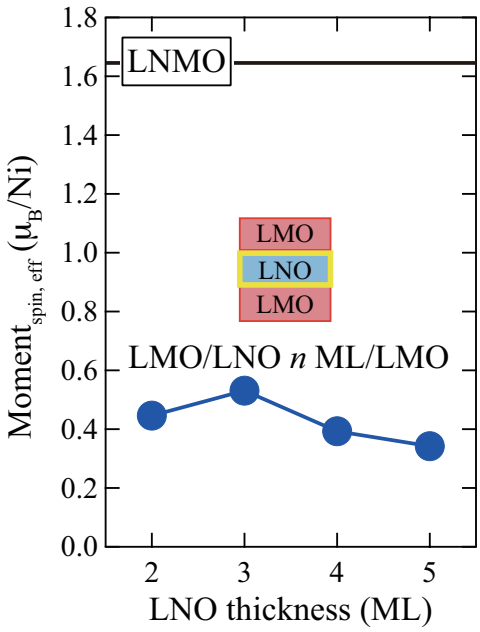

Figure 6.9: Effective spin moments of Ni calculated using sum rules for LMO/LNO/LMO trilayers and LNMO as a function of the LNO middlelayer thickness.

Mn-$L_{2,3}$ XAS and XMCD spectra of the same LMO/LNO/LMO trilayer structures and a 20-ML LMO single-layer film are shown in Figs. 6.10 (a) and (b). In Mn-$L_{2,3}$ XAS spectra of LMO/LNO/LMO trilayers, the main-peak positions locate at slightly higher photon energies and the spectral weights at higher photon energies are larger than that of an LMO single film. This is caused by the increase of the additional Mn^{4+} states due to the charge transfer between LNO and LMO. As for the Mn-$L_{2,3}$ XMCD spectra, XMCD signals are clearly observed for all spectra including an LMO single film. The net magnetization in an LMO single film may come from oxygen excess and/or cation vacancy or strain effects from a substrate. Evolution of an additional shoulder structure around 643.5 eV in the XMCD spectra of LMO/LNO/LMO trilayers compared to that of an LMO single film indicates that Mn^{4+} has a larger contribution to

the magnetism induced in Mn ions of LMO/LNO/LMO trilayers than an LMO single film. The XMCD spectra of LMO/LNO/LMO trilayers are similar in line shape to that of $La_{1-x}Sr_xMnO_3$ [118, 119, 120], as shown in Fig. 6.11 [118], demonstrating that not only Mn^{4+} ions generated by the charge transfer but also Mn^{3+} ions contribute the magnetization. The strong negative signs in the Ni-L_3 and Mn-L_3 XMCD spectra demonstrate that Ni 3*d* and Mn 3*d* spins align parallel to the magnetic field. Furthermore, the same sign of XMCD signals between Ni-$L_{2,3}$ and Mn-$L_{2,3}$ edge is an evidence that the Ni spins and Mn spins align ferromagnetically.

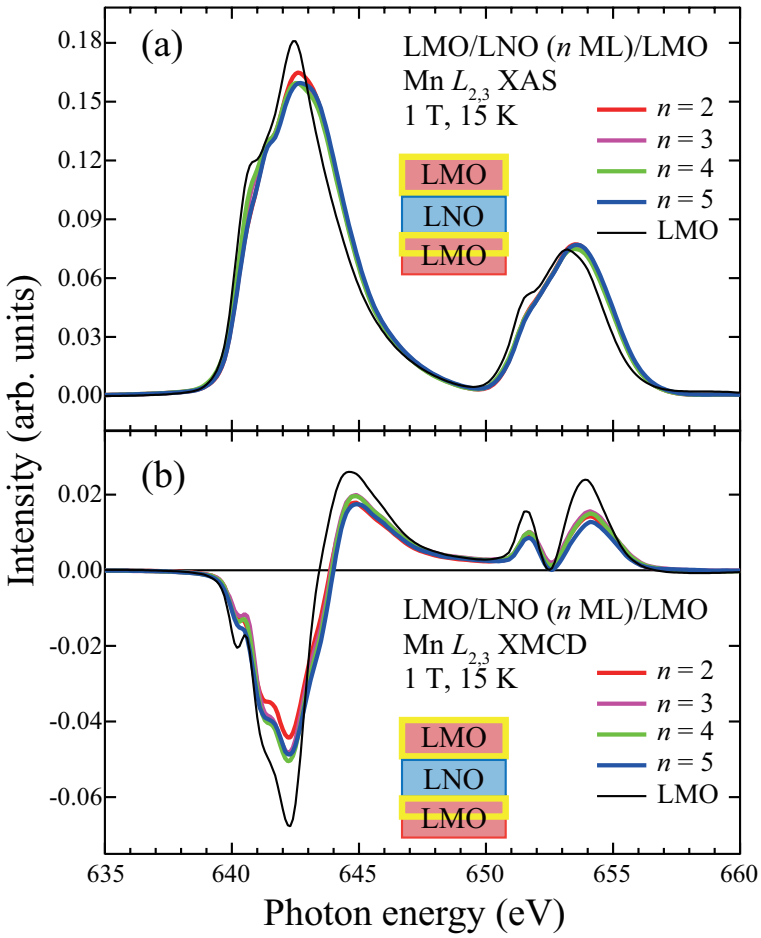

Figure 6.10: (a) Mn-$L_{2,3}$ XAS and (b) Mn-$L_{2,3}$ XMCD spectra of LMO/LNO/LMO trilayers with varying LNO middlelayer thickness *n* together with LMO measured under the magnetic bias of

1 T and temperature of 15 K.

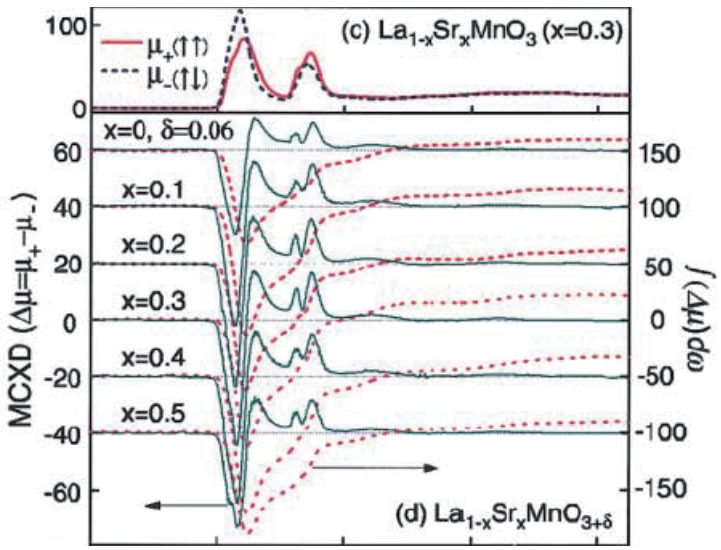

Figure 6.11: Mn-$L_{2,3}$ XMCD spectra of of $La_{1-x}Sr_xMnO_3$ under the magnetic bias of 2 T and temperature of 20 K [118].

The other structures, LNO/LMO/LNO trilayers, have also been investigated by XAS and XMCD measurements. I have selected LMO middlelayers with three different thicknesses based on the spatial distribution of the transferred charge in an LMO layer, which is 3-4 ML from the interface. First is a 2-ML LMO layer, which consists of the interfaces toward LNO alone. Second is a 6-ML LMO layer, where all regions are related to the charge transfer. Last is a 12-ML LMO layer, which has a layer with thickness of 4-6 ML not related to the charge transfer in the middle. Figures 6.12 (a) and (b) show Mn-$L_{2,3}$ XAS and XMCD spectra of LNO/LMO/LNO trilayer structures and a 20-ML LMO single-layer film as a reference. Mn-$L_{2,3}$ XAS spectrum of m = 2 resembles to a typical Mn^{4+} spectrum and the position of the most

prominent peak of XAS shifts towards lower photon energies with increasing the thickness of an LMO middlelayer, indicating the Mn^{3+} states evolves in the LMO layer following the increase of the thickness not related to the charge transfer. As for Mn-$L_{2,3}$ XMCD spectra, the spectrum of the trilayer of m = 2 is similar to a Mn^{4+} XMCD spectrum, as shown in Fig. 4.5 (d) and Fig. 4.6 (c) of Chapter 4 [89]. This result demonstrates that Mn^{4+} spins, which come from the charge transfer, dominantly contribute the magnetization in the trilayer of 2-ML LMO. On the other hand, the spectral shapes and the intensities of the trilayers of 6-ML LMO and 12-ML LMO are significantly different from 2-ML LMO and rather close to an LMO single layer. In addition, compared to the XMCD spectrum of LMO single film, they have an additional structure derived from Mn^{4+} state around 635.6 eV. This result indicated that Mn spins reside in both Mn^{3+} and Mn^{4+} ions and the magnetized region is not constricted in 1-ML LMO at the interface but spreads through some monolayers from the interface, which is contrast to the result of the LNO side. The effective spin moments of Mn are calculated by XMCD sum rules [33, 34], as shown in Fig. 6.13. The net magnetization of Mn ions in trilayer of 2-ML LMO is significantly smaller than 6-ML LMO and 12-ML LMO, even if it is assumed that the Mn^{4+} (S = 3/2) states are dominant in 2-ML LMO, while 6-ML LMO and 12-ML LMO have both Mn^{4+} (S = 3/2) and Mn^{3+}(S = 2) states. One possible reason is that the magnetic field of 1 T is not high enough to saturate the magnetization of Mn^{4+} spins at the interface. Other reason is that ferromagnetism in 2-ML LMO layer is less stable than in thicker LMO due to the antiferromagnetic superexchange interaction between Mn^{4+}-O-Mn^{4+}, whereas ferromagnetic doubleexchange interactions derived from not only Mn^{4+} but also Mn^{3+} resulting from the charge spreading more stabilized ferromagnetism in an LMO layer with the thickness of 6-ML and 12-ML.

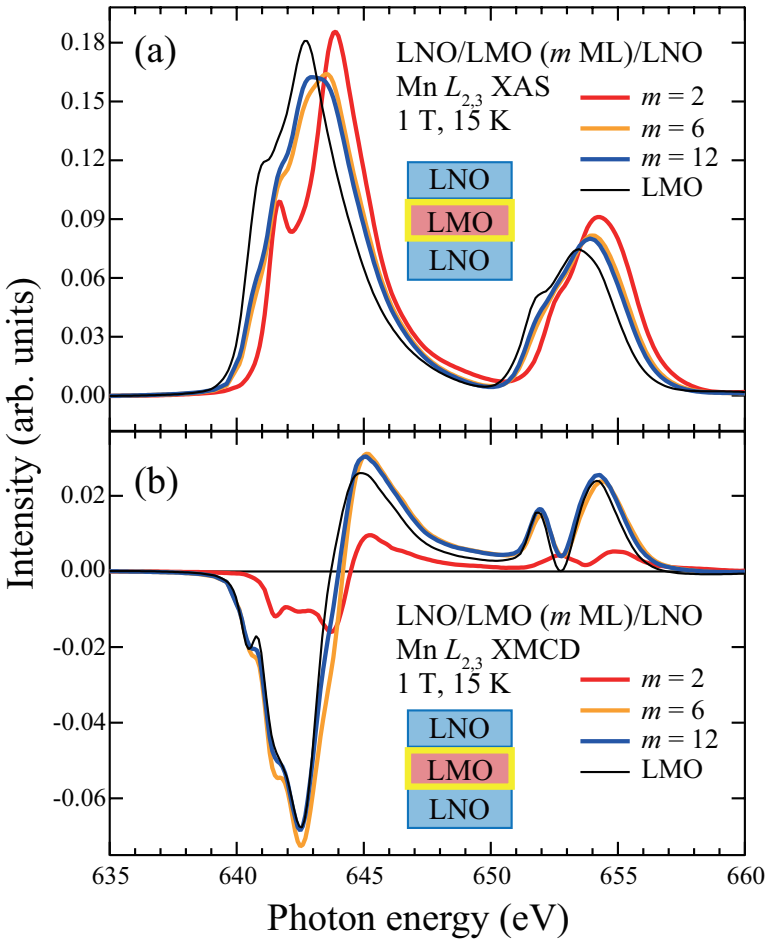

Figure 6.12: (a) Mn-$L_{2,3}$ XAS and (b) Mn-$L_{2,3}$ XMCD spectra of LNO/LMO/LMO trilayers with varying LMO middlelayer thickness *m* together with LMO measured under the magnetic bias of 1 T and temperature of 15 K.

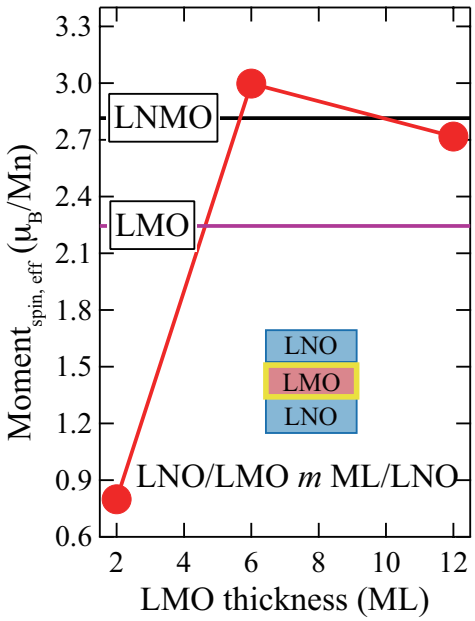

Figure 6.13: Effective spin moments of Mn calculated using sum rules for LNO/LMO/LNO trilayers, LMO and LNMO as a function of the LMO middlelayer thickness.

Figures 6.14 (a) and (b) show Ni-$L_{2,3}$ XAS and XMCD spectra of the same LNO/LMO/LNO trilayer structures and a 20-ML LNO single-layer film. XAS spectra of all trilayers is closer to Ni^{3+} XAS spectrum than Ni^{2+} one, which is consistent with the result that the Ni^{2+} states generated by the charge transfer is constricted in 1-ML LNO at the interface. XMCD signals are observed for all LNO/LMO/LNO trilayers, although their intensities are weak. Similar to the case of LMO/LNO/LMO trilayers, it can be concluded that spins residing in Ni and Mn ions of LNO/LMO/LNO trilayers couple ferromagnetically because both Ni-$L_{2,3}$ and Mn-$L_{2,3}$ edge show the same sign of XMCD signals.

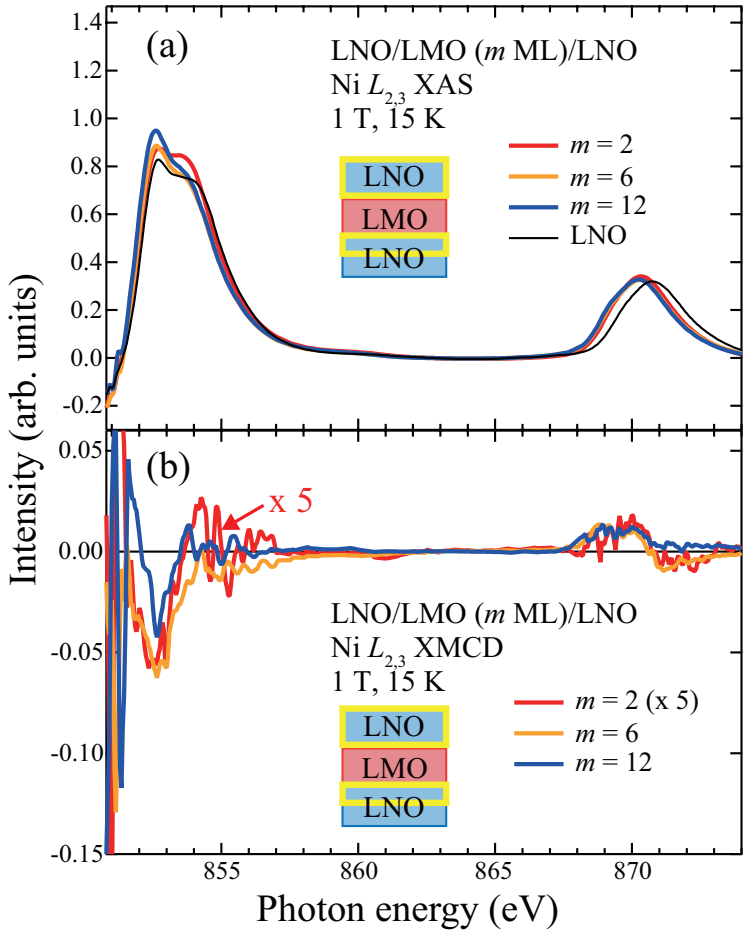

Figure 6.14: (a) Ni-$L_{2,3}$ XAS and (b) Ni-$L_{2,3}$ XMCD spectra of LNO/LMO/LMO trilayers with varying LMO middlelayer thickness *m* together with LNO measured under the magnetic bias of 1 T and temperature of 15 K. Ni-$L_{2,3}$ XMCD spectrum of LNO/2-ML LMO/LMO trilayer is amplified by a factor of five.

Based on the spatial distribution of the transferred charge mentioned in Chapter 5, which is 1 ML for LNO and 3-4 ML for LMO, it is considered that the formal valence of Ni ions in the 1-ML LNO at the interface is 2+ and Mn^{4+} states are dominant in the 1-ML LMO at the interface, although there still exist minor Mn^{3+} states. Let me consider the case that charge transfer occurs between 1-ML LNO and 1-ML LMO, resulting in the existence only Ni^{2+} and

Mn^{4+} ions at the interface. Based on the superexchange interaction, in the (001)-oriented LNO/LMO heterointerface, the spins of Mn and Ni ions in the out-of-plane $Ni^{2+}(d^8)$-O-$Mn^{4+}(d^3)$ bonds that are across the interface can couple ferromagnetically, as in $La_2Ni^{2+}Mn^{4+}O_6$ (T_C ~ 280 K), while those in in-plane $Ni^{2+}(d^8)$-O-$Ni^{2+}(d^8)$ and $Mn^{4+}(d^3)$-O-$Mn^{4+}(d^3)$ bonds couple antiferromagnetically, as in $Ni^{2+}O$ (T_N ~ 525 K), $SrMn^{4+}O_3$ (T_N ~ 260 K), and $CaMn^{4+}O_3$ (T_N ~ 130 K). As a result, net magnetization residing in Ni and Mn ions are expected to become zero at the interface, as shown in Fig. 6.15(a). However, in this study, I have clearly observed net magnetic moments in both Ni and Mn ions of (001)-oriented LNO/LMO trilayers by XMCD measurements. There is a possible explanation for the observed interfacial ferromagnetism. In the LMO layer around the interface, Mn^{4+} state is dominant but small amounts of Mn^{3+} ions also exist due to the 3-4 ML charge spreading, resulting in the ferromagnetism observed in slightly electron-doped $CaMn^{4+}O_3$ [79]. Then, if a $Ni^{2+}(d^8)$-O-$Mn^{4+}(d^3)$ ferromagnetic superexchange interaction through the interface is stronger than $Ni^{2+}(d^8)$-O-$Ni^{2+}(d^8)$ antiferromagnetic superexchange interaction in-plane of an LNO layer, one can obtain net magnetizations coupled ferromagnetically in both Ni and Mn ions, as shown in Fig. 6.15(b). It plays an important role for interfacial ferromagnetism at the heterointerface between LNO and LMO that the transferred charges are not confined in 1 ML at the interface but spreads through 3-4 ML in an LMO layer and resultant Mn^{3+} states.

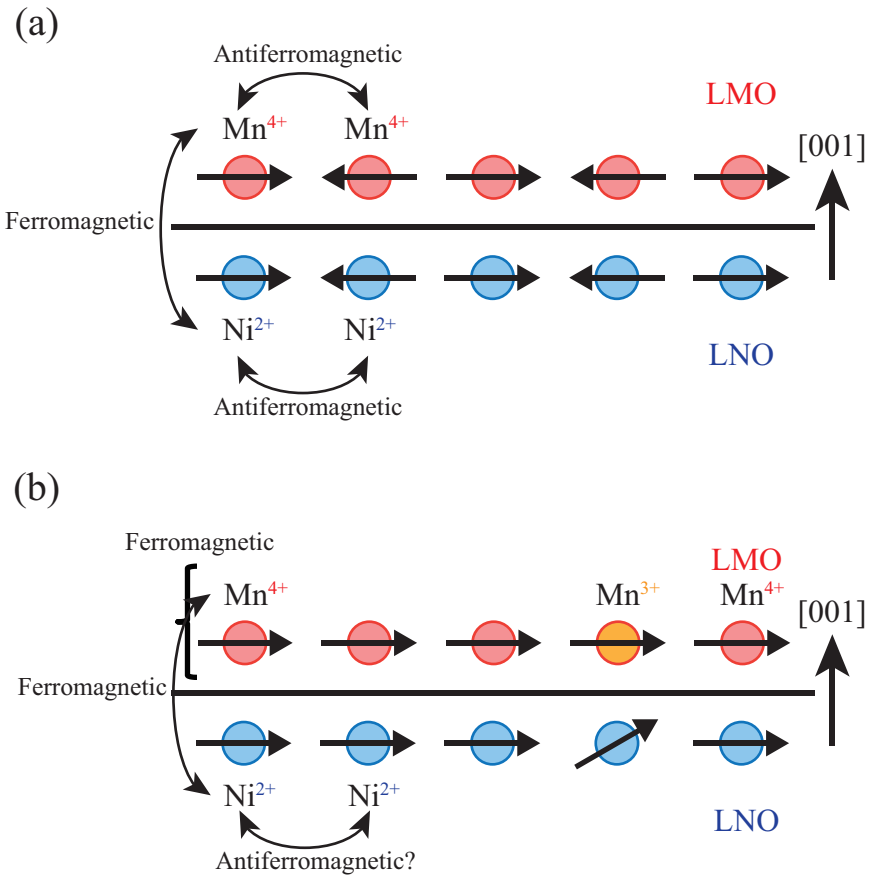

Figure 6.15: A schematic image of the magnetic structure expected in the cases that (a) the transferred charges are confined in both 1-ML LNO and LMO at the heterointerface and (b) the charges spread through some monolayers in LMO.

6.4 Conclusion

The interfacial ferromagnetism of the LNO/LMO heterostructures has been studied by XMCD measurements. XMCD signals were clearly observed in Ni-$L_{2,3}$ XMCD spectra of trilayer structures, while no XMCD signal was observed for a paramagnetic LNO single film, indicating that the magnetizations in Ni ions are induced by fabricating the junction between

LNO and LMO. Systematical analysis of a thickness series of the XMCD spectra for LMO/LNO/LMO trilayers reveals that the net spins reside in Ni^{2+} ions at 1-ML LNO at the interface, which come from the charge transfer between LNO and LMO. On the other hand, both Mn^{3+} and Mn^{4+} states contribute the magnetization in an LMO layer and the magnetized region spreads though some monolayers from the heterointerface. The same sign of Ni-$L_{2,3}$ and Mn-$L_{2,3}$ XMCD signals indicates that the net spins residing in Ni^{2+} and Mn^{4+} ions at the interface align ferromagnetically. Thus, the charge transfer between Ni and Mn ions plays an important role for the interfacial ferromagnetism in LNO/LMO hetrostructures.

Chapter 7
Determination of band diagram for *p-n* junction between Mott insulator $LaMnO_3$ and band insulator Nb:$SrTiO_3$

7.1 Introduction

7.1.1 Previous studies of novel magnetic properties of $LaMnO_3$-$SrTiO_3$ superlattices

As mentioned in Chapter 5, $LaMnO_3$ (LMO) is a Mott insulator exhibiting A-type antiferromagnetic spin order at low temperature in stoichiometric bulk phase, while LMO thin film often shows ferromagnetism due to oxygen excess and/or cation vacancy or strain effects. The heterostructures between LMO and band insulator $SrTiO_3$ (STO) exhibit interesting aspects reflecting the strongly correlated nature of LMO. Recently, Choi *et al*., have reported that LMO-STO superlattices exhibit weak ferromagnetic properties although LMO is an antiferromagnetic and STO is a non-magnetic, as shown in Fig. 7.1 [24]. Garcia-Barriocanal *et al*. have reported that LMO-STO superlattices exhibit ferromagnetic properties different from an LMO film and they can be modulated with change of the periods of superlattices, as depicted in Fig. 7.2 [26, 121]. These ferromagnetic modulations were also reported although there were some inconsistencies about the relationships between the superlattice period and enhancement/suppression of ferromagnetism [24, 122]. The emergence of interfacial ferromagnetism with high-mobility carriers has also been predicted by a recent first-principle

calculation [123]. Furthermore, the occurrence of a certain charge leakage process, probably due to the polar discontinuity at the interface and the strain effects, has been suggested by recent scanning transmission electron microscopy (TEM) studies [26, 124, 125]. However, the variations of Mn and Ti valences are very small, which may not be enough to cause the observed large modifications of magnetic properties. And thus, the origin of these novel magnetic properties remains unclear at the moment.

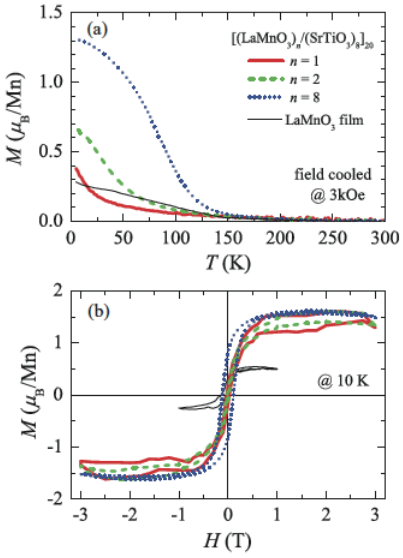

Figure 7.1: (a) Temperature dependence of magnetization and (b) Magnetic field dependence of magnetization of $[(LaMnO_3)_n/(SrTiO_3)_8]_{20}$ superlattices [24].

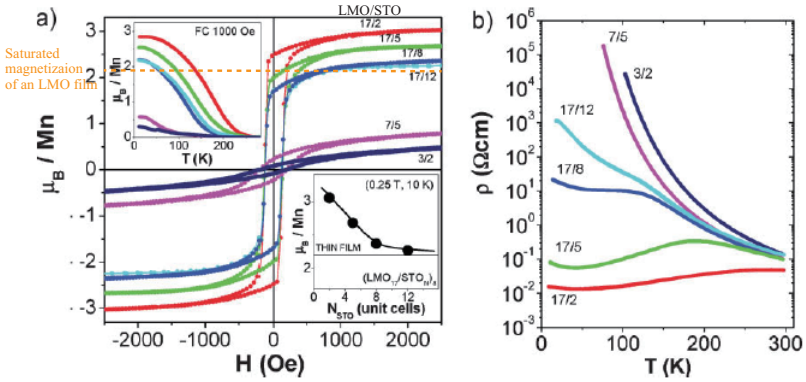

Figure 7.2: (a) Magnetic properties and (b) Transport properties of $[(LaMnO_3)_M/(SrTiO_3)_N]_8$ superlattices [26].

7.1.2 Previous studies of *p-n* junction between $LaMnO_3$ and $SrTiO_3$

In contrast to the exotic ferromagnetic properties observed in LMO-STO superlattices, LMO/STO heterointerfaces have been studied as a *p-n* junction. The *p-n* junction of conventional semiconductors is one of the most fundamental elements of electronic devices, which has made a great contribution to the development of modern information technology. Thus far, various "*p-n* junctions" based on perovskite oxides have been evaluated for their characteristics [126, 127]. Among them, the *p-n* junction composed of the "*p*-type" Mott insulator LMO [81] and the *n*-type oxide semiconductor STO [128] has been intensively studied as a prototypical example [129, 113]. Despite the Mott insulating ground states in LMO [2], it has been reported that clear rectification properties of *p-n* junctions are obtained in LMO/Nb:STO heterointerfaces, as depicted in Figs. 7.3 and 7.4 [129, 113]. These results suggest that the *p-n* junction characteristics observed in LMO/Nb:STO heterostructures are dominated by the "practical" carrier concentration in LMO and designed by the analogy of conventional semiconductor technology: the carrier density estimated from thermodynamic measurements, such as a photocurrent measurement (4×10^{19} cm^{-3} [113]), directly corresponds to the practical carrier concentration N_p in LMO, while one hole per unit cell is expected from the chemical formula (1.7×10^{22} cm^{-3}).

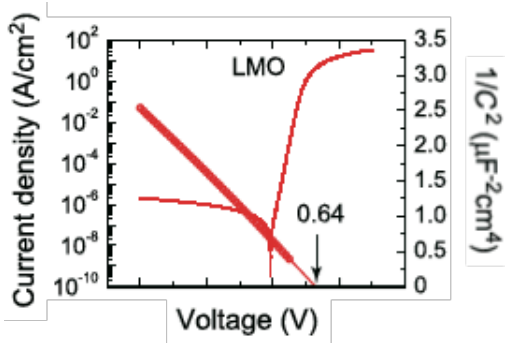

Figure 7.3: Transport properties of $LaMnO_3$/Nb:$SrTiO_3$ heterojunction [129].

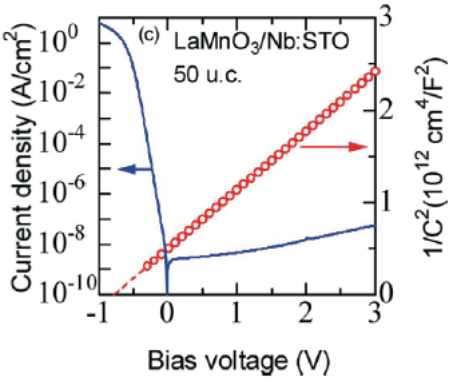

Figure 7.4: Transport properties of $LaMnO_3$/$Nb:SrTiO_3$ heterojunction [113].

7.1.3 Purpose of this study

As mentioned in the introduction, LMO/STO heterointerfaces are studied in the two contrast points of view: One is derived from Mott insulating character of LMO, the other is an analogy of *p-n* junction of conventional semiconductors. In this study, at first, in order to clarify the relationships between the charge transfer and novel magnetic properties, I investigated whether the charge transfer occurs or not between LMO and STO using x-ray absorption spectroscopy (XAS). Furthermore, in order to obtain the information of the electronic structure at the heterointerface, I determined the band diagram of LMO/Nb:STO *p-n* junctions and its carrier concentration dependence by using x-ray photoemission spectroscopy (XPS). LMO/Nb:STO heterojunctions were fabricated by epitaxial growth of LMO films on Nb:STO substrates. I obtained the amount of band bending on Nb:STO side, which is correspond to the built-in potentials in Nb:STO, by evaluating the core-level peak shifts of Nb:STO following the deposition of LMO. By studying the variation of built-in potentials in Nb:STO side with the change of carrier concentration of Nb:STO, I calculated the band diagram of LMO/Nb:STO heterojuction.

7.2 Experiments

Epitaxial LMO films with various thicknesses were grown on 0.1 at. % and 1.0 at. % Nb-doped (100) STO single-crystal substrates by laser molecular beam epitaxy (Laser MBE). A Nd-doped yttrium-aluminum-garnet laser in the frequency-triplet mode (λ = 355 nm) at a repetition rate of 1 Hz was used for ablation. A sintered LMO pellet was used as the target. The TiO_2-terminated Nb:STO substrates were annealed at 1050 °C under an oxygen pressure of 1×10^{-7} Torr to obtain atomically flat and chemically clean surfaces. During the LMO deposition, the substrate was kept at the temperature of 800 °C and the oxygen pressure was maintained at 1×10^{-3} Torr. The thickness of the LMO films was precisely controlled by monitoring the intensity oscillation of the specular spot with reflection high-energy electron diffraction (RHEED) during the growth. After the LMO film growth, the samples were transported to an XPS chamber without air exposure using a home-built "vacuum suitcase". XPS measurements were performed using a VG-Scienta R3000 analyzer with a monochromatized Al Kα x-ray source ($h\nu$ = 1486.6 eV). Binding energies were calibrated by measuring a gold film electrically connected to the samples. All spectra were acquired at room temperature with a total energy resolution of 500 meV.

XAS measurements were performed at BL-16A of KEK-PF. The magnetic field of about 1 T was applied 30 ° from the sample surface and parallel to the incident beam. The direction of the magnetic field was field, while the helicity of the incident beam was switched in 10 Hz. The XAS spectra were taken in a total-electron-yield mode at 15 K.

The surface morphology of the measured films was analyzed by *ex-situ* atomic force microscopy in air. The crystal structure was characterized by cross-sectional TEM and synchrotron-based x-ray diffraction (SR-XRD) measurements performed at the BL-4C beamline of KEK-PF.

7.3 Results and Discussion

7.3.1 Growth and characterization of $LaMnO_3$ films

Figure 7.5 shows a RHEED pattern after 100-monolayer (ML) LMO deposition and an intensity oscillation of the specular spot of RHEED pattern during the 5-ML and 10-ML LMO deposition. Clear streak patterns indicate that single crystal and flat surface is obtained. The period of RHEED oscillation corresponds to the 1-ML LMO deposition and strict control of film deposition with intentional thickness was attained. In order to characterize the surface morphology of a film, AFM measurements were carried out. As shown in Fig. 7.6, a 100-ML LMO film has an atomically flat surface with step-and-terrace structures reflecting the surface of Nb:STO substrate, indicating that not only the surface but also the buried interfaces were atomically flat. Figure 7.7 depicts a reciprocal space mapping around (114) reflection and $2\theta/\omega$ scan around (002) of 100-ML LMO film on an Nb:STO substrate by SR-XRD measurements, where the reciprocal-space coordinates correspond to the cubic Nb:STO substrate. The (114) diffraction peak of LMO film has the same H value with that of Nb:STO substrate, indicating that an LMO film grows with keeping the in-plane crystal coherency to a Nb:STO substrate at least up to 100-ML thickness. The crystal structure of an LMO film is modified to tetragonal with suppression in a lateral plane to match a Nb:STO substrate and resultant expansion along a vertical direction. The coherent growth of LMO on Nb:STO was also confirmed by the high-angle annular dark-field scanning TEM (HAADF-STEM). The lattice parameters estimated by a (002) diffraction peak were 3.95 Å, which is approximately the same as those stated in a previous report [19].

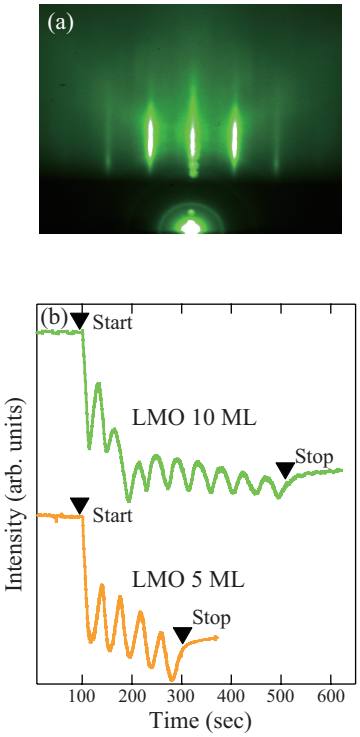

Figure 7.5: (a) RHEED pattern of 100-ML LMO film. (b) Intensity oscillations of the specular spot of RHEED pattern during the 5-ML and 10-ML LMO growth.

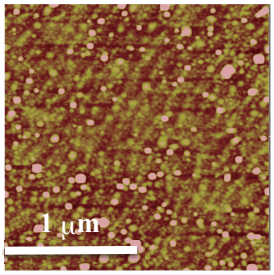

Figure 7.6: AFM image of 100-ML LMO film.

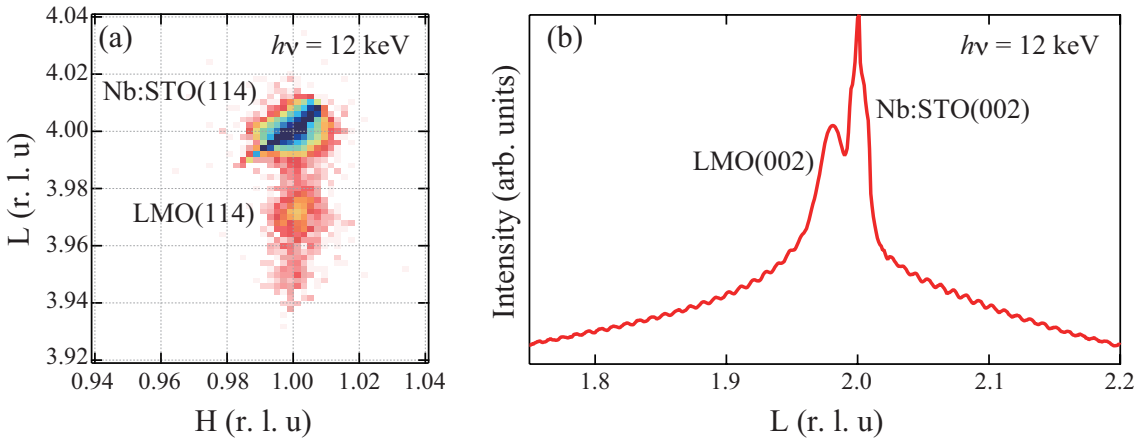

Figure 7.7: (a) A reciprocal space mapping around (114) reflection and (b) $2\theta/\omega$ scan around (002) reflection of 100-ML LMO film.

7.3.2 Confirmation of chemical abruptness at the interface

I provide experimental evidence for the formation of a chemically abrupt interface between the LMO and STO. Figure 7.8 (a) shows the Sr 3*d* core-level spectra of the buried STO for a junction between an LMO film and a 0.1 at. % Nb-doped STO substrate, where the top layer is that of the LMO with variable thickness. The intensity of the core level rapidly attenuates with increasing the LMO overlayer thickness and completely disappears at 30 ML. Almost the same spectral attenuation is observed in the Ti 2*p* core-level spectra (Fig. 7.8 (b)), as well as the other junction between LMO and 1.0 at. % Nb-doped STO, as shown in Fig. 7.9. In order to evaluate the abruptness at the interface, the intensities of the Sr 3*d* and Ti 2*p* core levels are plotted in Fig. 7.10 for both junctions as a function of the LMO overlayer thickness. The exponential reduction in core-level intensity with increasing the LMO overlayer thickness indicates the formation of a chemically abrupt interface between the LMO film and the Nb:STO subtrate. This formation is further confirmed by HAADF-STEM image shown in Fig. 7.11.

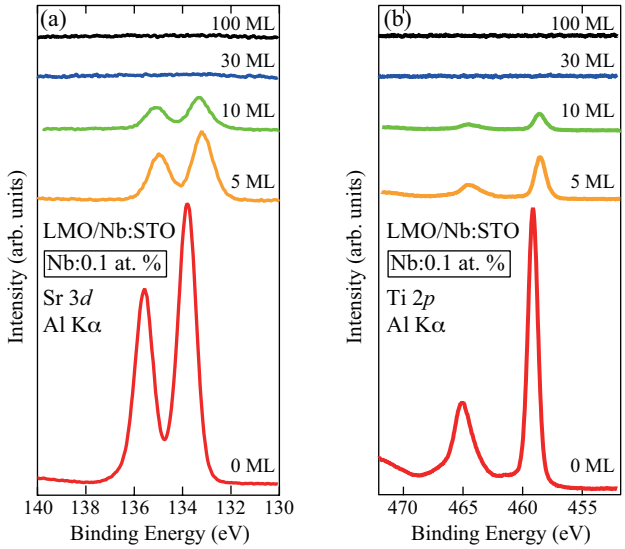

Figure 7.8: (a) Sr 3*d* core-level spectra and (b) Ti 2*p* core-level spectra for 0.1 at. % Nb-doped STO covered by LMO overlayers.

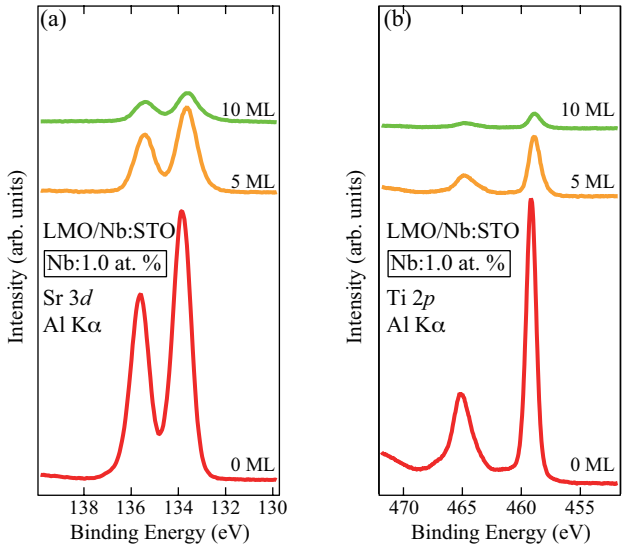

Figure 7.9: (a) Sr 3*d* core-level spectra and (b) Ti 2*p* core-level spectra for 1.0 at. % Nb-doped STO covered by LMO overlayers

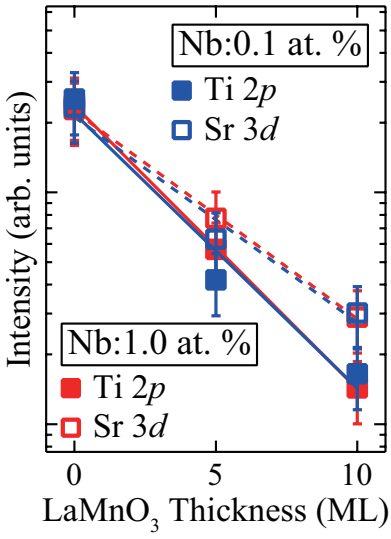

Figure 7.10: Plot of the intensity of the Sr 3*d* and Ti 2*p* core levels as a function of LMO overlayer thickness for 0.1 at. % and 1.0 at. % Nb-doped STO substrates. The dashed and solid lines represent the fitted results by photoelectron attenuation functions for the Sr 3*d* and Ti 2*p* core levels, respectively.

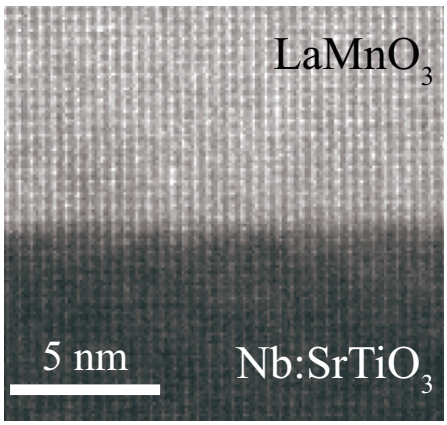

Figure 7.11: HAADF-STEM image at the interface of LMO and 0.1 at. % Nb-doped STO.

7.3.3 Verification of the charge transfer

In order to investigate the charge transfer between LMO and STO, Ti-$L_{2,3}$ (Ti 2*p* → 3*d* excitation) XAS measurements were performed. Figure 7.12 shows Ti-$L_{2,3}$ XAS spectra of a 0.1 at. % Nb-doped STO substrate and a 5-ML LMO/Nb:STO heterostructure measured under magnetic field of 1T and temperature of 15 K. These spectra were obtained as an average of XAS spectra taken by an incident beam of right-handed helicity and left-handed one. The peak around 458.5-462.7 eV is called Ti-L_3 XAS, and that around 462.7-470 eV is called Ti-L_2 XAS. The spectral shapes and peak positions of obtained XAS spectra of a substrate and a heterostructure are quite similar to each other and reported Ti^{4+} XAS spectra, as shown in Figs. 7.13 and 7.14 [130, 131], implying that the valences of Ti do not change between a Nb:STO substrate and an LMO/Nb:STO heterostructure. This result indicates that the charge transfer does not occur between Ti and Mn ions, which is consistent with the result expected from the redox potential as mentioned in Chapter 1 [29, 28]. Furthermore, the difference of chemical potentials between the LMO and Nb:STO at the interface does not support the occurrence of the charge transfer. Figure 7.15 illustrates the electronic structures predicted at the LMO/Nb:STO interface: The valence bands of LMO and Nb:STO are realigned with the same energy position of each O 2*p* states because LMO and Nb:STO share the same oxygen ion at the interface, as is the case in the LNO/LMO heterojunction. In this alignment, because the unoccupied Ti 3*d* state is located at the higher energy position than the occupied Mn 3*d* state, it may be impossible to occur the electron transfer from Mn to Ti ions.

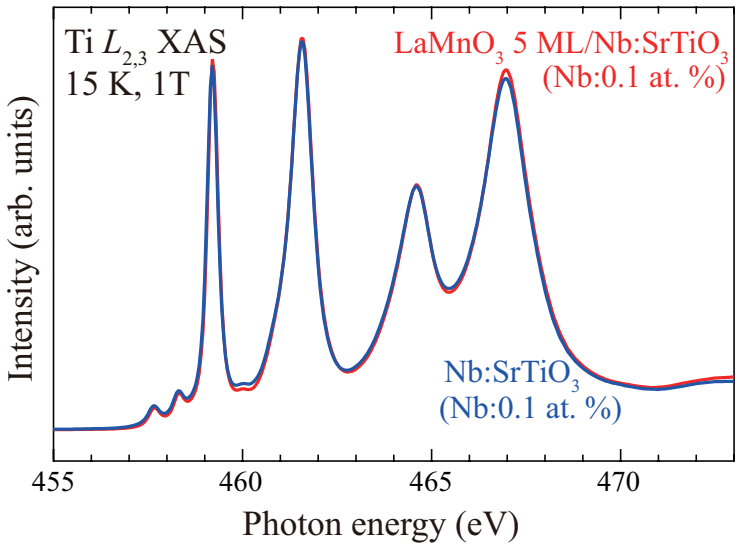

Figure 7.12: Ti-$L_{2,3}$ XAS spectra of a 0.1 at. % Nb-doped STO substrate and a 5-ML LMO/Nb:STO heterostructure.

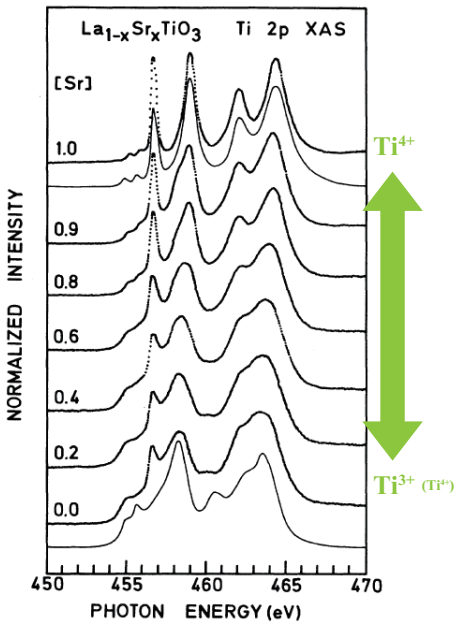

Figure 7.13: Ti-$L_{2,3}$ XAS spectra of $La_{1-x}Sr_xTiO_3$ [130].

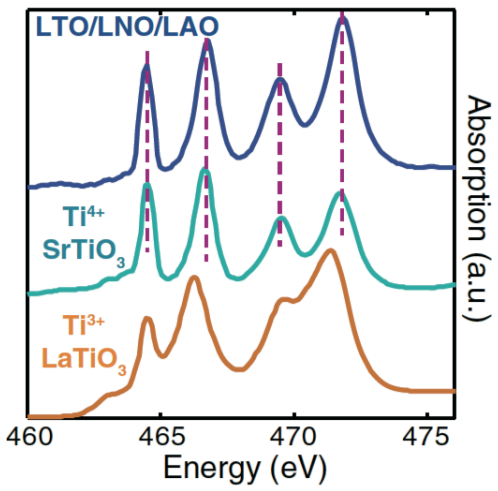

Figure 7.14: Ti-$L_{2,3}$ XAS spectra of $SrTi^{4+}O_3$ and $LaTi^{3+}O_3$ [131].

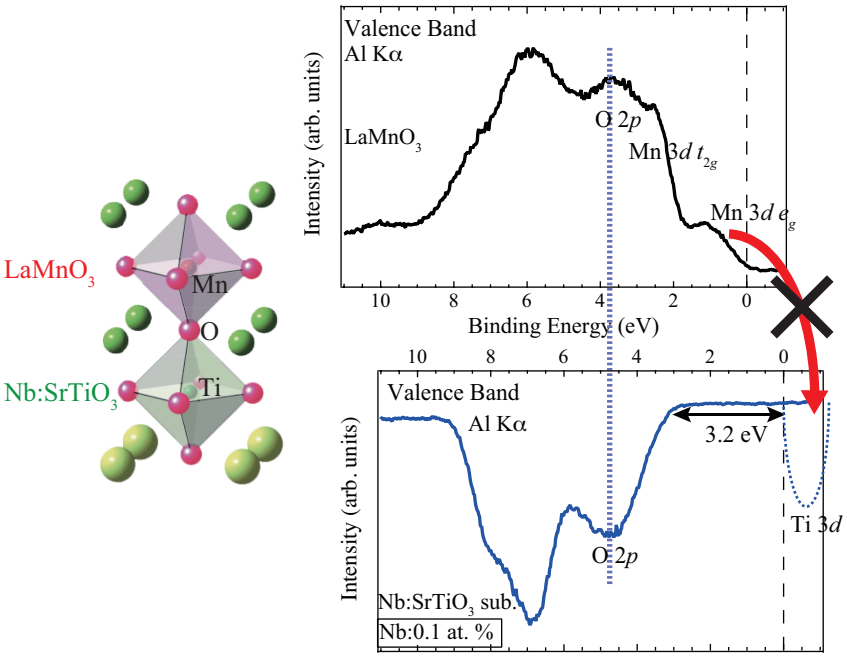

Figure 7.15: The electronic structures predicted at the LMO/Nb:STO interface. Based on the difference of the chemical potentials between LMO and Nb:STO, the charge transfer are not expected to occur.

Thus, other mechanisms than the charge transfer between B-site ions may induce the novel magnetic properties reported in LMO-STO superlattices. One possibility is that the MnO_6 octahedral rotation in an LMO layer caused by the strain from an STO is linked to the modification of ferromagnetism in LMO-STO superlattices, as recently reported by Zhai *et al*. [132]. The bond angle of Mn-O-Mn is changed with following MnO_6 octahedral rotation, resulting that the double exchange interaction in LMO is strengthened or weakened and resultant modification of ferromagnetism.

7.3.4 Valence band spectra

Figure 7.16 shows the valence band spectra for the constituent oxides: a thick LMO film (100 ML) and Nb:STO substrates with different Nb concentrations. An extrapolation of the linear portion of the leading edge to the energy axis (the background level) yields a valence band maximum (VBM) for the constituent oxides. The values of VBM were estimated to be -0.02±0.06 eV for the 100-ML LMO films, 3.13±0.05 eV for the 0.1 at. % Nb-doped STO substrates, and 3.20±0.05 eV for the 1.0 at. % Nb-doped STO substrates. Taking into account the band gap of 1.1 eV for LMO [95], the obtained value of VBM suggests that the LMO film can be considered to be a degenerate *p*-type semiconductor without a surface depletion layer. The comparison of the VBM value with those obtained by previous studies, where the VBM of LMO was located at about 0.3-0.4 eV [133, 92], implies that the present LMO films contain much higher carrier concentrations. The difference may be caused by larger amount of oxygen excess and/or cation deficiency in the present LMO film. The *p*-type degenerate semiconductive nature of the present LMO film enables me to determine the band lineup more accurately owing to the formation of a flatband at the surface of the LMO film. On the other hand, the VBM of Nb:STO shows almost the same value of ~3.2 eV between the two substrates, irrespective of their difference in donor concentration. This result is consistent with the fact that STO with a

Nb-doping level higher than 0.1 at. % is an *n*-type degenerate semiconductor [134] because the band gap of STO is 3.2±0.1 eV at room temperature [135].

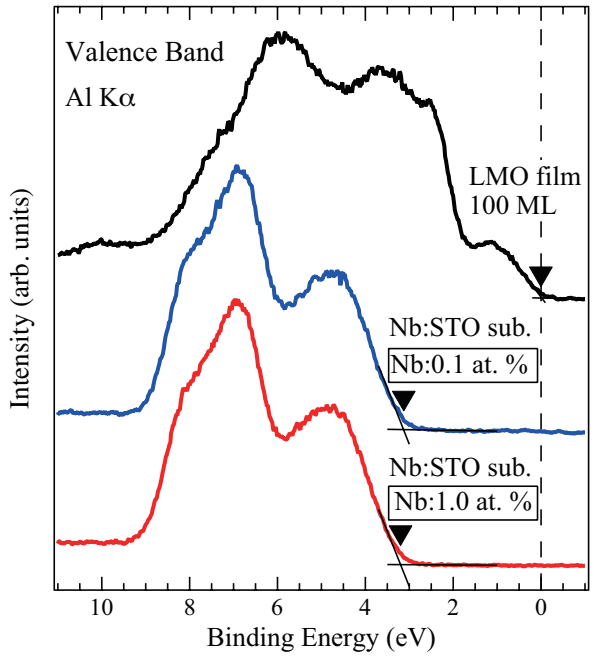

Figure 7.16: Valence-band photoemission spectra of a 100-ML LMO film, a 0.1 at. % Nb-doped STO substrate, and a 1.0 at. % Nb-doped STO substrate. The triangles indicate the VBM of the respective surfaces, estimated from the intersection point between the extrapolation of the linear portion of the leading edge and the background signal level.

7.3.5 Peak shift of core level spectra

In order to determine the built-in potential in the Nb:STO side directly, I replotted the Ti 2*p* and Sr 3*d* core-level spectra. Figures 7.17 (a) and (b) show the Ti 2*p* core-level spectra of the buried Nb:STO layer for an LMO/Nb:STO junction with a donor concentration of 0.1 at. % and 1.0 at. %, respectively. The spectra are normalized by the maximum intensities of the

peaks for a clearer display of the peak shift. For both junctions, a peak shift toward lower binding energies is clearly observed with increasing overlayer LMO thickness and it seems to be saturated at 5-ML LMO deposition. Owing to the short electron escape depth of a few nm in the XPS measurement, the obtained energy shifts of the Ti 2*p* core-level peaks predominantly reflect the potentials in the thin interface region on the Nb:STO side only. It should be noted that almost the same energy shifts were observed in the Sr 3*d* core-level peaks, indicating that the shifts were caused by the band bending of Nb:STO at the interface with LMO: The energy shifts of core-level peaks of Nb:STO to a lower binding energy mean the energy bands of Nb:STO bend to a lower binding energy at the interface with LMO. In other words, by determining the core-level peak shifts of Nb:STO following the deposition of LMO, it is possible to obtain the amount of band bending on the Nb:STO side experimentally. The energy shifts of the Ti 2*p* and Sr 3*d* core-level peaks are summarized in Fig. 7.17 (c). Considering their saturation levels, the energy shifts can be estimated to be 0.55±0.05 eV for the 0.1 at. % and 0.25±0.05 eV for the 1.0 at. % Nb concentration. Since a flatband is formed at the surface of Nb:STO [134], these shifts directly correspond to the built-in potentials in Nb:STO at the LMO/Nb:STO junctions.

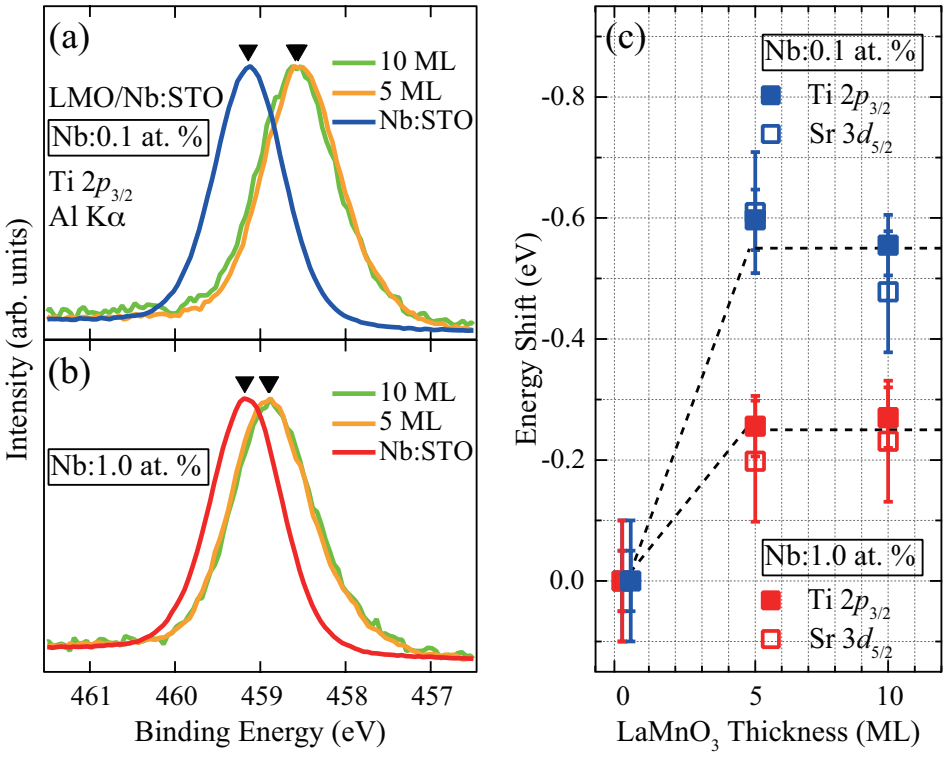

Figure 7.17: Shifts of the core level for Nb:STO. Ti 2*p* core-level spectra of (a) 0.1 at. % and (b) 1.0 at. % Nb-doped STO covered by LMO films with various thicknesses. (c) Plot of the energy shifts of the Ti-2*p* and Sr-3*d* core-level peaks as a function of LMO overlayer thickness. The dashed lines are guides for the eyes.

7.3.6 Band alignment of $LaMnO_3/SrTiO_3$ heterojunction

In general, the relationships between the built-in potentials and carrier concentrations for *p-n* junctions of conventional semiconductors are given by the following equations [136]:

$$\begin{cases} V_{btot} = V_{bn} + V_{bp} \\ \dfrac{V_{bn}}{V_{bp}} = \dfrac{\varepsilon_p}{\varepsilon_n}\dfrac{N_p}{N_n} \end{cases} \qquad (7.1)$$

Here, V_{btot} is the total build-in potential formed at the interface of the *p-n* junction, while V_{bn} and V_{bp} are the potentials distributed on the *n*-type and *p*-type semiconductor sides, correspondingly. N_n (N_p) and ε_n (ε_p) are the donor (acceptor) density and relative permittivity in the *n*-type (*p*-type) semiconductor, respectively. In the present LMO/Nb:STO case, the V_{bn} values of 0.55±0.05 eV for the 0.1 at. % and 0.25±0.05 eV for 1.0 at. % Nb-doped STO sides are directly determined by XPS measurements. Assuming that (i) V_{btot}, ε_n, ε_p, and N_p remain unchanged for the two heterojunctions with the different Nb-doping concentrations; (ii) N_n and N_p remain unchanged near the boundaries of the junctions; and (iii) the dopant Nb atoms are fully activated in STO (namely, $N_n = 1.7\times10^{19}$ cm^{-3} for the 0.1 at. % and $N_n = 1.7\times10^{20}$ cm^{-3} for the 1.0 at. % Nb-doped STO), the value of V_{btot} can be estimated as follows.

The subscript of "1" is the notation for the heterojunction between $LaMnO_3$ (LMO) and 0.1 at. % Nb-doped $SrTiO_3$ (STO), while "2" for the heterojunction between LMO and 1.0 at. % Nb-doped STO. Assuming that the values of V_{btot}, ε_n, ε_p, and N_p are independent to the difference of Nb-doping level in STO ((i)), the following equations are obtained.

$$\begin{cases} V_{btot} = V_{bn1} + V_{bp1} = V_{bn2} + V_{bp2} = const. \\ \dfrac{\varepsilon_p N_p}{\varepsilon_n} = \alpha = const. \end{cases} \quad (7.2)$$

Using these equations, Eqs. (7.1) can be converted to following equations for the respective junctions:

$$\begin{cases} \dfrac{V_{bn1}}{V_{bp1}} = \dfrac{\alpha}{N_{n1}} \\ \dfrac{V_{bn2}}{V_{bp2}} = \dfrac{\alpha}{N_{n2}} \end{cases} \quad (7.3)$$

Thus, the following relation is obtained using the values of N_{n1} (1.7×10^{19} cm^{-3}) and N_{n2} (1.7×10^{20} cm^{-3}) that are calculated from the Nb concentration in respective Nb-doped STO.

$$\frac{V_{bn1}\cdot(V_{btot}-V_{bn2})}{V_{bn2}\cdot(V_{btot}-V_{bn1})}=\frac{N_{n2}}{N_{n1}}=10 \quad (7.4)$$

When I plug the values of V_{bn1} = 0.55±0.05 eV and V_{bn2} = 0.25±0.05 eV that are determined from XPS in the Eq. (7.4), V_{btot} were calculated to be 0.66±0.12 eV.

Because Eqs. (7.1) represent the distribution ratio of V_{btot} between the *n*-type and *p*-type semiconductor sides, the values of V_{bp} are calculated from these obtained potential values to be 0.11±0.07 eV for LMO/Nb:STO *p-n* junctions with the donor concentration of 0.1 at. % and 0.41±0.17 eV for those with the donor concentration of 1.0 at. %. The estimated value of V_{btot} is in good agreement with those evaluated from transport measurements, 0.64 eV [129] and 0.77 eV [113]. This agreement suggests that the junction properties of an LMO/Nb:STO heterointerface can be described in the framework of the conventional *p-n* junction model. [136]

From the values estimated from the conventional *p-n* junction model, I deduced the band diagrams of the two LMO/Nb:STO junctions with different donor concentrations, illustrated in Fig. 7.18. As mentioned before, since the VBM of the present LMO film is located around the Fermi level (see Fig. 7.16), the flat-band condition may also be fulfilled at the surface of the LMO film. Therefore, the band lineup between the two oxides can be evaluated accurately in the present case. Because Eqs. (7.1) represent the distribution ratio of V_{btot} between the *n*-type and *p*-type semiconductor sides, the built-in potential on the Nb:STO (LMO) side decreases (increases) from 0.55±0.05 eV (0.11±0.07 eV) to 0.25±0.05 eV (0.41±0.17 eV) by changing the donor concentration in STO from 0.1 at. % to 1.0 at. %. As can be seen in Fig. 7.18, the donor concentration dependence of the built-in potential formed at the interface between the Mott insulator LMO and the band insulator Nb:STO is well described by the conventional semiconductor theory.

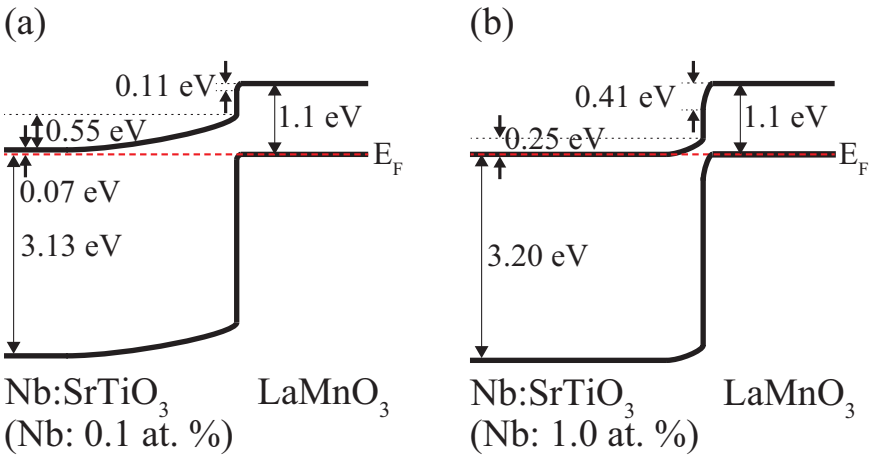

Figure 7.18: Band diagrams of LMO/Nb:STO heterojunctions deduced from the present XPS measurements for (a) 0.1 at. % and (b) 1.0 at. % Nb-doped STO. The band gaps of STO and LMO are 3.2 eV [135] and 1.1 eV [95], respectively.

In addition, I estimated the carrier density for the LMO side from Eqs. (7.1) based on the conventional *p-n* junction model. Using the relative permittivity of LMO (ε_p = 50 [113]) and STO (ε_n = 300), and the donor concentration N_n of the respective Nb:STO, N_p was calculated to be about 6×10^{20} cm^{-3}. This value means that only 0.04 holes per Mn site are activated, whereas one hole per Mn ion is expected in the case where LMO is not a Mott insulator. Although the estimated value is one order of magnitude larger than that obtained with photocurrent measurements, where N_p was found to be about 4×10^{19} cm^{-3} [113], the higher value of N_p is consistent with the observed positions of VBM in Fig. 7.16, indicating that the present LMO films are *p*-type degenerate semiconductors, probably because of oxygen excess and/or cation deficiency [81].

Based on the conventional *p*-n junction model, the thicknesses of the depletion layer for both junctions were estimated using the following equations [136]:

$$W_n = \left[\frac{2N_p\varepsilon_n\varepsilon_p V_{btot}}{eN_n(N_n\varepsilon_n + N_p\varepsilon_p)}\right]^{1/2}$$
$$W_p = \left[\frac{2N_n\varepsilon_n\varepsilon_p V_{btot}}{eN_p(N_n\varepsilon_n + N_p\varepsilon_p)}\right]^{1/2} \quad (7.5)$$

where W_n and W_p are the thicknesses of the depletion layer in Nb:STO and LMO layer, respectively. Using the calculated values of V_{btot} and N_p, the reported ε_p [113], and physical properties of Nb:STO (N_n and ε_n), W_n and W_p are estimated to be 33 nm and 0.9 nm for a 1.0 at. % Nb-doped STO junction, and 7.2 nm and 1.8 nm for a 1.0 at. % Nb-doped STO junction, respectively.

7.4 Conclusion

The existence of the charge transfer was investigated by XAS measurement for LMO/Nb:STO heterointerfaces. Ti-$L_{2,3}$ XAS spectra clearly show that the valence of Ti ion does not change between before and after contact, demonstrating that the charge transfer does not take place at an LMO/Nb:STO heterointerface. I have determined the band diagrams of LMO/Nb:STO heterojunctions and their dependence on donor concentration using XPS. The built-in potentials on the Nb:STO sides were experimentally determined by investigating the peak shifts of the Ti 2*p* and Sr 3*d* core level with LMO deposition. As the Nb-doping concentration increased from 0.1 at. % to 1.0 at. %, the built-in potentials in the Nb:STO sides were reduced from 0.55±0.05 eV to 0.25±0.05 eV, in accordance with the conventional *p-n* junction theory. This result demonstrates that LMO/Nb:STO heterojunctions can be described on the basis of the *p-n* junction model for conventional semiconductors irrespective of the strongly correlated electron nature of LMO. Not the charge transfer but the depletion of the "practical" carrier compensates the built-in potential at the heterointerface. Other mechanisms than the charge transfer may cause the exotic interfacial magnetism observed LMO-STO

superlattices.

Chapter 8
Summary and Future prospects

In the preceding chapters, the charge transfer phenomena and interfacial ferromagnetic states at the heterointerface of perovskite transition-metal oxides studied by synchrotron radiation spectroscopy were described. The heterointerfaces were grown by a pulsed laser deposition method. I have evaluated the two contrast heterointerfaces, $LaNiO_3$ (LNO) /$LaMnO_3$ (LMO) and LMO/Nb-doped $SrTiO_3$ (STO). Although both heterosturctures has been observed exotic interfacial magnetism, the charge transfer between B-site ions are expected for LNO/LMO, whereas not for LMO/Nb:STO in terms of their redox potential. As for LNO/LMO interface, first, I have investigated double perovskite La_2NiMnO_6 (LNMO) which can be regarded as a "natural superlattice" of LNO/LMO. And next, I developed LNMO to artificially fabricated LNO/LMO heterostuructures.

In Chapter 3, I have optimized the growth condition of LNMO thin films by pulsed laser deposition method. The film growth conditions were found to significantly affect the magnetic moment and ferromagnetic transition temperature of LNMO films. Epitaxial LNMO films exhibiting the ferromagnetism equivalent to that of bulk polycrystal were successfully grown only in such a narrow region of growth temperature and oxygen pressure that stabilized Ni^{2+}-O-Mn^{4+} superexchange ferromagnetic interaction. Out of this narrow region, the ferromagnetism is significantly suppressed by the appearance of secondary phases, locally disordered Ni and Mn ions and oxygen vacancies. Strict control of growth conditions is inevitable to obtain an LNMO film exhibiting a higher ferromagnetic transition temperature and a higher magnetic moment.

In Chapter 4, I have evaluated the charge transfer between Ni and Mn ions and verified the origin of ferromagnetism in LNMO using Ni-$L_{2,3}$and Mn-$L_{2,3}$-x-ray absorption

spectroscopy (XAS) and x-ray magnetic circular dichroism (XMCD). The valence change due to charge transfer from Mn to Ni ($Ni^{3+} + Mn^{3+} \rightarrow Ni^{2+} + Mn^{4+}$) occurs in LNMO and magnetizations residing in Ni^{2+} and Mn^{4+} ions align ferromagnetically. These results indicate that the ferromagnetism of LNMO are explained by a $Ni^{2+} - O - Mn^{4+}$ ferromagnetic superexchange interaction obeying a Kanamori-Goodenough rule. The charge transfer between Ni and Mn ions has a large influence on the ferromagnetism in LNMO. Electronic structures he valence band and the conduction band in LNMO films are also characterized using synchrotron radiation photoemission spectroscopy, O-*K* XAS, and optical spectroscopy. The electronic structure at the valence band maximum is mainly derived from the Mn 3*d* state. The conduction band minimum is composed mostly of the Mn 3*d*-O 2*p* hybridized state. The optical gap is estimated to be about 1.5 eV based on the optical conductivity derived from optical spectra.

In Chapter 5, in order to investigate the charge transfer phenomena at the heterointerface between LNO and LMO, I have performed *in situ* XAS measurements on artificially fabricated LNO/LMO multilayers. The Ni-$L_{2,3}$ and Mn-$L_{2,3}$ XAS spectra clearly show the occurrence of electron transfer from Mn to Ni ions in the interface region. Detailed analysis of the thickness dependence of these XAS spectra has revealed that the spatial distribution of the transferred charges across the interface is significantly different between LNO and LMO: 1 ML for LNO and 3-4 ML for LMO. The difference of the observed spatial distribution is presumably described by the charge spreading model that treats the transfer integral between neighboring transition metal ions and the Coulomb interaction, rather than the Thomas–Fermi screening model [103].

In Chapter 6, in order to investigate the relationship between the charge transfer and the interfacial ferromagnetism of LNO/LMO heterostructures, I have carried out XMCD measurements on LNO/LMO trilayer structures. The Ni-$L_{2,3}$ XMCD spectra of trilayers reveal that the net magnetization is induced in Ni ions in an LNO layer which is paramagnetic in bulk phase and it is constricted in Ni^{2+} ions at 1-ML LNO at the interface which is related to the charge transfer. On the other hand, the net spins in an LMO layer reside in both Mn^{3+} and Mn^{4+}

ions which are located in some monolayers from the interface. The same sign of XMCD signals between Ni-$L_{2,3}$ and Mn-$L_{2,3}$ edge indicates that the Ni spins and Mn spins couple ferromagnetically across the interface. It is concluded that the charge transfer between Ni and Mn ions is a key for the interfacial ferromagnetism in LNO/LMO heterostructures.

In Chapter 7, I have performed XAS measurement in order to investigate the existence of the charge transfer at an LMO/Nb:STO heterointerface. Ti-$L_{2,3}$ XAS spectra clearly show not occurrence of the charge transfer between Ti and Mn ions in contrast to an LNO/LMO heterointerface Therefore, I have evaluated interfacial electronic structure by determining the band diagram of LMO/Nb:STO heterojunctions using x-ray photoemission spectroscopy. By changing the donor concentration in Nb:STO from 0.1 at. % to 1.0 at. %, the value of the built-in potential for the Nb:STO side (V_{bn}) is reduced from 0.55±0.05 eV to 0.25±0.05 eV. The modulation of V_{bn} is well described in the framework of the conventional *p-n* junction model, suggesting that the built-in potential at the heterointerface is compensated not by the charge transfer between B-site ions but by the depletion of the "practical" carrier. These results imply that the novel interfacial magnetism observed in LMO-STO superlattices are caused by other mechanisms than the charge transfer.

In this thesis, the charge transfer phenomena, the valence change and its spatial distribution, and the interfacial ferromagnetism related to the charge transfer have been investigated by synchrotron radiation spectroscopy utilizing its elemental selectivity and surface (interface) sensitivity. In order to clarify the origin of the novel ferromagnetism observed at the interface of transition metal oxides, it should be important to obtain the knowledge of the interfacial charge transfer. Based on the knowledge obtained in this study, fabrication of the appropriate interface and then control of the charge distribution at the heterointerface are considered to lead to the design and control the beneficial magnetic properties emerging at the interface of transition metal oxides.

One approach to modulate the interfacial charge transfer is the control of the interfacial structure. The stacking orientation is an important parameter to decide the charge transfer phenomena. For (001)/(011)/(111)-stacking of $ABO_3/AB'O_3$ heterointerfaces, as shown in Fig. 8.1, there are one/two/three B-O-B' bond, while five/four/three B-O-B' bond. Therefore, it is expected that the amount of the charge transfer is largest (smallest) for the (111)-orientation ((001)-orientation) because (111)-staking ((001)-orientation) has the most (the least) B-O-B' bonds. This trend has been observed in XAS studies by Piamonteze and coworkers [102]. However, Dong and coworkers reported the totally inverse trend predicted by the tight-binding calculation [137]. Furthermore, as for the relationship between the charge transfer and induced interfacial ferromagnetism, there are two opposite calculation results: Dong and coworkers have demonstrated that the amounts of the charge transfer is not related to the strength of interfacial ferromagnetism [137], while Lee and coworkers have concluded that induced magnetic moment is proportional to the amount of the charge transfer [138]. It will be necessary to systematically understanding the relationship between the stacking orientation, the charge transfer, and the interfacial magnetism. The present approach using the elementally selective spectroscopic measurements is considered to be a powerful tool to experimentally elucidate this relationship.

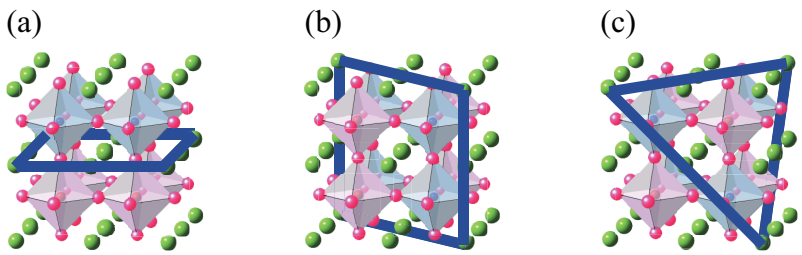

Figure 8.1: The images of various oriented interfaces. (a) (001), (b) (110), and (c) (111)-orientation.

Another structural modulation at the interface is obtained by utilizing layered perovskite structures. Figure 8.2 shows Ruddeleson-Popper (RP) type and Dion-Jacobson (DJ) type interfaces. In RP type interface, perovskite slabs are offset by a (1/2, 1/2) translation and DJ type interface has alkali metals as the separating motif, resulting in the suppression of the charge transfer.

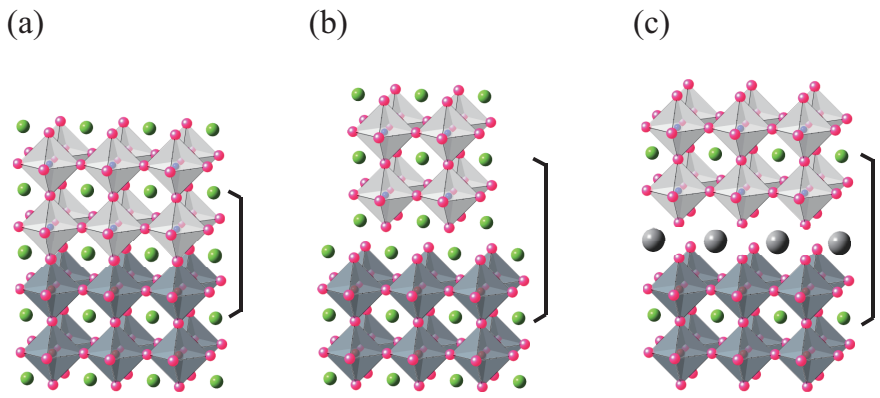

Figure 8.2: The images of various perivskite-based interfaces. (a) perovskite-type, (b) Ruddeleson-Popper type, and (c) Dion-Jacobson type interface.

Interfacial ferromagnetism are affected by not only the charge transfer phenomena, but also other parameters, such as the strain and structural coupling, and orbital polarization, and so on. Furthermore, the external electric or magnetic field could alter the interfacial charge transfer and/or orbital reconstruction. There may be fruitful area of a fundamental research as well as a path for device application at the heterointerfaces between transition metal oxides.

Bibliography

[1] M. K. Wu, J. R. Ashburn, C. J. Torng, P. H. Hor, R. L. Meng, L. Gao, Z. J. Huang, Y. Q. Wang, and C. W. Chu, Phys. Rev. Lett. **58**, 908 (1987).

[2] M. Imada, A. Fujimori, and Y. Tokura, *Rev. Mod. Phys.* **70**, 1039 (1998).

[3] Y. Tomioka, A. Asamitsu, H. Kuwahara, Y. Moritomo, and Y. Tokura, Phys. Rev. B **53**, R1689(R) (1996).

[4] J. Wang, J. B. Neaton, H. Zheng, V. Nagarajan, S. B. Ogale, B. Liu, D. Viehlamd, V. Vaithyanathan, D. G. Schlom, U. V. Waghmare, N. A. Spaldin, K. M. Rabe, M. Wuttig, R. Ramesh, Science **299**, 1719 (2003).

[5] H. Y. Hwang, Y. Iwasa, M. Kawasaki, B. Keimer, N. Nagaosa, and Y. Tokura, Nat. Mater. **11**, 103 (2012).

[6] J. Mannhart, and D. G. Schlom, Science **327**, 1607 (2010).

[7] P. Zubko, S. Gariglio, M. Gabay, P. Ghosez, and J. -M. Triscone, *Annu. Rev. Condens. Matter Phys.* **2**, 141 (2011).

[8] A. Ohtomo, D. A. Muller, J. L. Grazul, and H. Y. Hwang, Nature **419**, 378 (2002).

[9] A. Ohtomo, and H. Y. Hwang, Nature **427**, 423 (2004).

[10] N. Reyren, S. Thiel, A. D. Caviglia, L. F. Kourkoutis, G. Hammert, C. Richter, C. W. Schneider, T. Kopp, A. -S. Rüetschi, D. Jaccard, M. Gabay, D. A. Muller, J. -M. Triscone, and J. Mannhart, Science **317**, 1196 (2007).

[11] K. Ueda, H. Tabata, and T. Kawai, Science **280**, 1064 (1998).

[12] K. Ueda, H. Tabata, and T. Kawai, J. Appl. Phys. **89**, 2847 (2001).

[13] T. Koida, M. Lippmaa, T. Fukumura, K. Itaka, Y. Matsumoto, M. Kawasaki, and H. Koinuma, Phys. Rev. B **66**, 144418 (2002).

[14] C. Adamo, X. Ke, P. Schiffer, A. Soukiassian, M. Warusawithana, L. Maritato, and D. G. Schlom, Appl. Phys. Lett. **92**, 112508 (2008).

[15] K. S. Takahashi, M. Kawasaki, and Y. Tokura, Appl. Phys. Lett. **79**, 1324 (2001).

[16] J. W. Freeland, J. Chakhalian, A. V. Boris, J.-M. Tonnerre, J. J. Kavich, P. Yordanov, S. Grenier, P. Zschack, E. Karapetrova, P. Popovich, H. N. Lee, and B. Keimer, Phys. Rev. B **81**, 094414 (2010).

[17] C. He, A. J. Grutter, M. Gu, N. D. Browning, Y. Takamura, B. J. Kirby, J. A. Borchers, J. W. Kim, M. R. Fitzsimmons, X. Zhai, V. V. Mehta, F. J. Wong, and Y. Suzuki, Phys. Rev. Lett. **109**, 197202 (2012).

[18] A. J. Grutter, H. Yang, B. J. Kirby, M. R. Fitzsimmons, J. A. Aguiar, N. D. Browning, C. A. Jenkins, E. Arenholtz, V. V. Mehta, U. S. Alaan, and Y. Suzuki, Phys. Rev. Lett. **111**, 087202 (2013).

[19] H. Yamada, M. Kawasaki, T. Lottermoser, T. Arima, and Y. Tokura, Appl. Phys. Lett. **89**, 052506 (2006).

[20] T. S. Santos, B. J. Kirby, S. Kumar, S. J. May, J. A. Borchers, B. B. Maranville, J. Zarestky, S. G. E. te Velthuis, J. van den Brink, and A. Bhattacharya, Phys. Rev. Lett. **107**, 167202 (2011).

[21] J. C. Rojas Sánchez, B. Nelson-Cheeseman, M. Granada, E. Arenholz, and L. B. Steren, *Phys. Rev. B* **85**, 094427 (2012).

[22] X. Ning Z. Wang, and Z. Zhang, *Sci. Rep.* **5**, 8460 (2015).

[23] J. Chakhalian, J. W. Freeland, G. Srajer, J. Strempfer, G. Khaliullin, J. C. Cezer, T. Charlton, R. Dalgliesh, C. Bernhard, G. Cristiani, H.-U. Habermeier, and B. Keimer, Nat. Phys. **2**, 244 (2006).

[24] W. S. Choi, D. W. Jeong, S. S. A. Seo, Y. S. Lee, T. H. Kim, S. Y. Jang, H. N. Lee, and K. Myung-Whun, Phys. Rev. B **83** 195113 (2011).

[25] J. Hoffman, I. C. Tung, B. B. Nelson-Cheeseman, M. Liu, J. W. Freeland, and A. Bhattacharya, *Phys. Rev. B* **88**, 144411 (2013).

[26] J. Garcia-Barriocanal, F. Y. Bruno, A. Rivera-Calzada, Z. Sefrioui, N. M. Nemes, M. Garcia-Hernández, J. Rubio-Zuazo, G. R. Castro, M. Varela, S. J. Pennycook, C. Leon, and J. Santamaria, Adv. Mater. **22**, 627 (2010).

[27] M. Gibert, P. Zubko, R. Scherwitzl, J. Íñiguez, and J.-M. Triscone, *Nat. Mater.* **11**, 195 (2012).

[28] T. Ohzuku, S. Takeda, and M. Iwanaga, J. Power Sources **81**, 90 (1999).

[29] T. Ohzuku, A. Ueda, and N. Yamamoto, J. Electrochem. Soc. **142**, 1431 (1995).

[30] P. -Q. Nilsson, Appl. Optics **7**, 435 (1968).

[31] S. Hüfner, *Photoelectron Spectroscopy* (Springer-Verlag, Berlin,1995).

[32] C. T. Chen, Y. U. Idzerda, H. -J. Lin, N. V. Smith, G. Meigs, E. Chaban, G. H. Ho, E. Pellegrin, and F. Sette, Phys. Rev. Lett. **75**, 152 (1995).

[33] B. T. Thole, P. Carra, F. Sette, and G. van der Laan, Phys. Rev. Lett. **68**, 1943 (1992).

[34] P. Carra, B. T. Thole, M. Altarelli, and X. Wang, Phys. Rev. Lett. **70**, 694 (1993).

[35] K. Horiba, H. Ohguchi, H. Kumigashira, M. Oshima, K. Ono, N. Nakagawa, M. Lippmaa, M. Kawasaki, and H. Koinuma, Rev. Sci. Instrum. **74**, 3406 (2003).

[36] M. Watanabe, A. Toyoshima, Y. Azuma, T. Hayaishi, Y. Yan, and A. Yagishita, Proc. SPIE **3150**, 58 (1997).

[37] K. Amemiya, A. Toyoshima, T. Kikuchi, T. Kosuge, K. Nigorikawa, R. Sumii, and K. Ito,

AIP Conf. Proc. **1234**, 295 (2010).

[38] T. Muro, T. Nakamura, T. Matsushita, H. Kimura, T. Nakatani, T Hirono, T. Kudo, K. Kobayashi, Y. Saitoh, M. Takeuchi, T. Hara, K Shirasawa, and H. Kitamura, J. Electron Spectrosc. Relat. Phenom. **144-147**, 1101 (2005).

[39] K. Amemiya, M. Sakamaki, T. Koide, K. Ito, K. Tsuchiya, K. Harada, T. Aoto, T. Shioya, T. Obina, S. Yamamoto, and Y. Kobayashi, J. Phys.: Conf. Ser. **425** 152015 (2013).

[40] N. A. Subramanian, D. Li, N. Duan, B. A. Reisner, and A. W. Sleight, J. Solid. State Chem. **151**, 323 (2000).

[41] M. T. Anderson, K. B. Greenwood, G. A. Taylor, and K. R. Poeppelmeier, Prog. Solid St. Chem. **22**, 197, (1993).

[42] A. K. Azad, A. Mellergård, S. -G. Erinksson, S. A. Ivanov, S. M. Yunus, F. Linderg, G. Svensson, and R. Mathieu, Mater. Res. Bull. **40**, 1633 (2005).

[43] M. R. Suchomel, C. I. Thomas, M. Allix, M. J. Rosseinsky, A. M. Fogg, and M. F. Thomas, Appl. Phys. Lett. **90**, 112909 (2007).

[44] R. Nechache, C. Harnagea, A. Pignolet, F. Normandin, T. Veres, L. -P. Carignan, and D. Menard, Appl. Phys. Lett. **89**, 102902 (2006).

[45] A. Masuno, M. Haruta, M. Azuma, H. Kurata, S. Isoda, M. Takano, and Y. Shimakawa, Appl. Phys. Lett, **89**, 211913 (2006).

[46] K. -I. Kobayashi, T. Kimura, H. Sawada, K. Terakura, and Y. Tokura, Nature **395**, 677 (1998).

[47] B. T. Matthias, R. M. Bozorth, and J. H. Van Vleck, Phys. Rev. Lett. **7**, 160 (1961).

[48] P. K. Baltzer, H. W. Lehmann, and M. Robbins, Phys. Rev. Lett. **15**, 493 (1965).

[49] M. A. Subramanian, A. P. Ramirez, and W. J. Marshall, Phys. Rev. Lett. **82**, 1558 (1999).

[50] T. Kimura, S. Kawamoto, I. Yamada, M. Azuma, M. Takano, and Y. Tokura, Phys. Rev. B **67**, 180401 (2003).

[51] R. Mathieu, B. S. Sørensen, J. Sadowski, U. Södervall, J. Kanski, P. Svedlindh, P. E.

Lindelof, D. Hrabovsky, and E. Vanelle, Phys. Rev. B **68**, 184421 (2003).

[52] D. Chiba, K. Takamura, F. Matsukura, and H. Ohno, Appl. Phys. Lett. **82**, 3020 (2003).

[53] K. Ueda, H. Tabata, and T. Kawai, Appl. Phys. Lett. **79**, 988 (2001).

[54] Y. Matsumoto, R. Takahashi, M. Murakami, T. Koida, X. -J. Fan, T. Hasegawa, T. Fukumura, M. Kawasaki, S. -Y. Koshihara, and H. Koinuma, Jpn. J. Appl. Phys. **40**, L1204 (2001).

[55] Y. Matsumoto, M. Murakami, T. Shono, T. Hasegawa, T. Hasegawa, T. Fukumura, M. Kawasaki, P. Ahmet, T. Chikyow, S. Koshihara, and H. Koinuma, Science **291**, 854 (2001).

[56] S. B. Ogale, R. J. Choudhary, J. P. Buban, S. E. Lofland, S. R. Shinde, S. N. Kale, V. N. Kulkarni, J. Higgins, C. Lanci, J. R. Simpson, N. D. Browning, S. Das Sarma, H. D. Drew, R. L. Greene, and T. Venkatesan, Phys. Rev. Lett. **91**, 077205 (2003).

[57] N. S. Rogado, J. Li, A. W. Sleight, and M. A. Subramanian, Adv. Mater. **17,** 2225 (2005).

[Dass PRB67] R. I. Dass, and J. B. Goodenough, Phys. Rev. B **67**, 014401 (2003).

[58] M. Hashisaka, D. Kan, A. Masuno, T. Terashima, M. Takano, and K. Mibu, J. Magn. Magn. Mater. **310**, 1975 (2007).

[59] Y. Shiomi, and E. Saitoh, Phys. Rev. Lett. **113**, 266602 (2014).

[60] A. Wold, R. J. Arnott, and J. B. Goodenough, J. Appl. Phys. **29**, 387 (1958).

[61] J. B. Goodenough, A. Wold, R. J. Arnott, and N. Menyuk, Phys. Rev. **124**, 373 (1961).

[62] G. Blasse, J. Phys. Chem. Solids **26**, 1969 (1965).

[63] K. Asai, H. Sekikawa, and S. Iida, J. Phys. Soc. Jpn. **47**, 1054 (1979).

[64] M. Sonobe, and K. Asai, J. Phys. Soc. Jpn. **61**, 4193 (1992).

[65] M. C. Sánchez, J. García, J. Blasco, G. Subías, and J. Pérez-Cacho, Phys. Rev. B **65** 144409 (2002).

[66] J. Blasco, M. C. Sánchez, J. Pérez-Cacho, J. García, G. Subías, and J. Campo, J. Phys.

Chem. Solids **63**, 781 (2002).

[67] C. L. Bull, D. Gleeson, and K. S. Knight, J. Phys. Condens. Matter, **15**, 4927 (2003).

[68] R. I. Dass, J. -Q. Yan, and J. B. Goodenough, Phys. Rev. B **68**, 064415 (2003).

[69] M. Hashisaka, D. Kan, A. Masuno, M. Takano, Y. Shimakawa, T. Terashima, and K. Mibu, Appl. Phys. Lett. **89**, 032504 (2006).

[70] V. L. Joseph Joly, P. A. Joy, S. K. Date, and C. S. Gopinath, Phys. Rev. B **65**, 184416 (2002).

[71] M. P. Singh, C. Grygiel, W. C. Sheets, Ph. Boullay, M. Hervieu, W. Prellier, B. Mercey, Ch. Simon, and B. Raveau, Appl. Phys. Lett. **91**, 012503 (2007).

[72] H. Z. Guo, J. Burgess, E. Ada, S. Street, A. Gupta, M. N. Iliev, A. J. Kellock, C. Magen, M. Varela, and S. J. Pennycook, Phys. Rev. B **77**, 174423 (2008).

[73] T. Manako, M. Izumi, Y. Konishi, K.-I. Kobayashi, M. Kawasaki, and Y. Tokura, Appl. Phys. Lett. **74**, 2215 (1999).

[74] J. A. M. Van Roosmalen, E. H. P. Cordfunke, R. B. Helmholds, and H. W. Zandbergen, J. Solid State Chem. **110** 100 (1994).

[75] J. A. M. Van Roosmalen, and E. H. P. Cordfunke, J. Solid State Chem. **110** 106 (1994).

[76] B. C. Tofield, and W. R. Scott, J. Solid State Chem. **10,** 183 (1974).

[77] R. Takahashi, I. Ohkubo, K. Yamauchi, M. Kitamura, Y. Sakurai, M. Oshima, T. Oguchi, Y. Cho, and M. Lippmaa, Phys. Rev. B **91**, 134107 (2015).

[78] R. Takahasi in private communication.

[79] J. J. Neumeier, and J. L. Cohn, Phys. Rev. B **61**, 14319 (2000).

[80] C. Ritter, M. R. Ibarra, J. M. De Teresa, P. A. Algarabel, C. Marquina, J. Blasco, J. García, S. Oseroff, and S-W. Cheong, Phys. Rev. B **56**, 8902 (1997).

[81] J. Töpfer, and J. B. Goodenough, J. Solid State Chem. **130**, 117 (1997).

[82] M. P. Singh, K. D. Truong, S. Jandl, and P. Fournier, J. Appl. Phys. **107**, 09D917 (2010).

[83] Y. Sakurai, I. Ohkubo, Y. Matsumoto, H. Koinuma, and M. Oshima, J. Appl. Phys. **110**,

063913 (2011).

[84] H. Guo, J. Burgess, S. Street, A. Gupta, T. G. Calvarese and M. A. Subramanian, Appl. Phys. Lett. **89**, 022509 (2006).

[85] M. Medarde, A. Fontaine, J. L. García-Muñoz, J. Rodríguez-Carvajal, M. de Santis, M. Sacchi and G. Rossi, Phys. Rev. B **46**, 14975 (1992).

[86] H. Wadati, M. Takizawa, T. T. Tran, K. Tanaka, T. Mizokawa, A. Fujimori, A. Chikamatsu, H. Kumigashira, M. Oshima, S. Ishiwata, M. Azuma, and M. Takano,Phys. Rev. B **72**, 155103 (2005).

[87] M. Abbate, F. M. F de Groot, J. C. Fuggle, A. Fujimori, O. Strebel, F. Lopez, M. Domke, G. Kaindl, G. A. Sawatzky, M. Takano, Y. Takeda, H. Esaki and S. Uchida, Phys. Rev. B **46**, 4511 (1992).

[88] C. Mitra, Z. Hu, P. Raychandhuri, S. Wirth, S. I. Csiszar, H. H. Hsieh, H.-J. Lin, C. T. Chen and L. H. Tjeng, Phys. Rev. B **67**, 092404 (2003).

[89] H. Guo, A. Gupta, M. Varela, S. Pennycook, and J. Zhang, Phys. Rev. B **79**, 172402 (2009).

[90] J. -S. Kang, S. M. Lee, D. H. Kim, S. Kolesnik, B. Dabrowski, B. -G. Park, J. -Y. Kim. J. Lee, B. Kim, and B. I. Min, J. Appl. Phys. **107**, 09D721 (2010).

[91] T. Burnus, Z. Hu, H. H. Hsieh, V. L. J. Joly, P. A. Joy, M. W. Haverkort, H. Wu, A. Tanaka, H. -J. Lin, C. T. Chen, and L. H. Tjeng, Phys. Rev. B **77**, 125124 (2008).

[92] K. Horiba, A. Chikamatsu, H. Kumigashira, M. Oshima, N. Nakagawa, M. Lippmaa, K. Ono, M. Kawasaki and H. Koinuma, Phys. Rev. B **71**, 155420 (2005).

[93] K. Horiba, R. Eguchi, M. Taguchi, A. Chainani, A. Kikkawa, Y. Senba, H. Ohashi and S. Shin, Phys. Rev. B **76**, 155104 (2007).

[94] T. Mizokawa, A. Fujimori, T. Arima, Y. Tokura, N. Mōri and J. Akimitsu, Phys. Rev. B **52**, 13865 (1995).

[95] T. Arima, Y. Tokura, and J. B. Torrance, Phys. Rev. B **48**, 17006 (1993).

[96] M. Abbate, G. Zampieri, F. Parado, A. Caneiro, J. M. Gonzalez-Calbet and M. Vallet-Regi, Phy. Rev. B **65**, 155101 (2002).

[97] M. Abbate, G. Zampieri, F. Prado, A. Caneiro and A. R. B. de Castro, Solid State Commun. **111**, 437 (1999).

[98] P. Kuiper, J. van Elp, G. A. Sawatzky, A. Fujimori, S. Hosoya and D. M. de Leeuw, Phys. Rev. B **44**, 4570 (1991).

[99] Y. Sakurai, Master thesis (2012).

[100] H. Das, U. V. Waghmare, T. Saha-Dasgupta and D. D. Sarma, Phys. Rev. Lett **100**, 186402 (2008).

[101] S. F. Mater, M. A. Subramanian, A. Villesuzanne, V. Eyert, M. -H. Whangbo, J. Mag. Mag. Mater. **308**, 116 (2009).

[102] C. Piamonteze, M. Gibert, J. Heidler, J. Dreiser, S. Rusponi, H. Brune, J. -M. Triscone, F. Nolting, and U. Staub, *Phys. Rev. B* **92**, 014426 (2015).

[103] C. Lin, S. Okamoto, and A. J. Millis, *Phys. Rev. B* **73**, 041104(R) (2006).

[104] S. Tanuma, C. J. Powell, and D. R. Penn, Surf. Interface Anal. **35**, 268 (2003).

[105] S. J. May, A. B. Shah, S. G. E. te Velthuis, M. R. Fitzsimmons, J. M. Zuo, X. Zhai, J. N. Eckstein, S. D. Bader, and A. Bhattacharya, Phys. Rev. B **77**, 174409 (2009).

[106] M. Gibert, M. Viret, A. Torres-Pardo, C. Piamonteze, P. Zubko, N. Jaouen, J.-M. Tonnerre, A. Mougin, J. Fowlie, S. Catalano, A. Gloter, O. Stéphan, J.-M. Triscone, Nano Lett. **15**, 7355 (2015).

[107] E. Sakai, M. Tamamitsu, K. Yoshimatsu, S. Okamoto, K. Horiba, M. Oshima, and H. Kumigashira, *Phys. Rev. B* **87**, 075132 (2013).

[108] K. Horiba, H. Kawanaka, Y. Aiura, T. Saitoh, C. Satoh, Y. Kikuchi, M. Yokoyama, Y. Nishihara, R. Eguchi, Y. Senba, H. Ohashi, Y. Kitajima, and S. Shin, Phys. Rev. B **81**, 245127 (2010).

[109] A. Hoffmann, S. G. E. te Velthuis, Z. Sefrioui, J. Santamaría, M. R. Fitzsimmons, S. Park, and M. Varela, *Phys. Rev. B* **72**, 140407 (R) (2005).

[110] N. Mikoshiba, "Handotai no butsuri" (Physics of semiconductor) (Japanese) (Baifukan, Tokyo, 1982).

[111] M. Jouffroy, A. Gire, J.-G. Théobald, G. Bardèche, F. Torrealba-Anzola, and A. Chambaudet, *J. Phys. Chem. Solids* **60**, 181 (1999).

[112] K. P. Rajeev, G. V. Shivashankar, and A. K. Raychaudhuri, *Solid State Commun.* **79**, 591 (1991).

[113] J. Fujioka, M. Nakamura, M. Kawasaki, and Y. Tokura, J. Appl. Phys. **111**, 016107 (2012).

[114] T. Okuda, A. Asamitsu, Y. Tomioka, T. Kimura, Y. Taguchi, and Y. Tokura, *Phys. Rev. Lett.* **81**, 3203 (1998).

[115] L. Ghivelder, I. Abrego Castillo, M. A. Gusmão, J. A. Alonso, and L. F. Cohen, *Phys. Rev. B* **60**, 12184 (1999).

[116] J. C. Slater and G. F. Koster, *Phys. Rev.* **94**, 1498 (1954).

[117] P. Mahadevan, N. Shanthi, and D. D. Sarma, *Phys. Rev. B* **54**, 11199 (1996).

[118] T. Koide, H. Miyauchi, J. Okamoto, T. Shidara, T. Sekine, T. Saitoh, A. Fujimori, H. Fukutani, M. Takano, and Y. Takeda, Phys. Rev. Lett. **87**, 246404 (2001).

[119] G. Shibata, K. Yoshimatsu, E. Sakai, V. R. Singh, V. K. Verma, K. Ishigami, T. Harano, T. Kadono, Y. Takeda, T. Okane, Y. Saitoh, H. Yamagami, A. Sawa, H. Kumigashira, M. Oshima, T. Koide, and A. Fujimori, Phys. Rev. B **89**, 253123 (2014).

[120] J. -H. Park, E. Vescovo, H. -J. Kim, C. Kwon, R. Ramesh, and T. Venkatesan, Phys. Rev. Lett. **81**, 1953 (1998).

[121] J. Garcia-Barriocanal, J. C. Cezar, F. Y. Bruno, P. Thakur, N. B. Brookes, C. Utfeld, A.

Rivera-Calzada, S. R. Giblin, J. W. Taylor, J. A. Duffy, S. B. Dugdale, T. Nakamura, K. Kodama, C. Leon, S. Okamoto, and J. Santamaria, Nat. Commun. **1**, 82 (2010).

[122] X. Zhai, C. S. Mohapatra, A. B. Shah, J. M. Zuo, and J. N. Echstein, J. Appl. Phys. **113**, 173913 (2013).

[123] F. Cossu, N. Singh, and U. Schwingenschlögl, Appl. Phys. Lett. **102**, 042401 (2013).

[Kobayashi JAP96] D. Kobayashi, H. Kumigashira, M. Oshima, T. Ohnishi, M. Lippmaa, K. Ono, M. Kawasaki, and H. Koinuma, J. Appl. Phys. **96**, 7183 (2004).

052506 (2006).

[124] A. B. Shah, Q. M. Ramasse, X. Zhai, J. G. Wen, S. J. May, I. Petrov, A. Bhattacharya, P. Abbamonte, J. N. Eckstein, and J.-Min Zuo, Adv. Mater. **22**, 1156 (2010).

[125] J. A. Mundy, Y. Hikita, T. Hidaka, T. Yajima, T. Higuchi, H. Y. Hwang, D. A. Muller, and L. F. Kourkoutis, Nat. Comm. **5**, 3464 (2014).

[126] H. Tanaka, J. Zhang, and T. Kawai, Phys. Rev. Lett. **88**, 027204 (2002).

[127] A. Sawa, T. Fujii, M. Kawasaki, and Y. Tokura, Appl. Phys. Lett. **86**, 112508 (2005).

[128] H. P. R. Frederikse and W. R. Hosler, Phy. Rev. **161**, 822 (1967).

[129] M. Nakamura, A. Sawa, J. Fujioka, M. Kawasaki, and Y. Tokura, Phys. Rev. B **82**, 201101 (2010).

[130] M. Abbate, F. M. F. de Groot, J. C. Fruggle, A. Fujimori, Y. Tokura, Y. Fujishima, O. Strebel, M. Domke, G. Kaindl, J. van Elp, B. T. Thole, G. A. Sawatky, M. Sacchi, and N. Tsuda, Phys. Rev. B **44**, 5419 (1991).

[131] A. S. Disa, D. P. Kumah, A. Malashevich, H. Chen, D. A. Arena, E. D. Specht, S. Ismail-Beigi, F. J. Walker, and C. H. Ahn, Phy. Rev. Lett. **114**, 026801 (2015).

[132] X. Zhai, L. Cheng, Y. Liu, C. M. Schlepütz, S. Dong, H. Li, X. Zhang, S. Chu, L. Zheng,

J. Zhang, A. Zhao, H. Hong, A, Bhattacharya, J. N. Eckstein, and C. Zeng, Nat. Commun. **5**, 4283 (2014).

[133] J.-H. Park, C. T. Chen, S. W. Cheong, W. Bao, G. Meigs, V. Chakarian, and Y. U. Idzerda, Phys. Rev Lett. **76**, 4215 (1996).

[134] M. Minohara, I. Ohkubo, H. Kumigashira, and M. Oshima, Appl. Phys. Lett. **90**, 132123 (2007).

[135] J. A. Noland, Phys. Rev. **94**, 724 (1954).

[136] S. M. Sze and K. K. Ng, Physics of Semiconductor Devices, 3rd ed. (Wiley, Hoboken, NJ, 2007).

[137] S. Dong, and E. Dagotto, Phys. Rev. B **87**, 195116 (2013).

[138] A. T. Lee, and M. J. Han, Phys. Rev. B **88**, 035126 (2013).

Acknowledgements

It is my great pleasure to express my heartfelt gratitude to the following people for their supports concerning my doctoral thesis. I could never finish my PhD course without their help.

First of all, I would like to express my deepest gratitude to my supervisor of doctoral course, Prof. Hiroshi Fujioka, who has given me the opportunities to be engaged in this research, and to work at the University of Tokyo as well as the Photon Factory, KEK (KEK-PF). He provided me with a lot of helpful advices and encouragements.

I would like to express my cordial gratitude to my supervisor of bachelor and master courses, Prof. Masaharu Oshima, who has given me the guidance, lessons encouragements, and opportunities to work on the research using synchrotron radiation and guided me to the PhD course again. His energies toward science, research and instruction of students are always enlightening.

I would like to express my sincere gratitude to Prof. Hiroshi Kumigashira, who has given me the occasion to research at the KEK-PF, for teaching me various principals and skills of spectroscopies and giving me earnest guidance of presentation and writing papers.

I am deeply grateful to Dr. Isao Ohkubo for giving me the opportunity to work on an interesting research subject “Oxide thin films”, teaching me many basic skills and knowledge indispensable in material research, lots of useful discussions and sincere advices.

I would like to express my special gratitude to Prof. Koji Horiba for teaching me lots

enlightening knowledge on spectroscopy and condensed matter physics, and his kind support for not only my research but also my mind. His latitudinous knowledge always encourages me.

I would like to express my deep gratitude to members of Kumigashira laboratory, KEK-PF. Special thanks go to Dr. Masaki Kobayashi for guiding me to the PhD course, mental support, and teaching me lots of experimental and analytical skills. I also thank to Dr. Enju Sakai, Dr. Makoto Minohara, Dr. Ryu Yukawa, Mr. Taichi Mitsuhashi, Mr. Masatomo Tamamitsu, and Mr. Koji Nakata for lots of helpful advice, essential supports at beam time, and sharing much time with me.

I wish to express my sincere acknowledgement to members of Oshima laboratory, especially “Ohkubo group”. Special thanks go to Mr. Toshihiro Ishihara for lots of helps, discussions and encouragements. I am also grateful to Dr. Kenta Tsubouchi, Dr. Takayuki Harada, Mr. Genya Sugano, and Ms. Mari Isobe for fruitful discussions, supports and sharing much time with the fun and pain.

I would also thank to Prof. Yoshihisa Harada, Dr. Toshiyuki Taniuchi, Dr. Satoshi Toyoda, Dr. Akira Chikamatsu, Dr. Naoka Nagamura, Dr. Shoichi Hidai, Mr. Yoichi Sakuma, Mr. Kazuya Mitamura, Mr. Ken Kanai, Mr. Haruhiko Takahashi, Mr. Riichiro Takaishi, Mr. Atsushi Maniwa, Mr. Yasumasa Wada, Ms. Remi Ohba, Mr. Kotaro Kubo, Dr. Ryutaro Yasuhara, Dr. Jianwei Liu, Ms. Rumiko Ito, Mr. Kazuma Shimomoto, Mr. Tatsuhiko Tanimura, Mr. Yasushi Toyoshima, Dr. Kohei Yoshimatsu, Mr. Yuko Okano, Mr. Yosuke Kato, Mr. Hiroyuki Kamada, Mr. Yuki Nakamura, Dr. Hideharu Niwa, Mr. Tomoaki Fujii, Ms. Yoko Toyoda, Mr. Takashi Okabe, Mr. Tomofumi Kajima, Mr. Makoto Saitoh, and Mr. Taiki Yamamoto.

Acknowledgements

I would like to express my deep gratitude to members of Fujioka laboratory Dr. Jitsuo Ohta, Dr. Atsushi Kobayashi, Dr. Kohei Ueno, Dr. Shigeru Inoue, Dr. Myung-Hee Kim, Dr. Koichiro Okamoto, Ms. Ruriko Takatsuki, Mr. Kazuhiro Sato, Mr. Kyohei Irie, Dr. Yao Guo, Dr. Jeong-Woo Shon, Ms. Hye-Ryun Kim, Mr. Yasuaki Arakawa, Ms. Kana Ohkubo, Mr. Ryuta Tanaka, Mr. Masaaki Ooseki, Mr. Eiji Kishikawa, Mr. Takuto Watanabe, Mr. Takeki Ito, Mr. Masaya Ohhashi, Mr. Hidenari Noguchi, Mr. Hiroaki Hamashima, Ms. KheShin Lye, Mr. Masayuki Shinozuka and Mr. Kousuke Watahiki for fruitful suggestions and comments at colloquium.

I would like to thank to Prof. Mikk Lippmaa for his kindly support, useful advices and giving me an opportunity of Hall measurements in his laboratory of the Institute for Solid State Physics (ISSP). I am also grateful to Dr. Ryota Takahashi, Dr. Tsuyoshi Ohnishi, and other members of Lippmaa laboratory for their help and helpful suggestions.

I deeply thank to Prof. Kenta Amemiya for supporting me at XMCD measurements and lots of valuable advices for my research. Without his help, I could not do XMCD experiments at BL-16A, KEK-PF.

I would like to express my sincere acknowledgement to Prof. Atsushi Fujimori. He gave me lots of enlightening advices based on his deep insight into physics. His valuable advices always encourage me.

I express my great thanks to the members of Matsumoto laboratory. I express my sincere gratitude to Prof. Yuji Matsumoto for giving me an opportunity to work in his laboratory, and enlightening comments and guidance. I also thank Prof. Masao Katayama, Dr. Akira Imai, Dr. Ryohei Tanaka, Dr. Shingo Maruyama and other members in Matsumoto

laboratory for their kind supports and encouragements.

I would like to thank the members of Hasegawa laboratory. I am deeply grateful to Prof. Tetsuya Hasegawa for allowing me to use various precious instruments. I am also grateful to Prof. Yasushi Hirose, Prof. Taro Hitosugi, Mr. Shoichiro Nakao, Dr. Takumi Ohtsuki, Dr. Kuninori Hatabayashi, Ms. Sawako Ohno, and other members of Hasegawa laboratory for their kind supports.

I would like to express my gratitude to Prof. Shin Shik for giving me an opportunity to perform IR measurements at SPring-8. I am deeply gratitude to Prof. Masaharu Matsunami for collaboration, guidance, sincere supporting and lots of discussions on optical spectroscopy.

I am grateful to the members of Koinuma laboratory. I am deeply grateful to Prof. Hideomi Koinuma for enlightening comments in the collaboration in the CREST project and always care about me. I also thank to Prof. Kenji Itaka, and Dr. Sohei Okazaki for supporting my IR measurements and scanning SQUID measurements.

The experiments at KEK-PF were supported a number of people. I would be grateful to Dr. Masato Kubota for his support of XRD measurements on LNMO films. I would like to thank to Prof. Reiji Kumai, Prof. Hironori Nakao, and Prof. Yuichi Yamasaki for their sincere supports of XRD measurements. I also thank to Prof. Kanta Ono, Dr. Nobuhito Inami, and Dr. Tetsuro Ueno, and Dr. Masako Sakamaki for their help of XMCD measurements.

I would express my acknowledgement to Dr. Hiroyuki Yamada for useful advices and his help for using XRD and MPMS in National Institute of Advanced Industrial Science and Technology (AIST).

I am thankful Dr. Takuro Nagai for STEM-EELS measurements and useful

discussions at National Institute for Material Science (NIMS).

I am sincerely grateful to Ms. Hiroko Imafuku, Ms. Kaori Mizutani, Ms. Hide Tanomuro, Ms. Kazue Suzuki, Ms. Mio Horiguchi, Ms. Arisa Oyamada, Ms. Keiko Nakamura, and Ms. Sanae Takano for supporting my research by dealing with lots of office work. I also thank them for encouraging and creating pleasant and confortable environments.

I thank to Dr. Satoshi Okamoto of Oak Ridge National Laboratory for fruitful discussions especially on theoretical models of charge spreading in transition metal oxides.

I would like to express my gratitude to Prof. Masaru Miyayama, and Prof. Hiraku Ogino for providing me helpful suggestions about this research.

I am grateful to Dr. Yuki Shiomi for lots of encouragements and useful discussions. I also thank the members of Murata Manufacturing Corporation, Mr. Hiromichi Tokuda, Mr. Yasunari Nakashima, Ms. Takako Ozawa, Ms. Minori Adachi for a lot of encouragements and moral supports. I am grateful to my special friend, Mr. Daisuke Yoshimune for his sincere supports and encouragements from my entrance of the university.

Finally I deeply thank my parents, my grandmother, and my sister for their encouragement, help, and love during my PhD and throughout my life.

Tsukuba

February, 2016

Miho KITAMURA

Appendix A

List of Publications and Presentations

Original papars

1. **M. Kitamura**, I. Ohkubo, M. Kubota, Y. Matsumoto, H. Koinuma, and M. Oshima, "Ferromagnetic properties of epitaxial La_2NiMnO_6 thin films grown by pulsed laser deposition", Appl. Phys. Lett. **94**, 132506 (2009).

2. **M. Kitamura**, I. Ohkubo, M. Matsunami, K. Horiba, H. Kumigashira, Y. Matsumoto, H. Koinuma, and M. Oshima, "Electronic structure characterization of La_2NiMnO_6 epitaxial thin films using synchrotron-radiation photoelectron spectroscopy and optical spectroscopy", Appl. Phys. Lett. **94**, 262503 (2009).

3. **M. Kitamura**, M. Kobayashi, E. Sakai, R. Takahashi, M. Lippmaa, K. Horiba, H. Fujioka, and H. Kumigashira, "Determination of band diagram for a *p-n* junction between Mott insulator $LaMnO_3$ and band insulator Nb:$SrTiO_3$", Appl. Phys. Lett. **106**, 061605 (2015).

4. R. Takahashi, I. Ohkubo, K. Yamauchi, **M. Kitamura**, Y. Sakurai, M. Oshima, T. Oguchi, Y. Cho, and M. Lippmaa, "A-site-driven ferroelectricity in strained ferromagnetic La_2NiMnO_6 thin films", Phys. Rev. B **91**, 134107 (2015).

5. M. Kobayashi, K. Yoshimatsu, E. Sakai, **M. Kitamura**, K. Horiba, A. Fujimori, and H. Kumigashira, "Origin of the Anomalous Mass Renormalization in Metallic Quantum Well States of Strongly Correlated Oxide $SrVO_3$", Phys. Rev. Lett. **115**, 076801 (2015).

6. K. Horiba, **M. Kitamura**, K. Yoshimatsu, M. Minohara, E. Sakai, M. Kobayashi, A. Fujimori, and H. Kumigashira, "Isotropic kink and quasiparticle excitations in the three-dimensional perovskite manganite $La_{0.6}Sr_{0.4}MnO_3$", Phys. Rev. Lett. **116**, 076401 (2016).

7. **M. Kitamura**, K. Horiba, M. Kobayashi, E. Sakai, M. Minohara, T. Mitsuhashi, A. Fujimori, H. Fujioka, and H. Kumigashira, "Spatial distribution of transferred charges across the heterointerface between perovskite transition metal oxides $LaNiO_3$ and $LaMnO_3$", submitted.

International conferences

1. **M. Kitamura**, I. Ohkubo, T. Ishihara, K. Horiba, H. Kumigashira, Y. Matsumoto, H. Koinuma, and M. Oshima, "Electronic state characterizations of $LaNiO_3$-$LaMnO_3$ composition spread films using synchrotron-radiation photoemission spectroscopy", MRS fall meeting, A5.9 (2007).

2. **M. Kitamura**, T. Ishihara, I. Ohkubo, M. Matsunami, K. Horiba, H. Kumigashira, Y. Matsumoto, S. Shin, H. Koinuma, and M. Oshima, "Electronic structure of ferromagnetic semiconductor $LaNi_{0.5}Mn_{0.5}O_3$ evaluated by synchrotron-radiation photoemission spectroscopy", International Symposium on Surface Science and Nanotechnology, 11a-3-7 (2008).

3. **M. Kitamura**, M. Kobayashi, E. Sakai, K. Horiba, R. Takahashi, M. Lippmaa, H. Fujioka, and H. Kumigashira, "Band diagram on *p-n* junction of Mott-insulator $LaMnO_3$ and

band-insulator Nb:$SrTiO_3$ determined by X-ray photoemission spectroscopy", 21st International Workshop on Oxide Electronics, P2-32 (2014).

4. **M. Kitamura**, K. Horiba, M. Kobayashi, E. Sakai, M. Minohara, T. Mitsuhashi, A. Fujimori, H. Fujioka, and H. Kumigashira, "Charge transfer at the heterointerface between perovskite oxides $LaNiO_3$ and $LaMnO_3$", 22nd International Workshop on Oxide Electronics, P16 (2015).

Domestic conferences

1. 北村未歩、石原敏裕、大久保勇男、組頭広志、松本祐司、鯉沼秀臣、尾嶋正治、「$LaNiO_3$-$LaMnO_3$ コンポジションスプレッド薄膜の作製と物性評価」、第 54 回応用物理学関係連合講演会、29pZA2 (2007).

2. 北村未歩、石原敏裕、大久保勇男、堀場弘司、組頭広志、松本祐司、鯉沼秀臣、尾嶋正治、「$LaNi_{1-x}Mn_xO_3$ エピタキシャル薄膜の電子状態解析」、第 68 回応用物理学会学術講演会、7pZT10 (2007).

3. 北村未歩、石原敏裕、大久保勇男、堀場弘司、組頭広志、松本祐司、鯉沼秀臣、尾嶋正治、「X 線吸収分光による $LaNiO_3$-$LaMnO_3$ コンポジションスプレッド薄膜の電子状態解析」、第 21 回日本放射光学会年会・放射光科学合同シンポジウム、13P040 (2008).

4. 北村未歩、石原敏裕、大久保勇男、松波雅治、堀場弘司、組頭広志、松本祐司、辛埴、鯉沼秀臣、尾嶋正治、「放射光光電子分光と光学測定による強磁性半導体 $LaNi_{0.5}Mn_{0.5}O_3$ エピタキシャル薄膜の電子状態解析」、第 55 回応用物理学関連連合講演会、29pL10 (2008).

5. 北村未歩、大久保勇男、松本祐司、鯉沼秀臣、尾嶋正治、「エピタキシャル La_2NiMnO_6 薄膜における磁気特性の作製条件依存」、第 56 回応用物理学関連連合講演会、31aP718

(2009).

6. 北村未歩、小林正起、坂井延寿、堀場弘司、高橋竜太、Mikk Lippmaa、藤岡洋、組頭広志、「X 線光電子分光によるモット絶縁体 $LaMnO_3$/バンド絶縁体 Nb:$SrTiO_3$ *p-n* 接合界面のバンドダイアグラム決定」、第 61 回応用物理学会春季学術講演会、18aE89 (2014).

7. 北村未歩、小林正起、坂井延寿、堀場弘司、高橋竜太、Mikk Lippmaa、藤岡洋、組頭広志、「X 線光電子分光によるモット絶縁体 $LaMnO_3$/バンド絶縁体 Nb:$SrTiO_3$ *p-n* 接合界面のバンドダイアグラム決定」、物構研サイエンスフェスタ 2014、(2014).

8. 北村未歩、小林正起、坂井延寿、堀場弘司、高橋竜太、Mikk Lippmaa、藤岡洋、組頭広志、「X 線光電子分光によるモット絶縁体 $LaMnO_3$/バンド絶縁体 Nb:$SrTiO_3$ *p-n* 接合界面のバンドダイアグラム決定」、第 28 回日本放射光学会年会・放射光科学合同シンポジウム、2C004 (2015).

9. 北村未歩、堀場弘司、小林正起、坂井延寿、簑原誠人、三橋太一、藤森淳、藤岡洋、組頭広志、「ペロブスカイト酸化物 $LaMnO_3$/$LaNiO_3$ ヘテロ界面における電荷移動」、第 62 回応用物理学会春季学術講演会、13pD104 (2015).

10. 北村未歩、堀場弘司、小林正起、坂井延寿、簑原誠人、三橋太一、藤森淳、藤岡洋、組頭広志、「ペロブスカイト酸化物 $LaMnO_3$/$LaNiO_3$ ヘテロ界面における電荷移動」、物構研サイエンスフェスタ 2015、(2015).

11. 北村未歩、堀場弘司、小林正起、坂井延寿、簑原誠人、三橋太一、藤森淳、藤岡洋、組頭広志、「ペロブスカイト酸化物 $LaNiO_3$/$LaMnO_3$ ヘテロ界面における電荷移動」、第 29 回日本放射光学会年会・放射光科学合同シンポジウム、1E002 (2016).

Publication in books

1. 大久保勇男、石原敏裕、北村未歩、尾嶋正治「機能性酸化物のコンビナトリアル薄膜の作製と電子状態解析」表面科学、vol 30、No.1、pp2-6 (2009).

Appendix B

Summary in Japanese

論文の内容の要旨

論文題目:　放射光分光による酸化物ヘテロ界面の電荷分布と
界面強磁性に関する研究
Charge distribution and ferromagnetism at oxide heterointerfaces
studied by synchrotron radiation spectroscopy

氏名　北村　未歩

本論文は、遷移金属酸化物ヘテロ界面の電荷分布と界面強磁性との相関関係について、放射光分光による電子状態、磁化状態観測の観点から述べたものである。ペロブスカイト型遷移金属酸化物からなるヘテロ接合では、その界面において特異な磁気特性が発現する。その界面磁性発現要因の１つとして界面における電荷移動が挙げられる。このような界面磁性を理解、制御するためには、価数変化とその深さ分布を決定し、その電荷移動と界面強磁性との相関関係を明らかにする必要がある。本研究では、界面電荷移動の発現の有無が予想される 2 種類の対照的な界面 ($LaNiO_3$ (LNO) /$LaMnO_3$ (LMO) ヘテロ界面、$LaMnO_3$ (LMO) /Nb:$SrTiO_3$ (STO)ヘテロ界面) を中心に据え、放射光の持つ元素選択性と界面 (表面) 敏感性を利用して、界面における電荷分布と界面磁化状態を実験的に直接決定した。

本論文は、以下の 8 章に大別して論じている。

第 1 章では、本研究の背景を述べている。遷移金属酸化物ヘテロ接合とその界面で発現する特異な磁気特性を例示し、界面強磁性の起源解明のための界面電荷移動の理解の重要性について述べている。

第 2 章では、本研究で用いた実験手法とその原理について述べている。本研究は、パルスレーザー堆積法 (PLD) による酸化物ヘテロ界面の作製と高エネルギー加速器研究機構放射光研究施設 (PF) アンジュレータービームライン BL-2C、MUSASHI (BL-2A)、及び BL-16A を用いた放射光光電子分光 (PES) 、X 線吸収分光 (XAS) 、X 線磁気円二色性 (XMCD)により行った。作製した薄膜は、反射高速電子線回折 (RHEED)、原子間力顕微鏡 (AFM)、X 線回折 (XRD)、透過型電子顕微鏡 (TEM)、透過率−反射率測定、電気抵抗測定、超伝導量子干渉計 (SQUID)を用いて評価を行った。

第 3 章では、ダブルペロブスカイト型酸化物 La_2NiMnO_6 (LNMO) の作製条件最適化について述べている。LNMO は約 280 K という室温に近い強磁性転移温度 (T_C) を有する強磁性半導体である。LNMO の強磁性の起源は Ni−O−Mn の強磁性的超交換相互作用とされている。LNMO の薄膜作製条件と、その結晶性及び強磁性特性との関係を調べることで、良好な強磁性特性を有する LNMO 薄膜の作製条件を確立した。低酸素分圧 (700 ºC, 190 mTorr) で作製した LNMO 薄膜は、酸素欠損による超交換相互作用の阻害が原因と考えられる非常に小さな磁化を示した。また、低温成長(600 ºC, 500 mTorr) では、2 種類の強磁性秩序の存在を示す 2 つの異なる T_C が観察された。これは、成長温度の不十分さに起因した局所的な Disorder が原因であると考えられる。さらに、高温・高酸素分圧成長 (700 ºC, 1100 mTorr)では、過剰酸素由来の La 欠損が原因と考えられる異相の発生が確認された。異相や酸素欠損の発生を防ぎ、Ni イオンと Mn イオンの秩序構造を促進する適切な酸素分圧、成長温度 (700 ºC, 500 mTorr) に制御することで、バルクに匹敵する強磁性特性を有する LNMO 薄膜の作製に成功した。

第 4 章では、LNMO の電子状態と磁化状態について述べている。LNMO の強磁性の起源を検証するために、Ni イオン及び Mn イオンの価数とその磁化状態について評価を行った。Ni、Mn $L_{2,3}$ XAS スペクトルにより、LNO、LMO 中では Ni イオン、Mn イオンは共に 3 価で存在するのに対し、LNMO 中では B サイトイオン間の電荷移動が ($Ni^{3+} + Mn^{3+} \rightarrow Ni^{2+} + Mn^{4+}$) が起こり、Ni イオンはほぼ 2 価、Mn イオンはほぼ 4 価に価数変化していることが明らかとなった。また、Ni、Mn $L_{2,3}$ XMCD による磁化状態の評価から、Ni^{2+} と Mn^{4+}は強磁性的に結合していることが分かった。このことから、LNMO の強磁性の起源は、Ni^{2+}−O−Mn^{4+}の強磁性的超交換相互作用であり、Ni イオンと Mn イオン間の電荷移動が強磁性発現に大きく寄与していると結論付けた。さらに、

LNMO の価電子帯、伝導帯の電子構造についても評価を行った。価電子帯光電子スペクトル、共鳴光電子スペクトル、及び O *K* XAS スペクトルから、LNMO の価電子帯上端と伝導帯下端は共に Mn 3*d* 由来の状態で構成されていることが明らかとなった。光学伝導度測定からバンドギャップは約 1.5 eV と見積もられた。価電子帯上端がフェルミ準位まで約 0.3 eV 離れていることを考慮すると、LNMO 薄膜は *p* 型半導体であると考えられ、Mn 由来のホールが多数キャリアとして伝導していることが示唆された。

第 5 章では、LNO/LMO ヘテロ構造における界面の電荷移動とその空間分布について述べている。「自然超格子」LNMO では、LNO と LMO 層が (111) 方向に 1 層ずつ交互に積層していると見なせるため、移動した電荷の空間分布を評価することができない。そこで、界面を厳密に定義した LNO/LMO ヘテロ構造での評価を行った。Ni、Mn $L_{2,3}$ XAS スペクトルにより、LNMO と同様にヘテロ界面においても Ni イオンと Mn イオンの価数がバルクの 3+からそれぞれ Ni^{2+}と Mn^{4+}に変化しており、界面を通じて Mn イオンから Ni イオンに電子が移動していることが裏付けられた。また、その膜厚依存性から、移動した電荷の空間分布について評価した。その結果、移動した電荷の空間分布は LNO 側と LMO 側で差があり、LNO では界面 1 ML に閉じ込められているのに対し、LMO では 3-4 ML の領域に広がっていることが明らかとなった。この差を記述するのに、電荷のホッピングを表すトランスファー積分とクーロン相互作用を扱った微視的なモデルが妥当であると結論付けた。

第 6 章では、XMCD による LNO/LMO ヘテロ界面における界面強磁性の観測と、界面強磁性と界面電荷移動との相関関係について述べている。Ni $L_{2,3}$ XMCD 測定では、常磁性の LNO 薄膜には XMCD 信号が観測されないのに対し、LNO/LMO サンドイッチ構造では明瞭な XMCD シグナルが観察されることから、LMO と接合することで Ni イオンに磁化が誘起されることが明らかになった。また、その LNO 膜厚の増加に伴い、XMCD 信号形状は変化せず、XMCD 信号強度、即ち Ni イオン当たりの平均磁化の大きさが減少することが分かった。このことから、Ni イオンに誘起された強磁性成分は界面の Ni^{2+}由来であると結論付けた。一方で、LMO 側では、その界面において Mn^{4+}由来の XMCD 信号が観測された。これらの XMCD 信号の方向を比較することで、界面において Ni^{2+}と Mn^{4+}が強磁性的に結合していることが明らかとなった。第 5 章の結果から、電荷移動により界面の Ni イオンと Mn イオンの価数が変化していると考えられ、この価数変化したイオン同士が強磁性的に結合していることから、LNO/LMO ヘテロ構造においては、界面電荷移動が界面強磁性を誘起する鍵であると結論付けた。

第 7 章では、モット絶縁体 LMO/バンド絶縁体 Nb:STO *p-n* 接合界面のバンドダイアグラム決定について述べている。LMO-STO 超格子で報告されている特異な強磁性と界

面電荷移動との関係を明らかにするため、まず、XAS により電荷移動の有無について評価を行った。Ti $L_{2,3}$ XAS スペクトルから、接合前後で Ti の価数は共に 4 価であり、Mn イオンと Ti イオンの間で電荷移動が生じていないことが明らかとなった。そこで、特異な強磁性の知見を得るため、界面の電子状態を解明することを目的として PES を用いてバンドダイアグラムの決定を行った。Nb:STO 基板に LMO 薄膜を堆積して接合を形成すると、Ti 2*p* 内殻光電子スペクトルは低結合エネルギー側にシフトした。このシフト量は Nb:STO 側に形成されるビルトインポテンシャルに対応していると考えられ、Nb:STO 基板の 0.1 at. %から 1.0 at. %への Nb ドープ量増加に伴うキャリア量の増加に応じて、0.55±0.05 eV から 0.25±0.05 eV へと減少した。このシフト量から半導体の *p-n* 接合理論を用いて界面に生じるビルトインポテンシャル (V_b) は 0.66±0.12 eV と算出され、LMO/Nb:STO 接合のバンドダイアグラムを描くことに成功した。これらの結果から、LMO/Nb:STO の接合は、V_b を B サイトイオン間の電荷移動によって遮蔽するのではなく伝導キャリアの空乏化によって遮蔽する、通常の半導体における *p-n* 接合理論の枠内で記述できると結論付けた。このことから、LMO-STO 超格子における特異な強磁性は、電荷移動以外の要因で発現していることが示唆された。

第 8 章では、本論文のまとめ及び今後の展開を述べている。

以上のように本論文は、2 種類の異なるヘテロ界面に対して、界面における電荷分布と界面磁化状態の相関関係を放射光の元素選択性を用いて明らかにしたものである。本研究で得られた知見に基づき適切な界面を作製して界面電荷分布を制御することで、界面強磁性の設計・制御につながると考えられる。